NTNU – Trondheim
Norwegian University of
Science and Technology

Slag Refining of Iron with Respect to Phosphorus

Raghed Saadieh

Silicon and Ferroalloy Production
Submission date: June 2014
Supervisor: Leiv Kolbeinsen, IMTE
Co-supervisor: Stian Seim, TTI Norway

Norwegian University of Science and Technology
Department of Materials Science and Engineering

Preface

This project was carried out at the Department of Material Science and Engineering, at the Norwegian University of Science and Technology (NTNU) during the spring of 2014.

First, I would like to thank my supervisor Professor Leiv Kolbeinsen for his support and guidance through the entire life of this project. I highly appreciate your enthusiasm for teaching and making me a better engineer, and gaining a wider perspective on a multitude of topics through our weekly discussions. I will always remember your saying: "There is no stupid questions, only stupid answers".

Secondly, I would like to thank my co-supervisors Stian Seim and Stephen Lobo. They made my journey easier and where always ready to help and to offer advice whenever they can. Moreover, I would like to thank TiZir Titanium & Iron in Tyssedal, Norway for their collaboration on this project, and for the valuable and constructive discussions, I had with the different employees at Tyssedal when I presented my work.

In addition, I would like to point out that I could not go through the practical lab experiments without the help of Delphine Leroy, Harald Holm and Trygve Schanche, who taught me how to use a multitude of equipment and furnaces. Furthermore, I would like to thank Julian Tolchard for his help with the XRD analysis and Morten Raanes for his help with the EPMA analysis.

Finally yet importantly, I would like to thank all the members of the SiManTi research group for their discussions, feedback and different social activities we had. Lastly, I am grateful to my family in Lebanon for their continuous support during my two years master study in Norway.

Abstract

TiZir Titanium and Iron produces high purity pig iron and titania slag from ilmenite. However, new ilmenite ores from "Grande Côte Mineral Sands Project" mine contain high level of phosphorus, which will contaminate the final iron product produced at the smelter in the future. As a result, a solution to remove the phosphorus from iron was needed. This work focused on studying the dephosphorization process using slags by compiling the existing information available in the literature and finding the best system for the Tyssedal process.

For this purpose, an experimental protocol was developed which consisted of smelting pure iron-phosphorus alloy and carrying out refining experiments on it using binary Fe_2O_3-CaO and ternary slags Fe_2O_3-CaO-SiO_2 slags. The best performing slag was chosen and another set of experiments was carried out on iron smelted at TiZir, Tyssedal. In these experiments, the effects of refining temperature and time were also investigated. However, when the same slag was tested on the iron from TiZir, results were very different since the metal and slag were strongly mixed. Analysis on the iron, as well as XRD and EPMA on the slag were carried.

Dephosphorization was successful on the pure Fe-P alloy and up to 99% of the phosphorus was removed using a (50wt% FeO, 45wt% CaO, 5wt% SiO_2) slag. On the other hand, accurate conclusions concerning dephosphorization on the iron from TiZir were not made due to the strong mixing between the slag and metal, which lead to limitations in the analysis. The main explanation behind this observation is the different amount of impurities in the two types of iron, especially carbon and silicon. Hence, more work is need to study the effect of these impurities on the dephosphorization process as well as refining temperature and time.

Contents

LIST OF FIGURES ..... **VII**

LIST OF TABLES ..... **XI**

LIST OF SYMBOLS **1**

1 INTRODUCTION **2**

2 BACKGROUND **4**

2.1 THE TYSSEDAL PROCESS 4

2.2 THE GRAND CÔTE MINERAL SANDS PROJECT 7

2.3 THE BLAST FURNACE 8

2.4 OVERVIEW OF THE DIFFERENT TYPES OF REACTIONS OCCURRING IN STEELMAKING 12

3 THEORY **13**

3.1 ACTIVITY DISCUSSION 13

3.2 STRUCTURE OF SLAGS 15

3.3 PHOSPHORUS OXIDATION 19

3.4 SLAGS FOR OXIDATION REACTIONS 26

3.5 THE TOTAL MASS TRANSFER COEFFICIENT 47

4 EXPERIMENTAL **57**

4.1 MATERIALS 57

4.2 EXPERIMENTS 59

4.3 ANALYSIS TESTS 62

5 RESULTS **64**

5.1 IRON ALLOYS 64

5.2 REFINING EXPERIMENTS 66

6 DISCUSSION **86**

6.1 IRON ALLOYS 86

6.2 REFINING EXPERIMENTS 86

7 CONCLUSION **93**

8 FUTURE WORK **95**

BIBLIOGRAPHY **96**

A. TEMPERATURE CURVE **99**

B. IRON ANALYSIS **100**

C. PHYSICAL APPEARANCE **104**

D. XRD **106**

E. EPMA **119**

List of figures

Figure 2.1: Flowchart of Tyssedal process (adapted from [10]) 6

Figure 2.2: Graphical representation of dredging operation (courtesy Tizir, Norway) 7

Figure 2.3: Grand Côte mine location (courtesy Tizir, Norway) 8

Figure 2.4: Iron blast furnace (courtesy SSAB, Sweden) 11

Figure 3.1: Activity as function of mole fraction (schematic)[13] 14

Figure 3.2: Calculated ion distribution for CaO-SiO2 (a), MnO-SiO2 (b), and FeO-SiO2 (c) at 1600^0C.(17) 19

Figure 3.3: Nomogram correlating $\%Fe_{total}$ in slag (containing dicalcium silicate), %Si in hot metal, %P is steel and specific lime consumption[20] 21

Figure 3.4: Phosphorus distribution between liquid iron and steelmaking slag saturated with CaO or Ca-phosphate[21] 22

Figure 3.5: Influence of FeO concentration in slag on activity coefficient of P_2O_5 [22] 22

Figure 3.6: Equilibrium partitioning of Phosphorous between slag and metal[22] 23

Figure 3.7: Relationship of Fe content in pig iron, iron recovery rate (a), P content in pig iron and dephosphorization rate (b) to reduction temperature [3] 24

Figure 3.8: Relationship of Fe content in pig iron, iron recovery rate (a), P content in pig iron and dephosphorization rate (b) to basicity [3] 25

Figure 3.9: Relationship of Fe content in pig iron, iron recovery rate (a), P content in pig iron and dephosphorization rate (b) to blowing- oxygen time [3] 25

Figure 3.10: Iron-oxygen phase diagram (adapted from [23]) 28

Figure 3.11: FeO_n-CaO phase diagram [26] 30

Figure 3.12: CaO-Fe2O3 phase diagram [26] 32

Figure 3.13: Schematic representation of the Fe-O-CaO system [28] 33

Figure 3.14: FeO-Fe_2O_3-CaO phase diagram [29] 33

Figure 3.15: Phase diagrams of magnesium oxide–iron oxide system in equilibrium with metallic iron (a) and in equilibrium with air (b).[26] 34

Figure 3.16: CaO-SiO_2 phase diagram. [26] 36

Figure 3.17: CaO-P_2O_5 phase diagram. [26] 37

Figure 3.18: CaO-FeOn-SiO2 phase diagram. [26] 38

Figure 3.19: CaO-FeO_n-SiO_2 phase diagram with isoactivity lines for iron (II) oxide at 1600^0C. [32] 39

Figure 3.20: MgO and MnO influence on the slag equilibria in the Fe- FeO_n-CaO- SiO_2 system at 1600^0C. [33] 40

Figure 3.21: Line of equal phosphorus distribution in the system CaO-(SiO_2+P_2O_5)-(FeO_n+MnO). (adapted from [34, 35]) 43

Figure 3.22: A section of the CaO- P_2O_5 -FeO_n constitutional phase diagram, saturated in iron. [37] 44

Figure 3.23: Isothermal section of the CaO- P_2O_5 -FeO_n constitutional phase diagram, in equilibrium with iron at 1600^0C. [38] 45

Figure 3.24: Oxygen and phosphorus contents in iron melts saturated with tetracalcium phosphates and lime slags of the CaO- P_2O_5 -FeO_n system at 1600^0C. (adapted from [40-44]) 46

Figure 3.25: Equilibrium ratio as a function of the iron oxide content in different types of slags. [36] 47

Figure 3.26: Concentration profiles in the melt and the slag[46] 49

Figure 3.27: Mixing reactor [46] 50

Figure 3.28: [%x]/$[\%x]_{in}$ ratio versus X [46] 52

Figure 3.29: Exponantial drop of the concetration in the melt %x versus time [46] 56

Figure 4.1: The Resina furnace 60

Figure 4.2: Experimental setup used in Set A and B of experiments 60

Figure 5.1: Temperature curves for all the refining experiments 66

Figure 5.2: Pictures showing the slag and metal surfaces in Experiment 8 67

Figure 5.3: Pictures showing the physical appearance of the samples in Set A 68

Figure 5.4: The appearance of the different samples right after the completion of the experiments 10-11-12 (from left to right) 69

Figure 5.5: The appearance of the different samples after being left couple of days in the air 70

Figure 5.6: XRD pattern of the slag powder in experiment 1 75

Figure 5.7: XRD pattern of the slag powder in experiment 2 and 5 75

Figure 5.8: XRD pattern of the slag powder in experiment 6 and 7 76

Figure 5.9: XRD pattern of the slag powder in experiment 8 76

Figure 5.10: XRD pattern of the slag powder in experiment 9 77

Figure 5.11: XRD pattern of the slag powder in experiments 10a, 10b and 12b 78

Figure 5.12: Different samples used for EPMA (from left to right: experiment 10.1, 10.2, 11, 12) 79

Figure 5.13: Surface image and point analysis of experiment 10.1 81

Figure 5.14: Surface image and point analysis of experiment 10.2 82

Figure 5.15: Surface image and point analysis of experiment 11 83

Figure 5.16: Surface image and point analysis of experiment 12 84

Figure 5.17: Quantitative mapping of the sample in experiment 10.1 85

Figure A.1: Temperature curve for the smelting of alloy B 99

Figure C.1: Physical appearance of the sample from experiment 10 104

Figure C.2: Physical appearance of the sample from experiment 11 105

Figure C.3: Physical appearance of the sample from experiment 12 105

Figure D.1: XRD pattern for experiment 1.....107

Figure D.2: XRD pattern for experiment 2.....108

Figure D.3: XRD pattern for experiment 3.....109

Figure D.4: XRD pattern for experiment 4.....110

Figure D.5: XRD pattern for experiment 5.....111

Figure D.6: XRD pattern for experiment 6.....112

Figure D.7: XRD pattern for experiment 7.....113

Figure D.8: XRD pattern for experiment 8.....114

Figure D.9: XRD pattern for experiment 9.....115

Figure D.10: XRD pattern for experiment 10a 116

Figure D.11: XRD pattern for experiment 10b 117

Figure D.12: XRD pattern for experiment 12b 118

Figure E.1: First EPMA image of experiment 10.1.....119

Figure E.2: Second EPMA image of experiment 10.1.....120

Figure E.3: Third EPMA image of experiment 10.1 121

Figure E.4: First EPMA image of experiment 10.2.....122

Figure E.5: Second EPMA image of experiment 10.2.....123

Figure E.6: First EPMA image of experiment 11.....124

Figure E.7: Second EPMA image of experiment 11.....125

Figure E.8: Third EPMA image of experiment 11 126

Figure E.9: Fourth EPMA image of experiment 11 127

Figure E.10: First EPMA image of experiment 12.....128

Figure E.11: Second EPMA image of experiment 12.....129

Figure E.12: Third EPMA image of experiment 12 130

Figure E.13: Mapping of an area from experiment 12.....131

Figure E.14: Mapping of a second area from experiment 12 132

List of tables

Table 4.1: Chemical composition of Tizir iron, 800 quality 58

Table 4.2: Industrial iron-phosphide chemical composition 58

Table 4.3: Slag composition in first set of experiments (Set A) 61

Table 4.4: Experimental conditions in second set of experiments (Set B) 62

Table 4.5: Analysis tests performed on the different samples (+=done, /= not done) 63

Table 5.1: Initial Chemical composition of Alloy A 64

Table 5.2:Final Chemical composition of Alloy A (After the re-melting) 64

Table 5.3: Chemical composition of Alloy B 65

Table 5.4: Chemical composition of the samples from set A of experiments after refining ... 71

Table 5.5: Iron loss as well as phosphorus and carbon removal in Set A of experiments 72

Table 5.6: Chemical composition of the iron in experiment 11 after refining compared to that of Alloy B 73

Table 5.7 : Species present in the slag from the different experiments accorindg to XRD analysis 74

Table B.1: Detailed chemical composition of the different points in Alloy A 100

Table B.2: Detailed chemical composition of the different points in Alloy B 101

Table B.3: Detailed chemical composition of the iron in experiments 1-7 102

Table B.4: Detailed chemical composition of the iron in experiments 8-9 103

Table B.5: Detailed chemical composition of the iron in experiment 11 103

List of symbols

Symbol	Description
A_s	Melt top surface area (m^2)
a_v	Slag-metal area (m^2)
a_x	Activity of species x
$C_{(PO_4^{3-})}$	Phosphate capacity
f_P	Henrian activity coefficient
ΔG^0	Standard Gibbs free energy (J/mol)
$\dot{G}_x$	Removal rate of impurity x (kmol/s)
K	Equilibrium constant
k	Mass transfer coefficient (m/s)
$\dot{M}$	Flow of the metal into the reactor (kg/s)
M_x	Molar weight of species x (kg/mol)
N	Number of reactors
$\dot{n}$	Molar flux ($kmol/m^2s$)
p	Pressure, partial pressure (atm)
R	Gas constant
T	Temperature
t	time
X	Ion fraction, mole fraction
Z	Efficiency of removal technique
γ_x	Activity coefficient of x
$\gamma_x^{(y)}$	Interaction coefficient
ρ	Density (kg/m^3)
τ	Dimensionless time, residence time

1 Introduction

Iron is one of the most important elements in the history of human development. The discovery of iron in the period we know as "The Iron Age" helped early humans to overcome many challenges, which accompanied the use of bronze (copper alloy) in earlier stages. In modern days, iron is employed in almost every application that impacts our life. It is even the most important constituent of hemoglobin, a protein complex, which allows red blood cells to transport oxygen in the body. The extensive use of iron was accompanied by a development in the metallurgical and mining industry. As a result old iron deposits, which contained the best ore grades, are being depleted and newer deposits are being investigated. The problem that is arising is related to the impurities in the recently discovered or excavated ores. The main concern in this study revolves around ilmenite ores from "Grande Côte Mineral Sands Project". These ores contain high level of phosphorus, which will contaminate the final iron product produced at the Tyssedal smelter. Phosphorus is one of the most important elements that can improve the strength of steels [1]; however, its presence in large amounts (limit is 0.15wt% and only found in special HSLA steels) can aggravate embrittlement [2].

The most widely employed industrial technique to remove phosphorus from iron and steel is slag refining [3, 4]. In addition, acid leaching is discussed in the literature [5, 6] and a reference to the concept of leaching using biological organisms like bacteria was also found [7]. On the other hand, references to vacuum refining of P in steels/iron are scarce. However vacuum degassing is widely used in the steel industry to remove volatile species (C, N, H)[8] and vacuum refining is also employed when ultra-high purity metal is produced [9] and the advantages of this technique is opening the way to new development and research in this field.

The slag refining process, although very successful, remains challenging. This is due to the impurities that can be found in the iron and that might alter the slag composition. Two such impurities are carbon and silicon, which can be simultaneously oxidized with phosphorus, hence competing with the dephosphorization. In addition, silicon will enter the slag as SiO_2 decreasing its basicity and consequently its phosphate capacity. Moreover, refining temperature and time can vary from a system to another. The general guidelines for successful dephosphorization are given in this thesis; however, each system should be studied thoroughly to extract the best conditions.

The aim of this study was to investigate removal of phosphorus from the industrial iron smelted at Tyssedal by Tizir Titanium and Iron AS, using slag refining. The effect of slag composition, effect of impurities, refining time and temperature were all studied. This study will serve as a guideline to compare the results obtained from the lab experiments to the industrial trials carried out at Tyssedal. In addition, the study aimed to develop a systematic experimental protocol, which can be used at later stages to further investigate the process. Kinetics were not investigated due to limitation in the equipment and the complexity of the experimental setup

needed and should be the focus of a separate study. The remainder of this study is divided according to the following:

- Background: a description of the Tyssedal process as well as the "Grande Côte Mineral Sands Project" and the blast furnace is given. In addition, an overview of the different reactions taking place during steelmaking is presented.
- Theory: discussion about activities, structure of slags and the thermodynamics of dephosphorization is given. In addition, different slag systems are presented and a short kinetic discussion focusing mass transfer is provided in this section.
- Experimental: the details for the different experiments and how they were carried out is given here. In addition, the different analysis techniques are also mentioned.
- Results: the results from the different experiments are presented.
- Discussion: the results are discussed here, based on the concepts described in the theory section.
- Conclusion: a summary of the results obtained.
- Future work: suggestions are given to further investigate the process.

This study will also contain an appendix containing different tables and figures.

2 Background

2.1 The Tyssedal process

This section is based on the work of J. Solheim in "The Tyssedal Ilmenite Smelting Process" [10]. The Tyssedal smelting process is used by TiZir Titanium and Iron AS to upgrade the ilmenite ores and produce metallic iron and titania slag. It consists of two main steps. First, the ilmenite concentrate is ball-milled under wet conditions to pelletizing size. The pulp then flow to a slurry tank before reaching the filter station. The milled ilmenite is then dewatered to about 9% moisture and mixed with 0.8% bentonite (binder material) in a separate mixing machine. This mixture is consequently transported to a pelletizing drum, which will produce raw pellets ranging in size from 9-16mm. The pellets are then distributed over a roller type feeder screen to help in the removal of residual fines and seeds, which are recycled to the classifier. The feeder screen is located at the end of the grate kiln unit.

The length of the travelling grate is 21m and has a width of 2.8m, and the pellets are usually retained for 20minutes. During this time, the pellets are subjected to gradual drying, preheating, and hardening and oxidizing to about 750^0C max, using the kiln gas.

Afterwards, the pellets are charged from the grate into the kiln with coal and recycled char additions. The coal serves two main purposes: to provide enough heat for both the kiln and grate, and to form a reducing atmosphere which will reduce the pellets to 70-75% metallization. This degree of metallization grants more adjustments flexibility in the final reduction step in the electric smelting furnace.

The kiln is 72m in length and 5.8m in diameter and it is equipped with a startup oil burner and a coal slinger at the outlet end. The coal is also charged from there. The kiln is loaded with pellets and coal to about 25%, and rotates at 0.5rpm with a retention time of approximately 9hours. Air is injected into the kiln to ensure combustion of the reduction products and to help maintain the temperature at 1150^0C.

The gases from the kiln are then fed to an afterburner and part of this gas is also utilized in the grate. All the process gases are washed and cleaned before discharged into the atmosphere. The reduced products (including coal and ashes) are then fed into a rotary steel drum cooler, 60m in length and 4.7m in diameter, to cool down the material to about 60^0C. The cooling process revolves around spraying the outer shell of the drum with cold water.

The cooled pellets are than discharged into a pan conveyer, which will in turn transport them to screening and magnetic separation stations. At this stage, the coke and non-magnetic coal ashes are separated. Pellets with oversize of +25mm will go into the smelting furnace. The next screening stage accepts pellets ranging from 3-25mm, and these pellets are fed later into the furnace via buffer silos.

The smaller pellets are stored into separate silos and can be fed into the furnace. Nonmagnetic products are charged into the kiln again.

The furnace itself is a conventional three-phase iron-smelting furnace having three self-baking Søderberg electrodes. The load is 33MW, which is supplied by three one-phase transformers of 17MVA capacity each. In the furnace, the pellets are melted into two phases. An iron layer at the bottom of the furnace and a floating TiO_2 slag on the top. These two phases are taped through separate tap holes.

The slag is tapped into railway wagons where is its water-cooled until it is solidified, and it is then lifted and dumped into intermediate concrete bins. The slag is stored for 6 days in those bins for oxidation. It is then crushed and grinded to -12mm TiO_2 slag in a separate plant. Finally, the finished product is transported to four storage silos (6500t capacity each).

The iron follows a separate route; it is tapped into preheated ladles (60t capacity) which are carried out by a crane into a wagon. This wagon is equipped with inductive stirring coils, to help in the skimming process. After skimming, cover fluxes are added and then it is transported to another furnace (13MVA) to increase the temperature to 1575^0C. The iron is treated via injection and additions of petrol coke, calcium carbide and ferrosilicon to give the right quality. The resulting slag is then skimmed and the iron is cast into ingots, a water-cooled casting machine, equipped with two belts with 340 molds each are used for this step. The ingots weigh 6-8kgs.

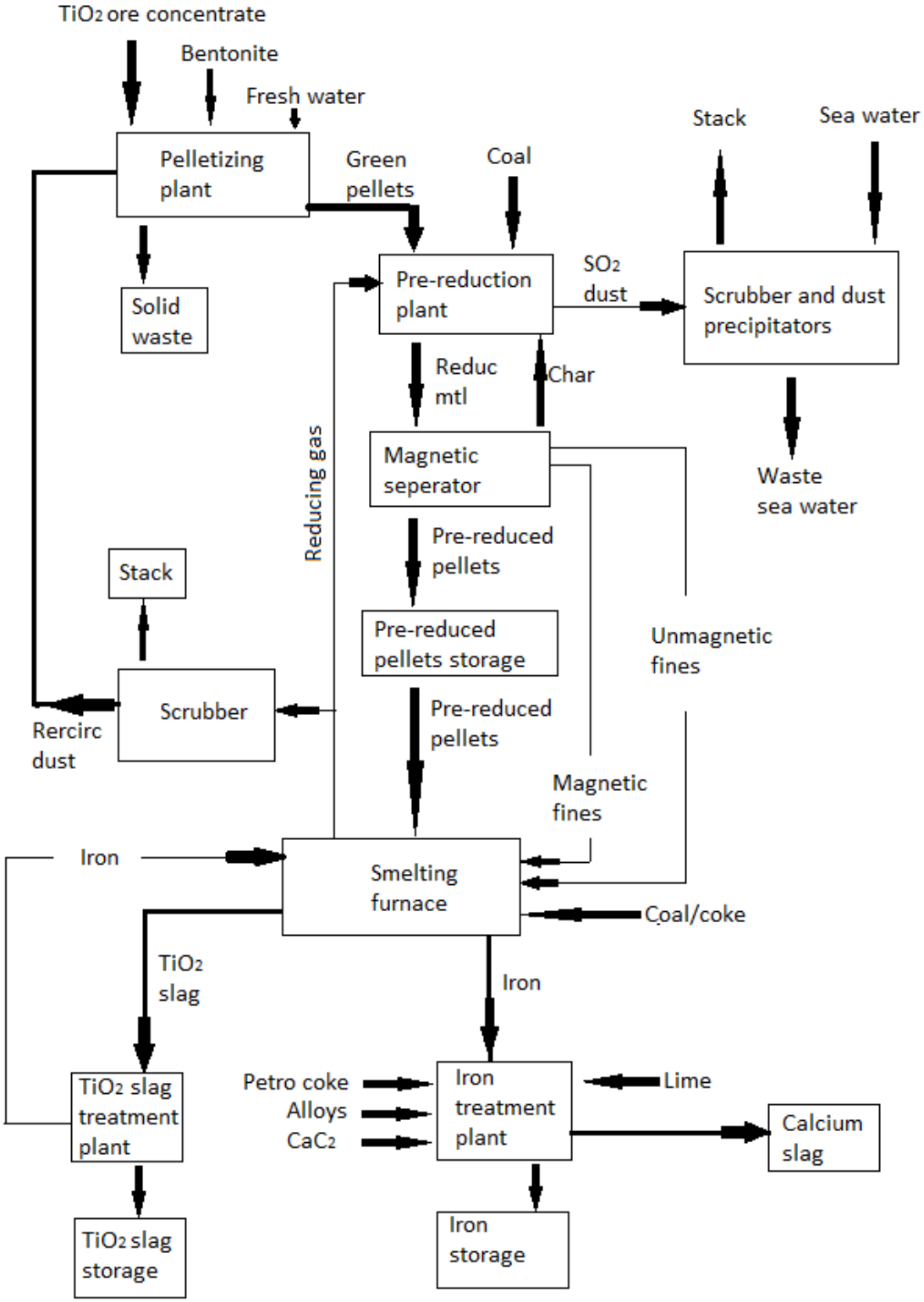

Figure 2.1: Flowchart of Tyssedal process (adapted from [10])

2.2 The Grand Côte mineral sands project

The following section is based on the information provided on the official site of TiZir limited [11]. The Grand Côte mineral sands project is located in Senegal, West Africa and is operated by TiZir. The project lies of a coastal, mobile dune system approximately about 50km north of Dakar. It is 100km in length and 4km in width covering a massive 400Km^2 area. The mine is expected to run for at least 20 years and the production is estimated around 575ktpa of ilmenite and 85ktpa of zircon when it reaches its full working capacity. The probable and proved ore reserve is estimated around 751million tons of 1.8% heavy mineral. The mine is planned to start production in 2014.

Since the ore consists of sand dunes containing minor vegetation and no overburden, the extraction process will be simple and will consist of dredging and processing.

Figure 2.2: Graphical representation of dredging operation (courtesy Tizir, Norway)

Utilizing the shallow water table in the area, the dredge will easily travel through the dunes. Sand will be mined from the front of the dredge and a slurry will be than pumped to a floating concentrator. The sand will pass through spirals, where it will be washed and the heavy minerals will be separated from the lighter quartz sand. The sand is then dumped again into the pond and hence the landscape will be restored. At this stage, the heavy minerals are moved to the separation plant. Separation techniques consist of electrostatic, magnetic and gravity process which will help concentrating the minerals into four classes: zircon, ilmenite, leucoxene and rutile. The separation process is environmentally friendly since no chemicals are used.

After processing, zircon will be shipped and sold to customers in Europe and North America, whereas the ilmenite will be shipped to Norway where it will be processed at the TiZir Tyssedal

titanium smelter, which will produce titania slag and iron and then shipped to customers in Europe and China. The ilmenite ore contains high level of phosphorus, which will end up contaminating the produced iron.

Figure 2.3: Grand Côte mine location (courtesy Tizir, Norway)

2.3 The blast furnace

The following section is based on the work of T. Rosenqvist in Principles of Extractive Metallurgy [12].The current blast furnace technology is the result of many centuries of development. In the Iron Age, iron was smelted in primitive holes in the ground, and primitive blast furnaces were used the first time during the late medieval period. Further development led to the use of coke and hot blast in the 18th century. The biggest development occurred in the 20th century, where optimal practices were employed: higher blast temperatures, better burden preparations and increased furnace pressure. Moreover, the capacity of these furnaces was increased and coke consumption has been decreased from 1000kg to below 500kg per ton of iron smelted. The main driving force behind these developments was a better understanding of the reactions taking place in the furnace and their impact on the coke consumption and smelting capacity.

The furnace is mainly a steel shaft of 20 to 30m high lined with refractory bricks. The charge material is iron ore, coke and fluxes. Fluxes (lime, limestone and sometimes dolomite) are added to obtain a slag of suitable composition. Hot air is introduced at the bottom of the furnace through tuyeres. As a result, furnace gases are collected at the top of the shaft whereas the molten metal, known as pig iron, and the slag are tapped out from the hearth located at the bottom of the furnace. The part connecting the hearth and the stack is an inverted cone called the bosh.

Many reactions take place in the different parts of the furnace. At the tuyeres level, coke reacts with air according to the following reaction:

Reaction 2.1

$$2C + O_2 = 2CO$$

This reaction supplies the furnace with the necessary heat and reducing gas. In the upper part of the stack, reduction of the ore takes place through a series of reactions:

Reaction 2.2

$$3Fe_2O_3 + CO = 2Fe_3O_4 + CO_2$$

Reaction 2.3

$$Fe_3O_4 + CO = 3FeO + CO_2$$

Reaction 2.4

$$FeO + CO = Fe + CO_2$$

These reactions start when the temperature is around few hundred degrees Celsius. In modern practices, Fe_2O_3 and Fe_3O_4 are reduced to FeO before the start of the metallic iron reduction. The main reason behind this practice is to obtain the most efficient use of the reducing gas (CO) and it is ensured by the use of very reactive ores having small lump size (pellets). If the ores are less reactive and coarser, than the above-mentioned reactions can overlap.

Then reduction of wustite to iron will occur when the ore has reached the stacks' lower parts with temperature above 1000^0C. At this stage, the reaction taking place on coke surface is very rapid, and as a result Boudouard reaction and wustite reduction will take place simultaneously. Thus, the overall reaction can be written as:

Reaction 2.5

$$FeO + C = Fe + CO$$

Although this reaction occurs through the gas phase, it is sometimes referred to as "direct reduction" [12]. In addition, the reaction between CO and the iron ore in the stacks' upper part is referred to as "indirect reduction" [12], since the temperature is not enough for coke reaction.

In the lowest part of the furnace, molten products are present. As a result, the following reactions take place to some extent:

Reaction 2.6

$$MnO + C = \underline{Mn} + CO$$

Reaction 2.7

$$SiO_2 + 2C = \underline{Si} + 2CO$$

In this case, silicon and manganese will enter the iron melt and should be removed during the refining step of steelmaking to obtain the desired steel grades.

It is important to note the effect of the CO_2/CO ratio, which is determined by the equilibrium between FeO-Fe. A higher ratio is the result of the ore being more reactive than the coke and reduction takes place around 900^0C. However if the ore is less reactive, higher temperature is needed and this gives a lower CO_2/CO ratio. So the highest efficiency is obtained with unreactive coke. Moreover, the coke should have good mechanical properties in order to be able to carry the weight of the burden.

One last reaction that can take place around 500-600^0C is soot precipitation. This reaction has little effect on the overall stoichiometry of the blast furnace and on coke consumption due to the closed-circuit circulation. However, it can damage the refractory bricks and is regarded as harmful.

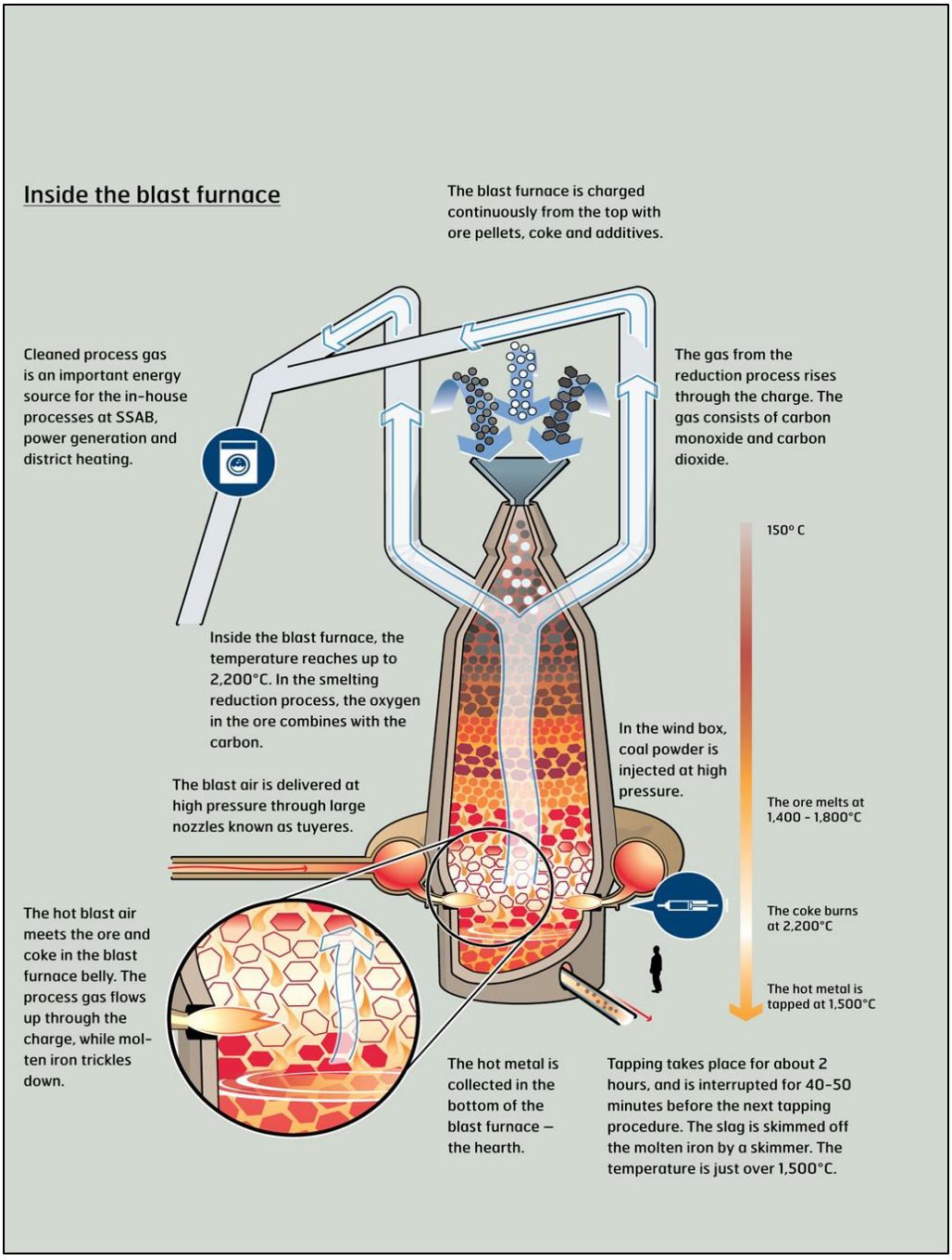

Figure 2.4: Iron blast furnace (courtesy SSAB, Sweden)

2.4 Overview of the different types of reactions occurring in steelmaking

This section is based on the work of F. Oeters in Metallurgy of Steelmaking [13]. The iron produced from the blast furnace, usually referred to as pig iron, contain high level of carbon and other impurities. In order to obtain steel, the pig iron must be refined and the total amount of impurities should be less than 1% by weight. Steels frequently contain <0.1%C, <0.04%P, <0.03%S and <0.005%N. Moreover, the level of Si and Mn are adjusted in the metal according to the different steel grades required. Carbon and phosphorus are usually removed by oxidizing the hot metal. The oxidation of carbon and its subsequent removal is known as decarburization. Simultaneous oxidization of Si and Mn, as well as some of the iron, usually accompany the oxidation of the aforementioned impurities. The oxides formed upon refining produce a separate phase (except for CO, which leaves the melt as a gas), known as slag. Refining processes of reducing nature remove the rest of the impurities.

All the oxidizing refining processes will produce a steel melt with high oxygen content covered with a layer of slag. The equilibrium between those two phases, metal and slag, will determine the degree of refining of the impurities. The oxidation reaction is given by:

Reaction 2.8

$$x[Me] + y[O] = (Me_xO_y)$$

Hence, the equilibrium between the metal-slag phases is given by:

Equation 2.1

$$K_{Me_xO_y} = \frac{(a_{Me_xO_y})}{[a_{Me}]^x [a_O]^y}$$

In Reaction 2.8, the brackets indicate that the elements are present in the iron phase whereas the parentheses denote the oxides in the slag. After the oxidation processes, the hot metal contain a high content of free oxygen, which will end up precipitating in the melt as oxides, which have an adverse effect on the quality of the steel. As a result, oxidation of the metal is usually followed by a deoxidation process to remove the oxygen from the metal, which is usually carried in ladles and the process is known as ladle metallurgy.

Nitrogen is usually removed simultaneously in the decarburization process, where the carbon monoxide bubbles flush it out. Sulfur and hydrogen are removed during ladle treatment, where the first is removed by converting it into sulfides (S^{2-}) and the second by degassing treatment either by vacuum or by argon purging.

Reaction 2.9

$$[S] + 2e^- = S^{2-}$$

Reaction 2.10

$$[H]_{dissolved} = {}^1/_2\, H_{2,gas}$$

As a result, the refining processes can be divided into four categories:

1. Oxidizing reactions
2. Reducing reactions, especially desulphurization
3. Deoxidation reactions
4. Degassing reactions

Of particular interest for this thesis are oxidizing reactions, which will be discussed thoroughly in the upcoming sections.

3 Theory

3.1 Activity discussion

This section is based on the work of F. Oeters in Metallurgy of Steelmaking [13]. In iron melts, different impurities interact within themselves and with iron. These interactions are thermodynamically expressed as activities. Consequently, a relationship exists between the activity a of species x and its dissolved concentration c. In (Figure 3.1), the ideal behavior follows Raoult's law and is presented as a straight line. However, real behavior deviates from the ideal one either positively or negatively. Moreover, the tangents to the ideal curves at $c = 0$ are referred to as Henrian lines, since they follow Henry's law, which apply at infinite dilution. The relation between the activity and the concentration is given by:

Equation 3.1

$$a_x = \gamma_x [x]$$

At very low concentrations, this relationship follows Henrian line, and consequently one can note that the activity coefficient is constant. By substituting for the expression of activity in Equation 2.1, we obtain:

Equation 3.2

$$K_{Me_xO_y} = \frac{(Me_xO_y)}{[Me]^x[O]^y}\frac{\gamma(Me_xO_y)}{\gamma^x_{[Me]}\gamma^y_{[O]}}$$

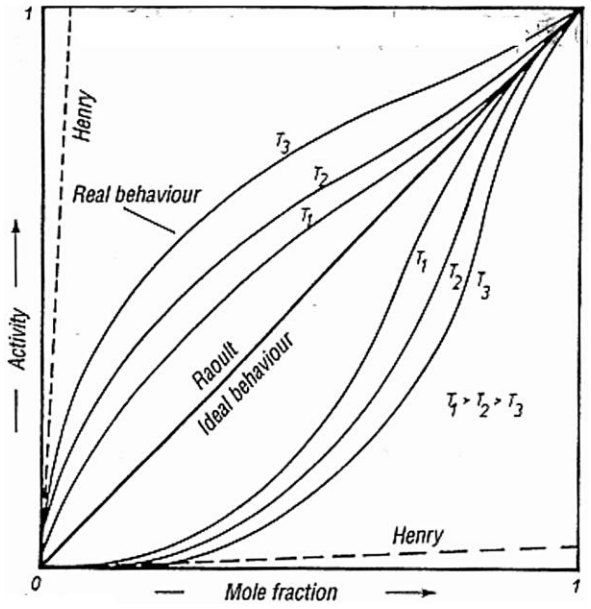

Figure 3.1: Activity as function of mole fraction (schematic)[13]

As it was already mentioned, at low concentrations, the activity coefficient is constant and hence the product of the different activity coefficients can be incorporated in the equilibrium constant and it will be possible to carry out numerical calculations directly by using the concentrations. Measurements on the activities of various different elements in iron and steel agree with the theoretical approach, since most of these elements occur in very low concentrations. However, one exception is carbon, which shows deviation from Henry's law due to its presence in higher quantities.

Moreover, all the different elements exert a mutual influence on each other. This is taken into account by incorporating the different interactions into the activity coefficient given by:

Equation 3.3

$$\gamma_x = \gamma_x^{(x)} \gamma_x^{(y)} \gamma_x^{(z)}$$

Where $\gamma_x^{(x)}$ refers to the activity coefficient in the binary Fe-X system and $\gamma_x^{(y)}$ is the interaction coefficient which indicates the effect of x on y etc. These interactions can be either significant or negligible depending on the quantity and the nature of each element.

3.2 Structure of slags

As mentioned before, when different elements are present in a metallic melt, they are bound to interact with each other. The same applies for different species in slags. However, these interactions exhibit wide variations compared to metallic melts and can differ from their respective concentrations by several order of magnitudes, and depend largely on slag composition.

The main theory describing the behavior of slags is based on the assumption that they form an ionic solution upon melting [14, 15, 16]. This assumption has been proven by different experimental measurements especially by measuring the electrical conductivity and the ion transport numbers when molten slags are subjected to electrical currents. In modern literature, strong basic oxides are assumed to fully dissociate into ions (e.g. Na_2O, CaO). Whereas less basic oxides dissociates partially. Those include, but not limited to MnO, FeO, MgO and NiO. These will occur as cations accompanied by anionic species especially O^{2-}. On the other hand, acidic oxides form anionic species (e.g. SiO_4^-, PO_4^{3-}, AlO_3^{3-}).

As a result, one can define the molar concentrations of the specific ions by using the concept of ionic fraction, which is calculated for cations and anions separately.

Equation 3.4

$$X_{i,cation} = \frac{n_{i,cation}}{\sum_i n_{i,cation}}$$

Equation 3.5

$$X_{i,anion} = \frac{n_{i,anion}}{\sum_i n_{i,anion}}$$

Where X_i denotes the ion fraction of the i-th ion and n_i is the number of moles of the i-th ion.

The simplest approach to express the relation between the activities and the ion fractions is given by the Tempkin's equation:

Equation 3.6

$$a_{MeO} = X_{Me^{2+}}.X_{O^{2-}}$$

However, the Tempkin's equation is not always fulfilled. This is the case when silica is present in the slag. Silicate anions are found as interlinked anions varying in both shape and size. As the content of silica in the slag increases, the interlinking of these species increases. For example, in pure silica, silicate anions exist in a three dimensional configuration. The addition of basic oxides to the slag, will lead to the formation of the O^{2-} ions, which will break the

silicate linkage. This process can be seen in Reaction 3.1 where a single chain of silicate ions is broken into two smaller ones.

Reaction 3.1

$$Si - O - Si - + O^{2-} = -Si - O - + - O - Si -$$

As the basic content of the slag increases, more free oxygen ions become available and the breaking of the silicate chains increases. This will affect a multitude of physical properties in the slag, e.g. viscosity, electrical conductivity and diffusion coefficient. Moreover, it can affect the chemistry of the slag such as the concentration of free oxygen ions. To better understand these properties, it is important to explain the thermodynamics properties in relation to the structure of silicates.

The starting point is to give the equilibrium reaction for the silicate dissociation reaction:

Reaction 3.2

$$Si_{n+1}O_{3n+4}^{2(n+2)^-} + O^{2-} = Si_nO_{3n+1}^{2(n+1)^-} + SiO_4^{4-}$$

In addition, the equilibrium constant for Reaction 3.2 can be approximated by:

Equation 3.7

$$K = \frac{X_{O^{2-}} X_{Si_{n+1}O_{3n+4}^{2(n+2)^-}}}{X_{SiO_4^{4-}} X_{SiO_4^{4-}}}$$

It is important to note that this only an approximation of the equilibrium since the ion fractions are used instead of the activities. The reason behind this approach is that ion activities cannot be measured. As a result, using the ion fraction instead can be a practical solution. As a result, the equilibrium constant will depend on the slag composition e.g., increasing basicity of the slag will decrease the equilibrium constant.

However, silicate ions exist in a wider range than that described in Reaction 3.2. For a given binary silicate melt, the concentration of the individual polyanions is dependent on their respective equilibrium constants. Nevertheless, one can employ a simpler approach by assuming that the dissociation equilibrium constant is the same independent of the position in the polyanion. In other words, that all positions are thermodynamically equivalent and as a result, only straight lined chains occur. Many theoretical models exist to calculate the concentration of the silicate anions and free oxygen ions by using the activities of the basic components of the system. One such model was developed by R. Masson [17], and led to the formulation of the following expression:

Equation 3.8

$$\frac{1}{X_{SiO_2}} = 2 + \frac{1}{1 - a_{MeO}} - \frac{1}{1 + a_{MeO}\frac{1}{K_{11} - 1}}$$

Where K_{11} is the equilibrium constant for the following reaction:

Reaction 3.3

$$2SiO_4^{4-} = Si_2O_7^{6-} + O^{2-}$$

As it was already mentioned, assuming all positions are thermodynamically equivalent, this expression can be applied to reaction similar to the one given in Reaction 3.2. It can be seen from Equation 3.8 that K_{11} can be calculated by knowing a_{MeO} and X_{SiO_2}. Finally, by having the value of K_{11}, the concentration distribution of the anionic complexes can be calculated. This only applies for $X_{SiO_2} \leq 0.5$, since at higher concentrations three-dimensional chains are formed.

In melts containing only one cation ($X_{Me^{2+}} = 1$), the Tempkin's equation results in:

Equation 3.9

$$a_{MeO} = X_{O^{2-}}$$

Moreover, Equation 3.8 reflects the relationship between the silica content and free oxygen ions concentration. In other words, the concentration of the free oxygen ions serve as an indication of the melt basicity [18].

The equilibrium constant K_{11} was calculated for different binary silicate melts, e.g. for CaO-SiO_2 (K_{11}=0.0016), MnO-SiO_2 (K_{11}=0.25) and FeO-SiO_2 (K_{11}=1) at 1600^0C [17]. In addition, the silicate ion distribution was also calculated (Figure 3.2) [17]. It was found that in CaO-SiO_2 systems, SiO_4^{4-} predominates and is found exclusively at X_{SiO_2}=0.33. For the other systems, SiO_4^{4-} was also present in the highest proportion but ions with higher molar mass started to be present in greater extents. Moreover, calculations showed that at X_{SiO_2}<0.33, the ion fraction of all the different silicate ions decrease whereas on the other hand the concentration of free oxygen ions increases. The sharpest variations were observed in the CaO-SiO_2 system.

The importance of the ion theory lies in the fact that it allows us to draw conclusions concerning the effect of the slag constituents on different refining processes, e.g. desulphurization and dephosphorization.

Reaction 3.4

$$[S] + (O^{2-}) = (S^{2-}) + [O]$$

Reaction 3.5

$$2[P] + 5(Fe^{2+}) + 8(O^{2-}) = 2(PO_4^{3-}) + 5[Fe]$$

It can be seen from the above equations that the activity of the free oxygen ion plays a decisive role in determining the extent of these refining processes. The conclusions that can be drawn from the ion theory model are:

1. Free oxygen ions play an important role in dissociating silicate anion complexes and as a result are consumed during this process. When all silicate complexes are present as SiO_4^{4-} ions the process stops. This behavior is observed at $N_{SiO_2} = 0.33$ for divalent cations, and at different SiO_2 molar fractions for other slags, becoming increasingly pronounced for more basic oxides.

2. The activity of the free oxygen ion becomes larger following the sequence $FeO \rightarrow MnO \rightarrow CaO$ (at a given mole fraction). In addition, looking at the concentration distribution of the different silicate ions, the proportion of the SiO_4^{4-} monomer increases in the same order above.

By taking into account these two conclusions, steel producers generally employ CaO as the main basifier, and aim to have a CaO:SiO_2 >2 (e.g. N_{SiO_2}<0.33) to enhance the dephosphorization and desulphurization efficiency of the industrial slags.

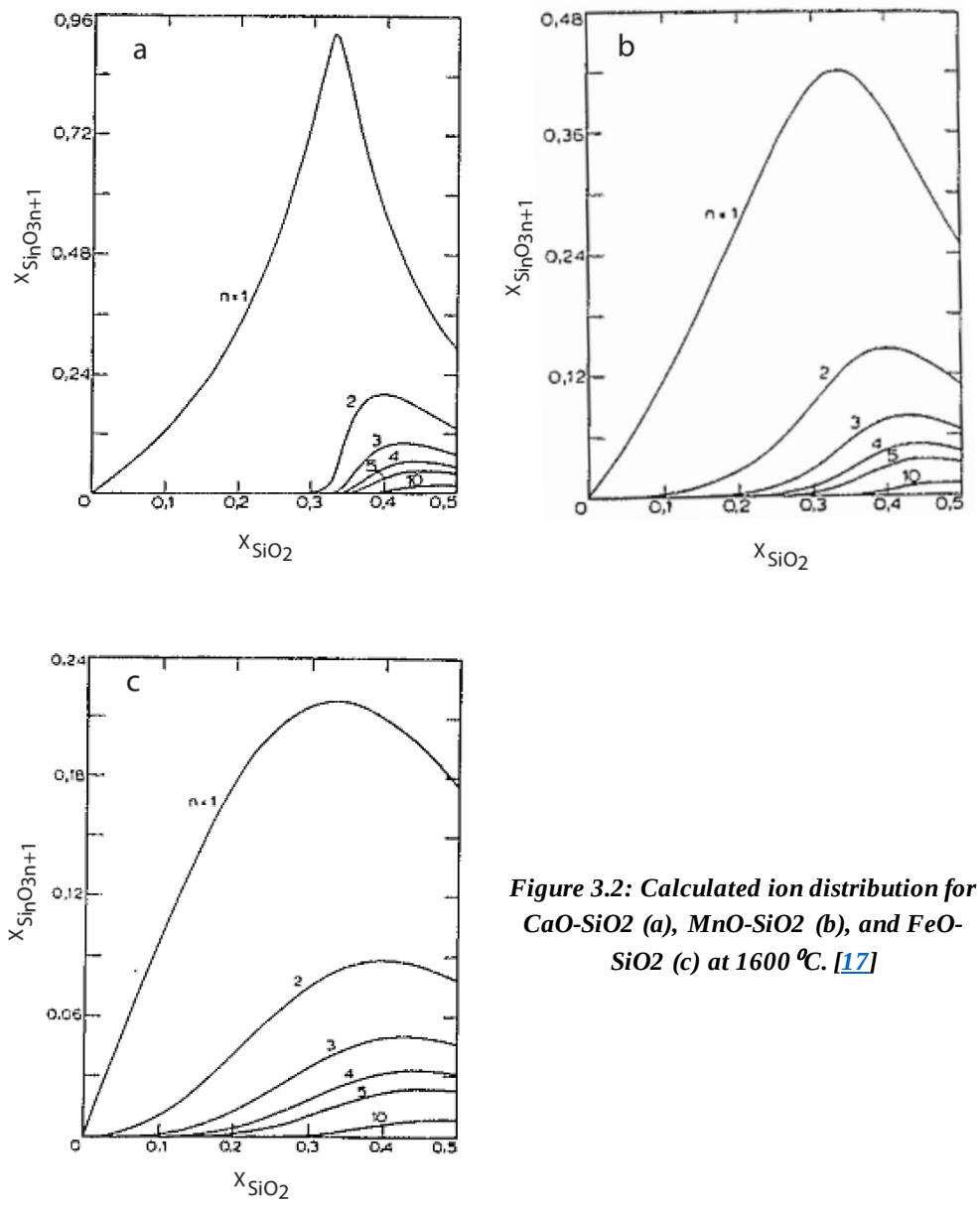

Figure 3.2: Calculated ion distribution for CaO-SiO2 (a), MnO-SiO2 (b), and FeO-SiO2 (c) at 1600 ^{o}C. [17]

3.3 Phosphorus oxidation

Slag refining is the main industrial process of P refining from iron/steels. In addition, literature references are widely available discussing the fundamentals of this technique and possible improvements. However when it comes to industrial practices producing low phosphorus steel can be challenging especially when operating at high temperatures. Consequently, the main

practice in the industry is to use a highly basic slag, which leads to increased cost of production and have negative impact on the environment. The following section is based on the work of Basu et al. [19].

The dephosphorization reaction can be written as:

Reaction 3.6

$$2[P] + 5(FeO) = (P_2O_5) + 5Fe\ ,$$

Equation 3.10

$$\Delta G^0 = -95800 + 295{,}17T\ (\frac{J}{mol})$$

And the equilibrium constant for this reaction is:

Equation 3.11

$$K_{P-P2O5} = \exp\left(\frac{-\Delta G^0}{RT}\right) = [a_{P2O5}.(a_{Fe})^5]/[\%P.f_P.(a_{FeO})^5]$$

Where (a) is the activity and (f_P) is the Henrian activity coefficient of P.

By investigating the two equations above, one can extract the thermodynamics condition required for good dephosphorization, which are:

- Low temperature
- High activity of FeO
- Low activity of P_2O_5

The activity of P_2O_5 is the product of its activity coefficient and its molar fraction. Hence, two possible paths can be followed to lower it. Either by reducing the activity coefficient by adding basic slag components (CaO) since P_2O_5 itself is acidic. Alternatively, one can reduce the molar fraction by diluting the solution, in other words increasing the slag volume.

The removal rate of P from the metal bath can be given as:

Equation 3.12

$$-\frac{d[\%P]}{dt} = a_v k_p(\%P - \%P_{eq})$$

Where (a_v) is the slag-metal area and (k_p) is the mass transfer coefficient of P in the metal. Consequently stirring will increase the rate of the reaction since it increases both (a_v) and (k_p) values. In addition, higher temperatures increase the (k_p) value. However higher temperatures, will lead to higher P_{eq} values. Finally, this equation shows that the lower the phosphorus content (%P), the more difficult it is to produce ultra-low P-steels.

Now we move on to discuss the effect of iron oxide concentration. Since the activity of FeO is the product of its activity coefficient and its molar fraction, it is commonly believed that higher levels of FeO will lead to improved dephosphorization. However, investigations in the past few decades showed that increasing the FeO concentration above certain levels is counterproductive. This is presented in Figure 3.3 [20]. It can be seen that for a specific silicon content, the highest dephosphorization is obtained for intermediate values of FeO in the slag(about 17wt%).

In addition, another study [21] came up with similar conclusion and the results are presented in Figure 3.4. In this case, highest dephosphorization is obtained when Fe content is with 15-18wt%. The main reason behind these observations is that the activity coefficient of P_2O_5 reaches its minimum around 15-18wt% FeO (Figure 3.5) [22].

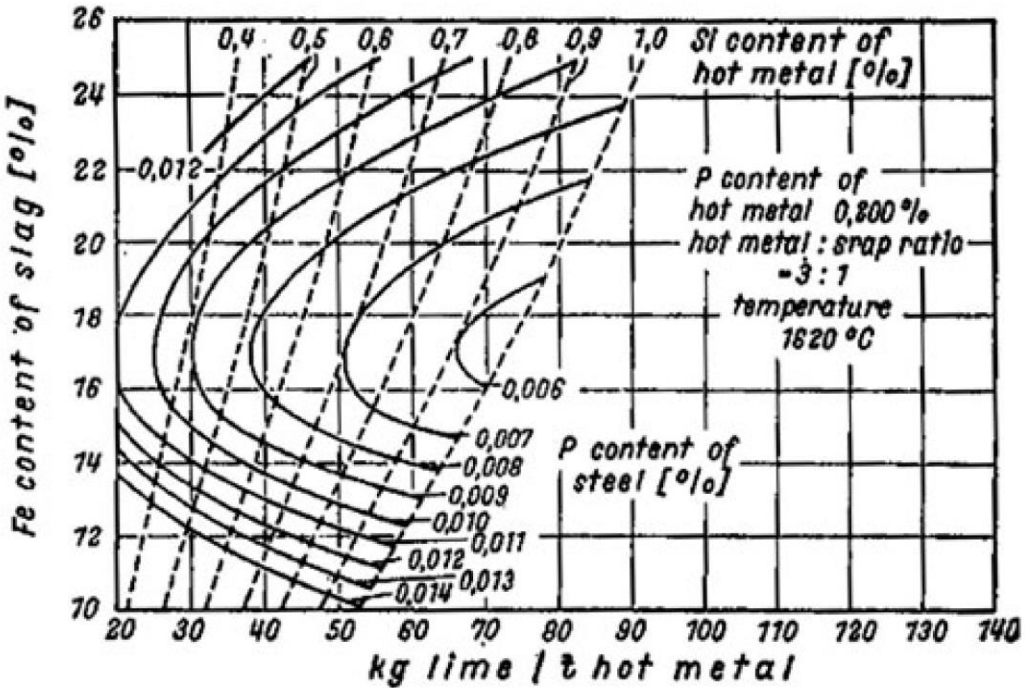

Figure 3.3: Nomogram correlating %Fe_{total} in slag (containing dicalcium silicate), %Si in hot metal, %P is steel and specific lime consumption[20]

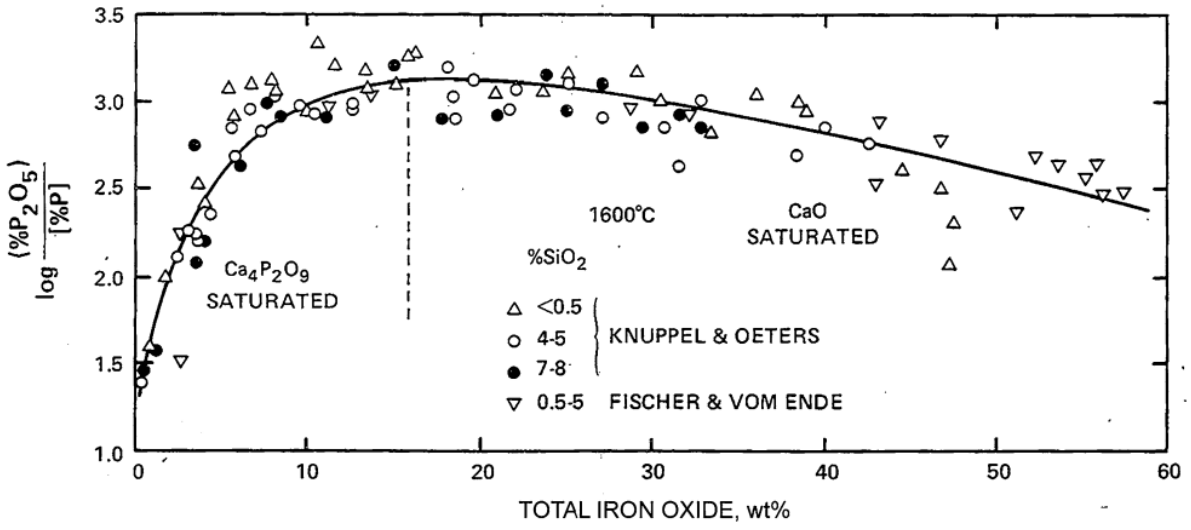

Figure 3.4: Phosphorus distribution between liquid iron and steelmaking slag saturated with CaO or Ca-phosphate[21]

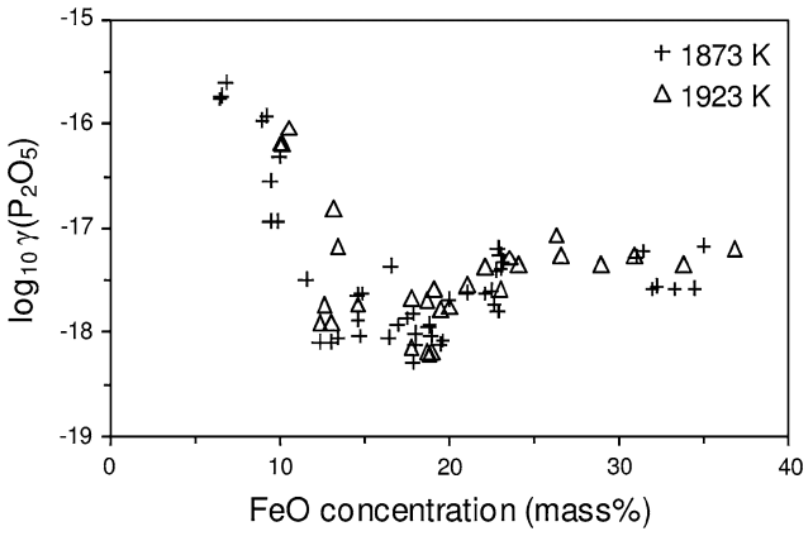

Figure 3.5: Influence of FeO concentration in slag on activity coefficient of P_2O_5 [22]

It is also important to discuss the role of CaO. Usually, basic slags with excess CaO are used in the industry. However, a recent study [22] shows that increasing the slag basicity beyond 2.5 does not lead to further increase in the phosphorus partition between slag and metal (Figure 3.6).The reason behind this observation is that at higher CaO content solid phases start to

appear in the slag, limiting further increase in dephosphorization. The positive effect that is seen in the industry is related to the larger volume of slags, which dilutes P_2O_5.

From these observations, one can conclude that the ideal slag chemistry is 15<%FeO<20 and 2.5<%CaO/%SiO_2<3. However, operators in the industry will favor having higher FeO content and basicity. This can be related to the following reasons:

- True slag basicity(calculated on the basis of dissolved lime) is often less than apparent slag basicity due to the presence of large amount of free lime.
- Higher FeO content helps in digesting CaO(by forming calcium ferrites)
- Higher slag volume since extra lime is added

Consequently, each steel producer will use different parameters that best suit its operations.

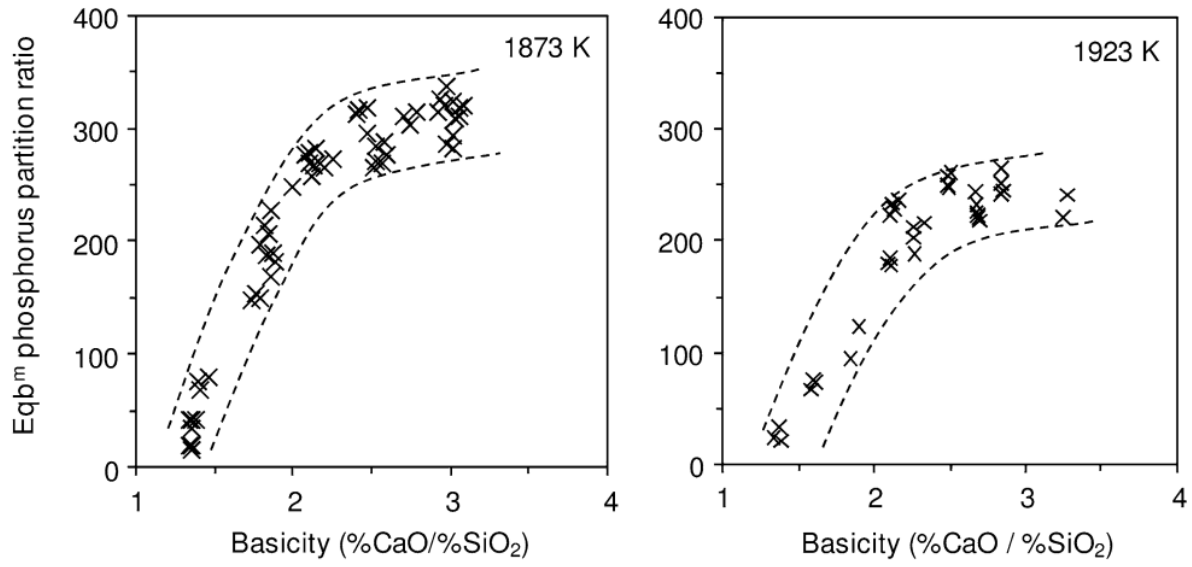

Figure 3.6: Equilibrium partitioning of Phosphorous between slag and metal [22]

In a recent study carried out by Hou et al. [3], ilmenite and high phosphorus iron ore smelting using oxygen enriched top blown process was investigated. The following discussion is based on their work. This is an important study since the process investigated in it is similar to the one carried out at Tyssedal. The effect of the different parameters such as temperature, slag basicity and ventilation time on the final product quality was studied.

At higher reduction temperatures, a higher Fe recovery rate was obtained relating to the higher solubility of the undissolved elements in the slag at higher temperatures. This in turn leads to a lower viscosity and enhanced kinetics. However, the dephosphorization rate decreases with increasing temperature since the dephosphorization reaction is exothermic (Figure 3.7). Hence,

to obtain low-P hot metal and high Fe recovery rate, temperatures around 1500°C should be used.

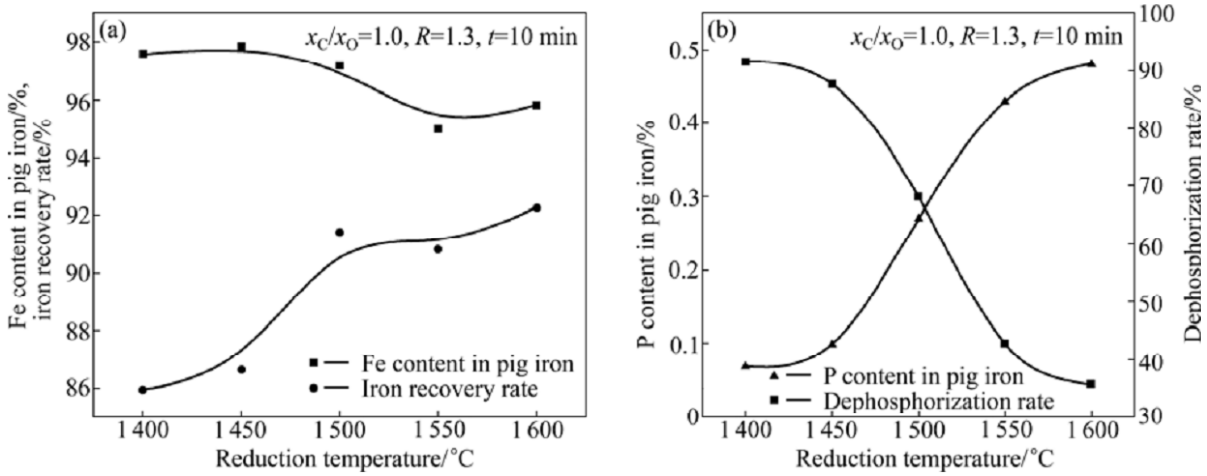

Figure 3.7: Relationship of Fe content in pig iron, iron recovery rate (a), P content in pig iron and dephosphorization rate (b) to reduction temperature [3]

In addition, the effect of basicity (denoted R in their work) was also studied in a CaO, FeO and SiO_2 slag. It was found that Fe recovery had its maximum value at basicity equal to 1.3. This can be explained by the fact that combination between CaO and SiO_2 increases the stability of the slag and as a consequence the activity of FeO. However, at higher basicity Fe recovery rate drops sharply caused by the increased viscosity of the slag due to excessive amounts of CaO, which slows the kinetics down. On the other hand, dephosphorization rate increased at higher basicity up to basicity equal 1.5 (Figure 3.8). The enhancement of basicity increases the number of O^{2-} in molten slag, hence improving the phosphate capacity. As a result, the optimal slag basicity is around 1.3 in order to ensure both a good dephosphorization and Fe recovery ratio.

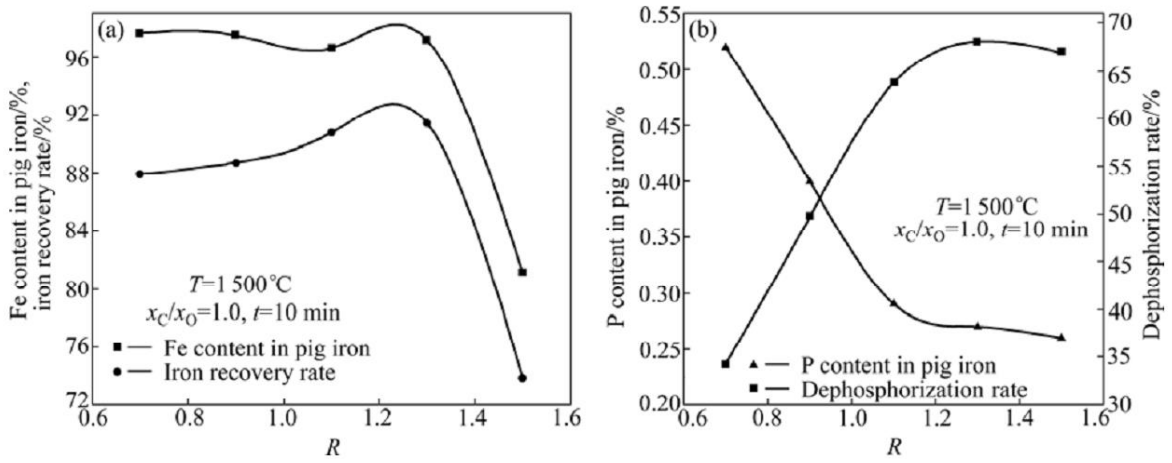

Figure 3.8: Relationship of Fe content in pig iron, iron recovery rate (a), P content in pig iron and dephosphorization rate (b) to basicity [3]

Moreover, oxygen-blowing time was also studied. At longer blowing durations, Fe recovery rates decrease slightly whereas dephosphorization rates show an increase (Figure 3.9). This result is attributed to the fact that oxygen blowing induces stirring in the melt enhancing the kinetics of the system. However, at very long periods, Fe can also be oxidized easily into ferrous oxide, causing a decrease in the Fe recovery rate.

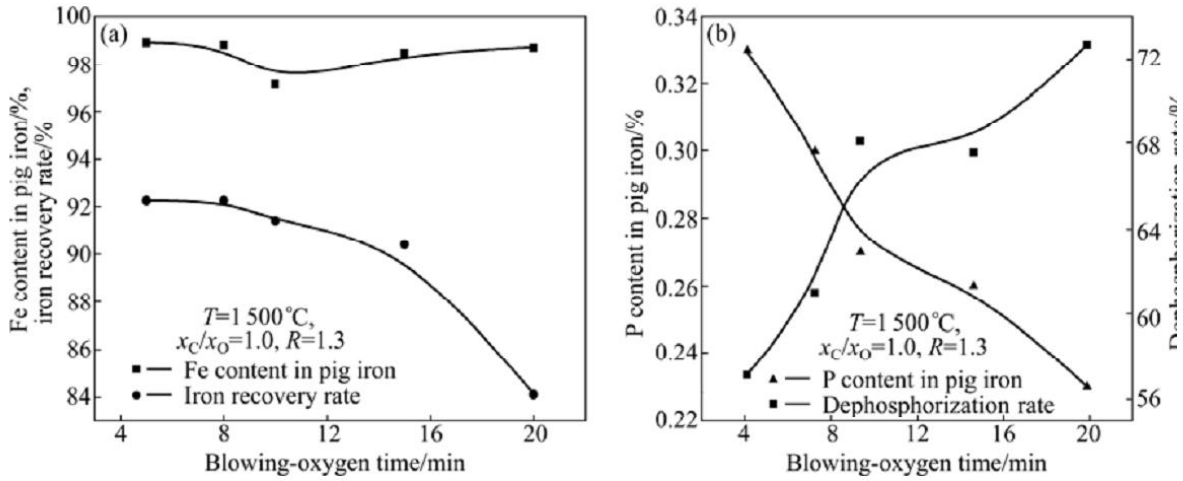

Figure 3.9: Relationship of Fe content in pig iron, iron recovery rate (a), P content in pig iron and dephosphorization rate (b) to blowing- oxygen time [3]

The general problem with ilmenite smelting is the formation of foaming slag caused by the formation of Ti(C, N) compounds. However, in top-blown smelting reduction with oxygen enrichment, this is not a big concern since TiO_2 content in the slag will be diluted. Moreover, by using the right set of conditions both high Fe recovery and dephosphorization rates can be obtained.

3.4 Slags for oxidation reactions

This section and the following subsections (3.4.1 to 3.4.6) are based on the work of F. Oeters in Metallurgy of Steelmaking [13]. Many of the references he uses are in German. Hence, it was impossible to read and comprehend them. However, when figures from those works were used they were referenced. The main components of slags produced in the refining processes of ion/steel are CaO, SiO_2, FeO_n, MnO and MgO. CaO is added to basify to slag and as a result to remove both phosphate (PO_4^{3-}) and sulfate (S^{2-}) ions in the form of $Ca_3(PO_4)_2$ and $CaS.SiO_2$. FeO_n and MnO are the result of the oxidation of iron whereas MgO is the result of the reaction between the melt and the refractory materials (either as pure MgO or dolomite, with the latter being a mixture of MgO and CaO). To better understand the role of these components in metallurgical processes, it is important to look at some of their phase diagrams. The focus will be on systems of relevance to the thesis.

3.4.1 The iron-oxygen system

The phase diagram is shown in Figure 3.10 [23]. The most important region of the phase diagram is the temperature range where liquid phases are present, which is directly related to many applications in the steel industry. The liquid region of the phase diagram consist of 2 phases: liquid metal and liquid oxide. Moreover, a miscibility gap exists which contain these two phases. Liquid iron is present in the far left of the diagram, and the melting point of pure iron is 1536^0C (point A). The dissolution of oxygen lowers the melting point of iron, reaching a minimum of 1528^0C at 0.16%O (Point B). At this point, liquid iron is in equilibrium with iron oxide melt containing 22.6%O (Point C). At higher temperatures, oxygen containing iron and oxide melt remain in equilibrium. However, with increasing temperature, the oxygen content in the metal increases whereas it decreases in the oxide melt, and as a result, the miscibility gaps becomes smaller. At 2046^0C, the solubility of oxygen in the iron is 0.83% (highest temperature where data exist [24]. At this temperature, the iron is in equilibrium with an oxide melt containing 22.4% O, and the oxide melt can be referred to as $FeO_{1.0045}$. The oxide melt has a lower melting point than iron, and hence with decreasing temperature it becomes in equilibrium with δ-iron (1400^0C -1528^0C), then with ϒ-iron (1371^0C -1400^0C). At T<1371^0C, the oxide becomes solid. At this stage, three phase are in equilibrium: ϒ-iron, wustite and oxide melt (points N and J). The melting point of the oxide increases with increasing oxygen content. Along the line NI, we can see that equilibrium exists between the oxide melt and wustite, where

the latter showing increasing oxygen content with that of the oxide (line JH), where at point H wustite has its highest oxygen content. When the temperature reaches 1424^0C, three phases are in equilibrium: oxide melt, wustite and magnetite. The melting point of magnetite lies at 1597^0C, which is a congruently melting oxide (point V). At higher oxygen contents, the oxide melt is in equilibrium with magnetite and in this region, oxygen can be absorbed by magnetite to form a solid solution. At the points R and R' (T=1583^0C), the oxide will be in equilibrium with oxygen having partial pressure of one atmosphere.

The most important point in this description of the phase diagram is that the liquid oxide melt region extends from equilibrium with iron melt when $pO_2 = 10^{-8}$ bar to equilibrium with oxygen with $pO_2 \approx 1$bar. Hence, the higher the oxygen content of the oxide melt, the higher its content of trivalent iron (Fe^{3+}).

The equilibrium can be written as:

Reaction 3.7

$$(Fe_2O_3) = (FeO) + 1/2\,O_2$$

And the equilibrium constant:

Equation 3.13

$$K = \frac{a^2_{(FeO)} \cdot p^{1/2}_{O_2}}{a_{(Fe_2O_3)}}$$

Hence, it can be noted that a precise of value of trivalent and divalent iron is bonded to each oxygen content in the oxide melt, which in turn are in equilibrium with the partial pressure of oxygen in the gas phase.

In the refining processes, where the hot metal is treated to obtain steels, pure iron oxide melts are not usually formed. Iron oxide is present usually with the oxides of other impurities (e.g. P_2O_5, SiO_2) forming a slag phase. The same approach can be followed for the iron oxide content of these slags in equilibrium with oxygen partial pressure of the gas phase. The most important point is to note that when a slag is in contact with iron melt, divalent iron is the main dominant species in the slag, whereas trivalent iron is dominant when in contact with air or oxygen. This is of significant importance in refining processes since oxygen transport is enhanced by the diffusion of divalent iron from the bottom part of the slag(in contact with the metal) to the top, and vice versa trivalent iron is transported from the top region of the slag (in contact with air) to the bot part of the slag. Moreover, the movement of the different species can stir the melt.

In the pure oxygen–iron system, the equilibrium between the iron oxide containing slag and the iron lies on line NGCC' in Figure 3.10. In addition, in multicomponent slag systems, the equilibrium can be determined if the concentrations of all the other elements is already

determined. Moreover, the ratio of divalent to trivalent iron, and as a consequence the oxygen potential of the slag is fixed when equilibrium is reached with the iron melt. As a result, one can find the oxidizing state of the slag by indicating the total iron content. However, in some cases, FeO_n amount is used instead, with n referring to the total amount of oxygen bound to iron.

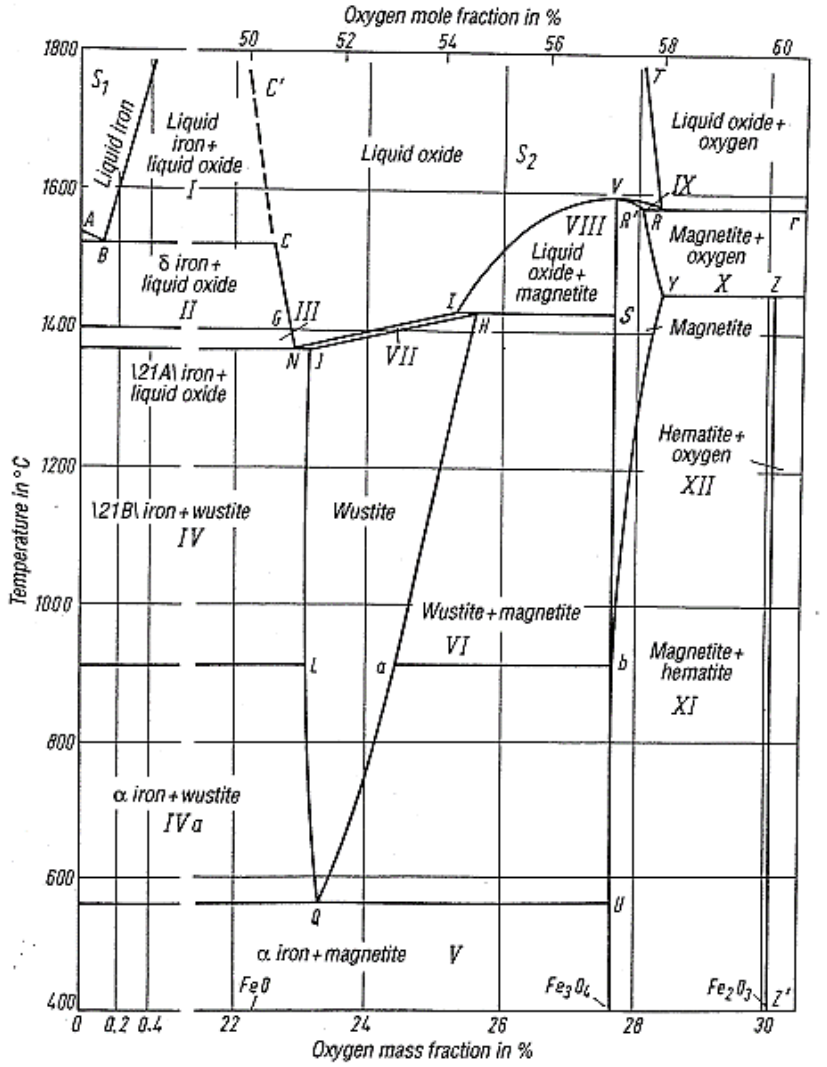

Figure 3.10: Iron-oxygen phase diagram (adapted from [23])

When the slag and the metallic iron are in equilibrium, oxygen in the iron can react with the iron oxide in the slag:

Reaction 3.8

$$(FeO) = [Fe] + [O]$$

And the equilibrium constant:

Equation 3.14

$$K_{FeO_n} = \frac{[a_O]}{(a_{FeO_n})}$$

Equation 3.15

$$\log_{10} K = -\frac{6320}{T} + 2.765 \quad [25]$$

One interesting condition worth mentioning is when the slag consist of pure iron oxide, hence $(a_{FeO_n}) = 1$ and $[a_O] = [a_O]_{saturation}$. Equation 3.14 will lead to:

Equation 3.16

$$(a_{FeO_n}) = \frac{[a_O]}{[a_O]_{saturation}}$$

The main application of this equation is that the activity of the iron oxide can be determined by knowing the oxygen content of the iron melt at equilibrium.

3.4.2 FeO-Fe_2O_3-CaO system

The first important feature of this system is the fact that it should be regarded as a ternary system. The reason is that the presence of lime leads to the formation of ferrite ions (e.g. $Fe_2O_4^{2-}$ or $Fe_2O_5^{4-}$) from trivalent iron , even if the slag is in equilibrium with molten iron. However, as mentioned the previous section, the ratio of divalent to trivalent iron is fixed by knowing the total iron content under equilibrium condition. Hence, it is suitable to present this system as a FeO_n–CaO binary system. This system has two important applications:

1. When in equilibrium with the metallic phase to study the metal-slag reactions.
2. When in equilibrium with the air or oxygen to study the slag-gas reactions.

The phase diagram is shown in Figure 3.11 [26]. The main characteristic of this system is a eutectic at 1130^0C and high peripheral solubility in the solid state. As a result, iron oxide is a very suitable flux for lime, playing a big role in its dissolution. The process of lime dissolution is first by the formation of a lime rich solid solution in the peripheral region, which is dissolved later. One feature, that validate the assumption that the system is ternary, is the presence of the incongruently melting dicalcium ferrite ($2CaO.Fe_2O_3$). The peritectic reaction between this compound and the melt leads to the precipitation of iron and a change in the valency according to the following reaction:

Reaction 3.9

$$\langle 2CaO.Fe_2O_3 \rangle_{solid} + \langle Fe \rangle_{solid} = [2(CaO) + 3(FeO)]_{melt}$$

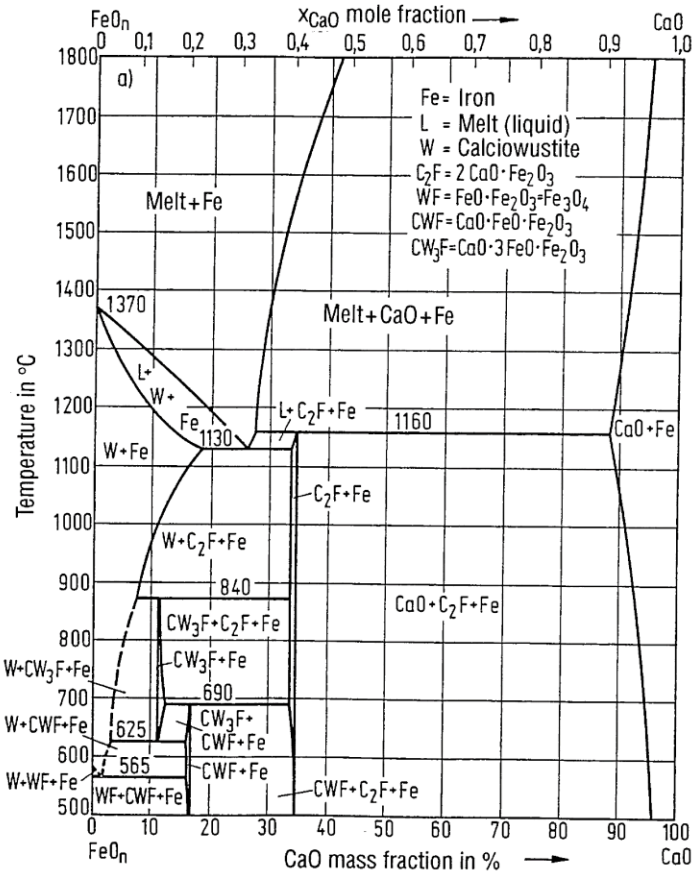

Figure 3.11: FeO_n-CaO phase diagram [26]

In this system, both lime and iron oxide show negative deviation from ideality when looking at activity [26, 27]. This is an indication of compounds formation and explain the tendency of iron oxide to combine with lime to form dicalcium ferrite.

The system in equilibrium with air is shown in Figure 3.12 [26]. Since hematite decomposes at 1393^0C (since pO_2=0.21bar), only magnetite is stable at higher temperatures. Moreover, the peripheral solubility is of little importance here since lime and iron (III) oxide have very different crystal structures and solid solution is difficult to form. Moreover, two new compounds exist in this system, $CaO.Fe_2O_3$ and $CaO.2Fe_2O_3$, which leads to the same conclusion that iron oxide is a very good flux for lime.

To better understand the effect that lime additions have on this system, it is a good idea to start with the Fe-O-CaO system (Figure 3.13) [28]. The oxygen range is limited from zero to 40wt% since Fe_2O_3 is the compound containing the highest oxygen content of 30wt% O. Note that the scales of the two triangles in Figure 3.13 are different. First, addition of lime will change the line indicating saturation with wustite and magnetite in the Fe-O system to areas. These areas will move toward lower temperatures with increasing lime content. Moreover, the different areas present are denoted: Fe_s (iron saturation, W (wustite saturation), H (hematite saturation) and M (magnetite saturation), the aforementioned regions are limited by areas of lime containing solid phases at high CaO content. Also many features are presented in Figure 3.13, e.g. point A is the incongruent melting point of dicalcium ferrite whereas B is the eutectic point between CaO and $2CaO.Fe_2O_3$ and line AB separated the saturation area of calcium ferrite from that of lime.

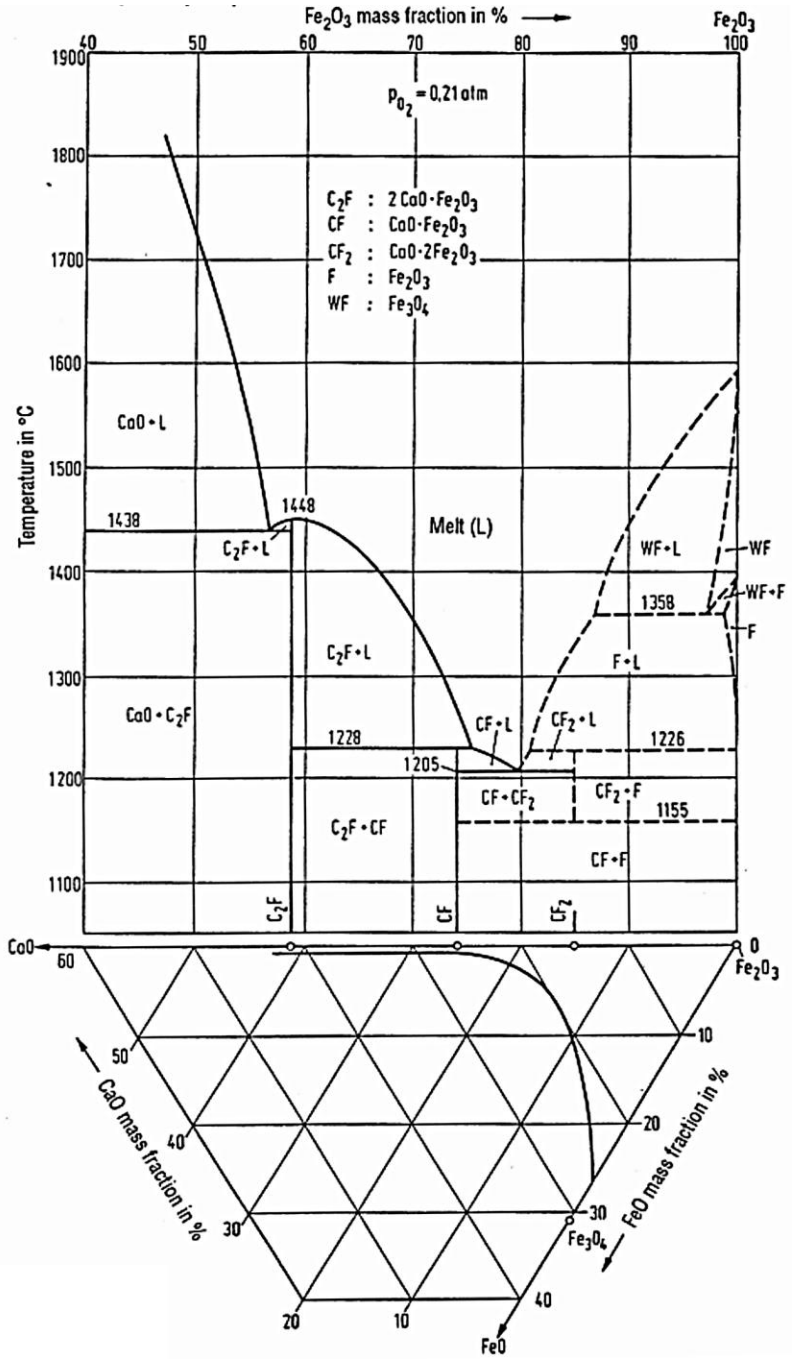

Figure 3.12: CaO-Fe2O3 phase diagram [26]

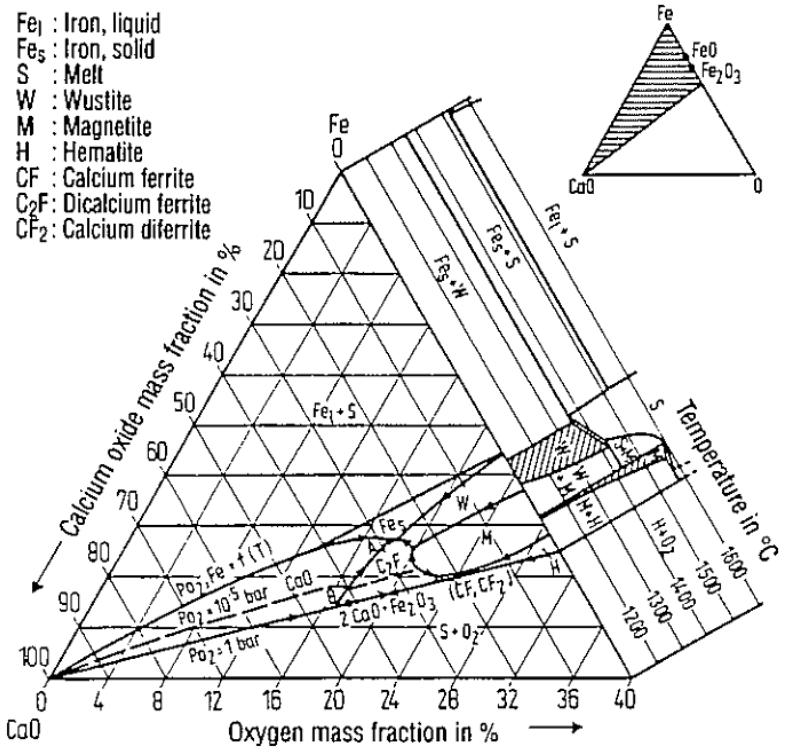

Figure 3.13: Schematic representation of the Fe-O-CaO system [28]

This phase diagram was supported by measured values by R. Scheel [28] and in more recent studies by E. Schürmann et. al. [29] and by S. Hara et. al. [30]. The two industrially important slag systems are those, which are simultaneously saturated with iron and lime, or those saturated with dicalcium ferrite and lime (Figure 3.14).

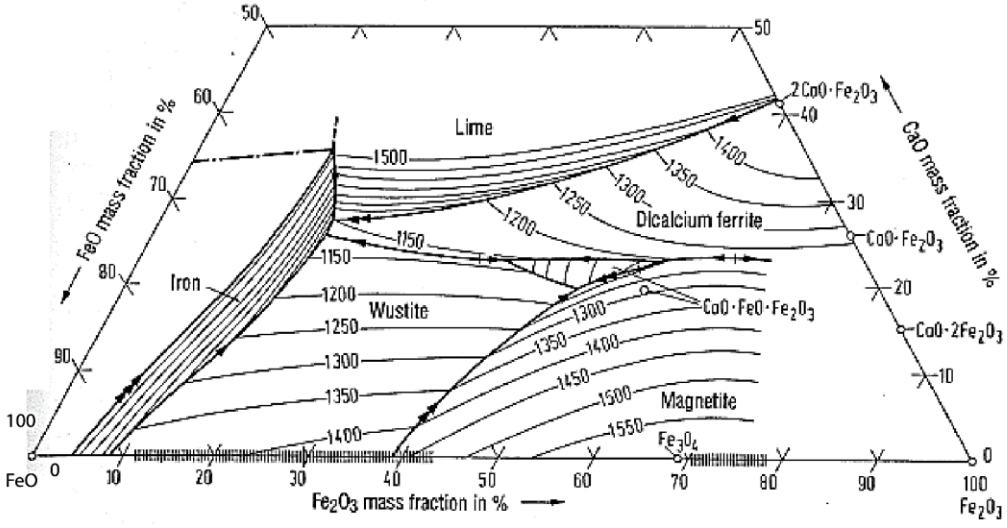

Figure 3.14: FeO-Fe$_2$O$_3$-CaO phase diagram [29]

3.4.3 The MgO-FeO-Fe_2O_3 system

The importance of this system is related to the behavior of dolomite or magnesite bricks used as refractory materials or lining in the metallurgical vessels in the steel industry. This system is studied in equilibrium with iron or with air, and systems are exactly binary and they follow the same aspects as in the case with lime (Figure 3.15) [26]. Since both FeO and MgO have a rock salt structure and similar lattice properties, a constant miscibility gap exist between those two compounds. This leads to the formation of magnesiowustite. Moreover, miscibility between MgO and Fe_2O_3 also occurs but to a limited extent due to the formation of magnesioferrite, a spinel compound. In addition, another important feature of this system, is the ability of magnesiowustite to dissolve Fe_2O_3, where trivalent iron Fe^{3+} enters the lattice and substitute for divalent ion hence simultaneously creating vacancies to achieve electro neutrality [31].

One example, which pinpoints the importance of the behavior of magnesiowustite in magnesite bricks, is its ability to absorb FeO from oxygen-containing iron melts (can absorb up to 75% FeO at 1600^0C), and then rereleasing it at later stages, i.e. in deoxidized melts.

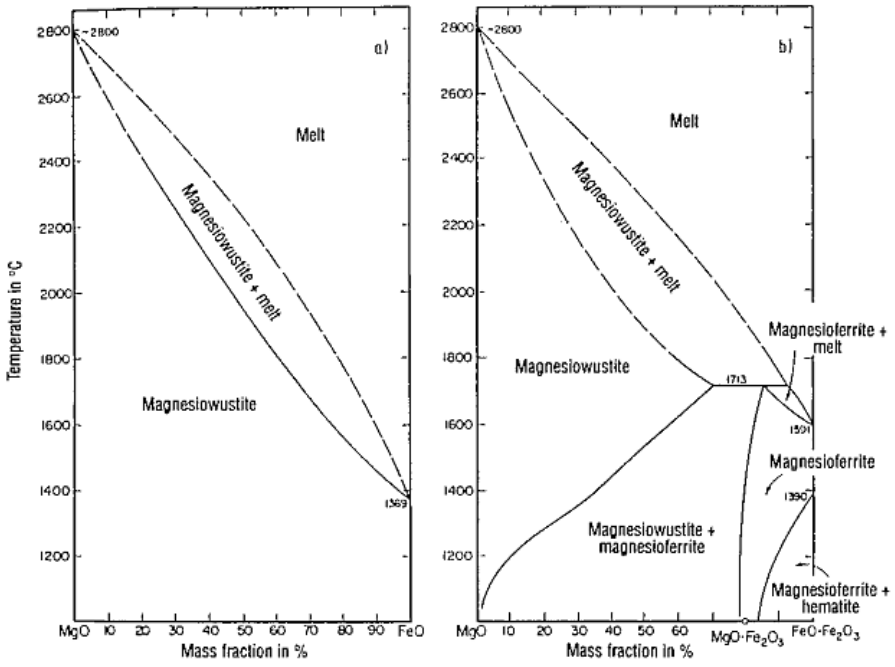

Figure 3.15: Phase diagrams of magnesium oxide–iron oxide system in equilibrium with metallic iron (a) and in equilibrium with air (b).[26]

Finally, the MgO-Fe_2O_3 system is the starting point for magnesite bricks manufacturing, where Fe_2O_3 plays the role of a binder and a crystallizing agent, dissolved in magnesioferrite or

magnesiowustite. This affects the temperature limit of effective wear resistance of these bricks, which is determined by the iron oxide content, i.e. shown by the liquidus line.

3.4.4 The $CaO\text{-}SiO_2$ and $CaO\text{-}P_2O_5$ systems

Since the main role of lime is to act as a basifier, the $CaO\text{-}SiO_2$ (Figure 3.16) [26] and $CaO\text{-}P_2O_5$ (Figure 3.17) [26] systems are of importance to steel metallurgy. These two systems are strictly binary. Lime rich regions of both diagrams are the most important, since in metallurgical steel process achieving the highest lime content is a priority. As a result, these type of slags contain primarily solid lime, but also the compounds Ca_2SiO_4 (dicalcium silicate), $Ca_3P_2O_8$ (tricalcium phosphate) and to a lesser extent the compounds Ca_3SiO_5 (tricalcium silicate) and $Ca_4P_2O_9$ (tetracalcium phosphate).

By looking into the phase diagrams, it can be seen that Ca_2SiO_4 and $Ca_3P_2O_8$ melt at very high temperatures (with a distinctive melting point maximum) and hence are thermodynamically very stable. In solidified phosphate slags that contain silica, these two compounds occur in the form of solid solutions. At 1600^0C (typical temperature in liquid steel metallurgy), silicophosphate and dicalcium silicate often occur as solid precipitates near the undissolved lime particles. In the $CaO\text{-}SiO_2$ and $CaO\text{-}P_2O_5$ binary system, the most important liquidus lines are lime saturation, saturation with Ca_2SiO_4 and Ca_3SiO_5 for the silicates, $Ca_3P_2O_8$ and $Ca_4P_2O_9$ for the phosphates. When iron oxide is added, forming ternary systems, these lines expand to form saturation areas, which will determine both the composition and behavior of the lime-rich slags in the steel industry.

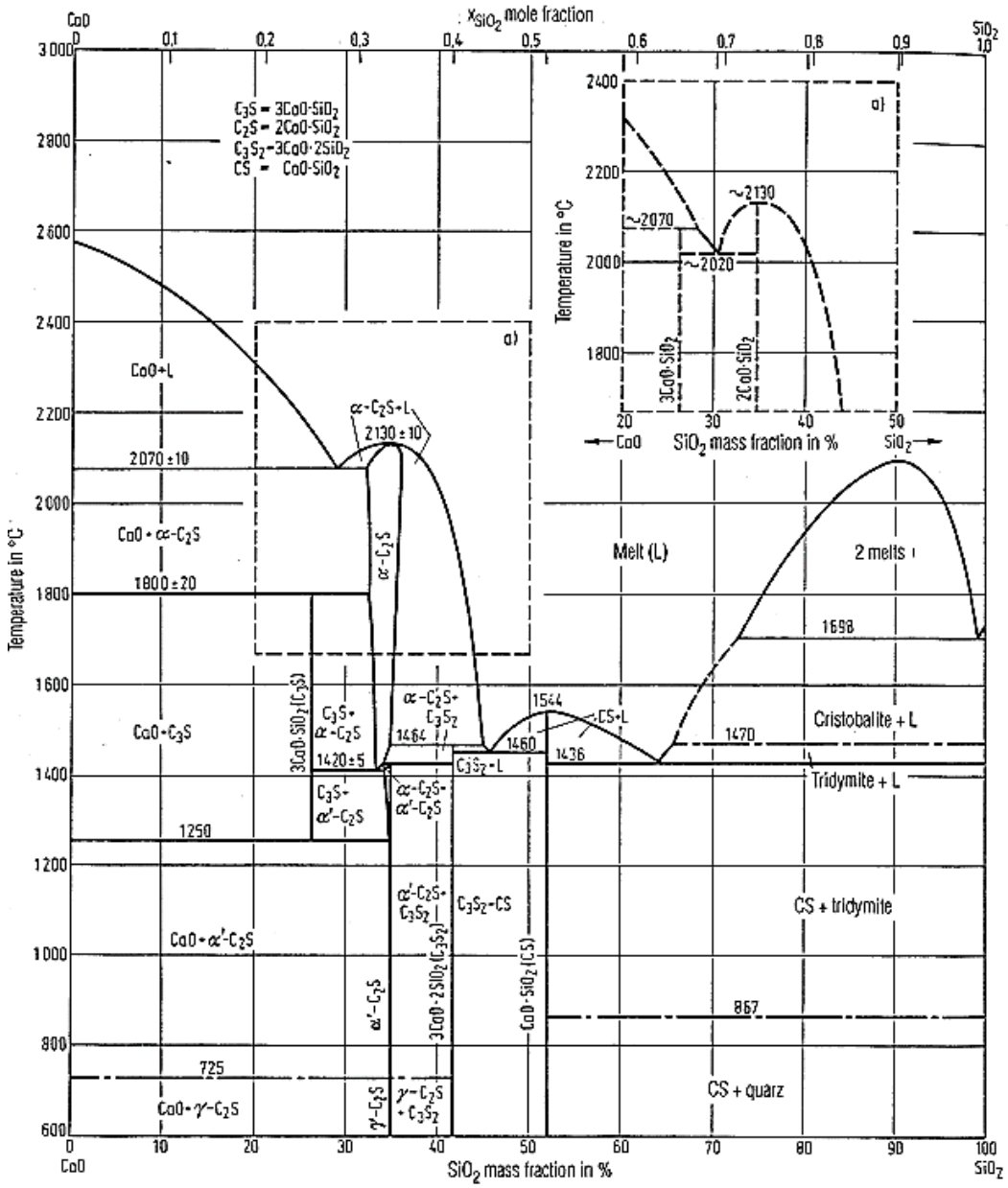

Figure 3.16: CaO-SiO_2 phase diagram. [26]

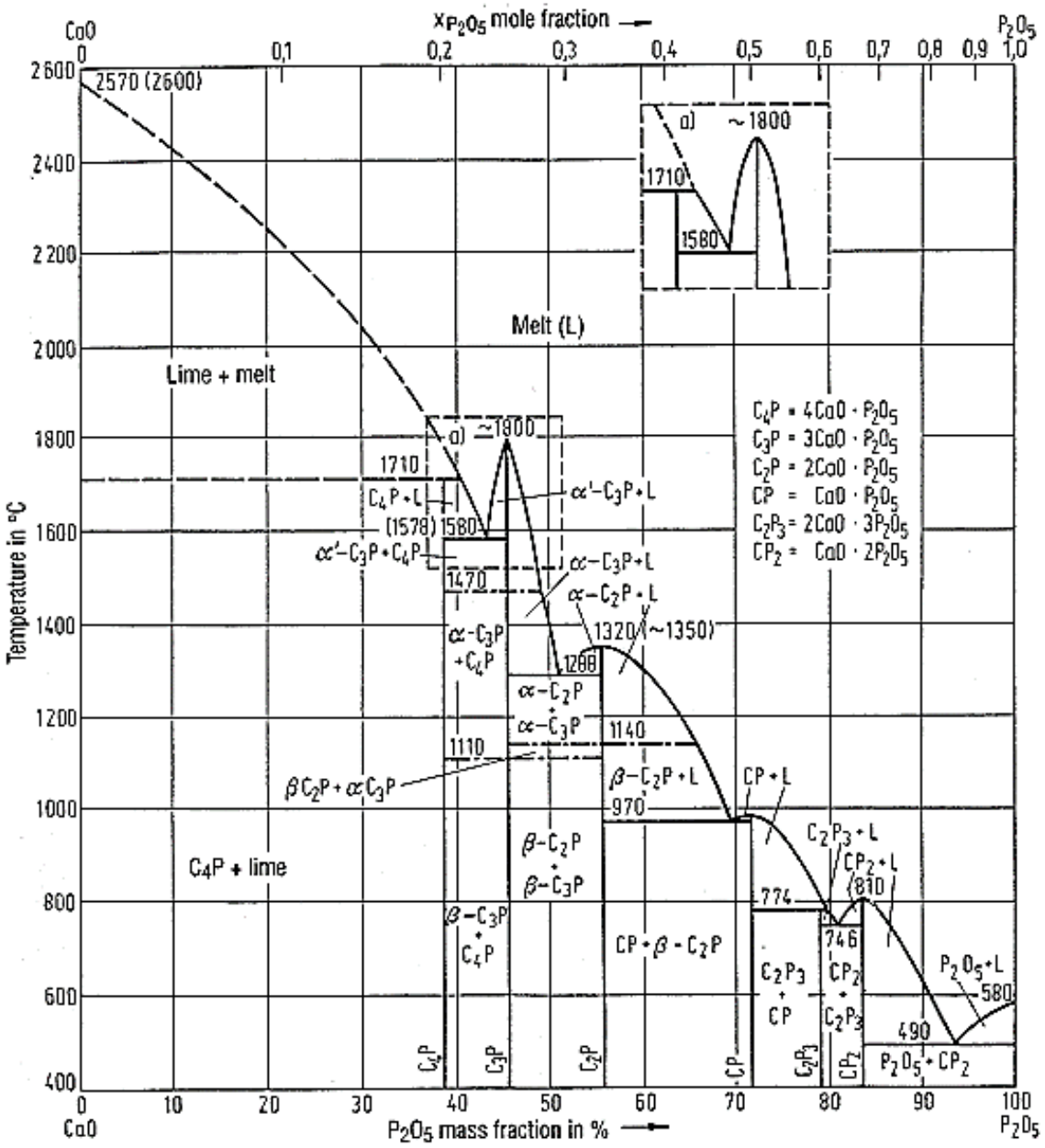

Figure 3.17: CaO-P_2O_5 phase diagram. [26]

3.4.5 The $CaO-FeO_n-SiO_2$ system

The $CaO-FeO_n-SiO_2$ system is the most important system occurring in steel production from low-phosphorus metal. The phase diagram is shown in Figure 3.18[26].It is a projection of the three dimensional ternary diagram, containing all the singular points that occur in this system. Continuous lines separate saturation areas of individual solid phases from each other and where more than one phase is precipitated during cooling. On the other hand, broken lines represent isotherms. Moreover, solid phases, which are in equilibrium with individual precipitate areas, are also shown. The most important features in the lime rich region are the saturations areas of lime, tricalcium silicate and dicalcium silicate, with the latter occupying a wide portion of the diagram. As for equilibrium with tricalcium silicate, it is found in a very narrow region of concentrations and for equilibrium with lime, it is only possible for silica content less than 10% (not often present in steel industries).

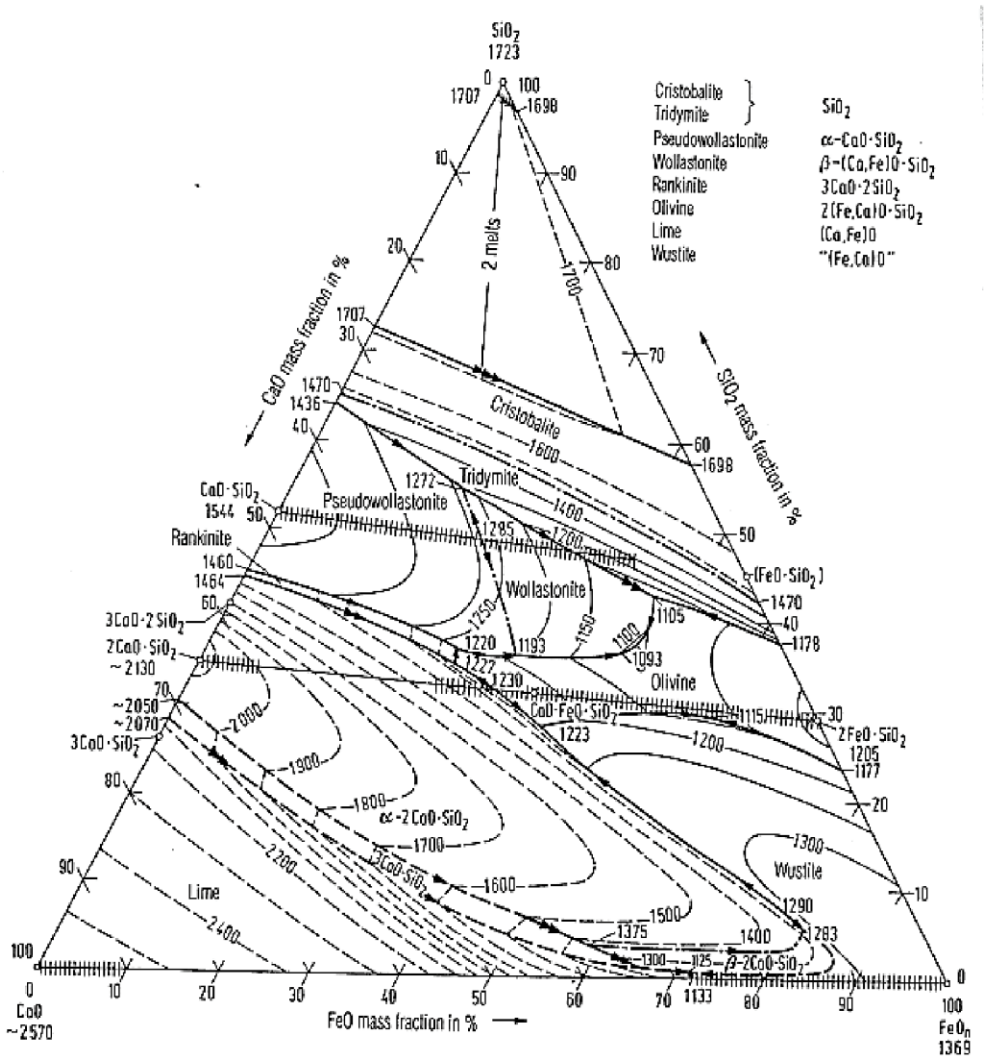

Figure 3.18: CaO-FeOn-SiO2 phase diagram. [26]

Since most metallurgical refining processes are carried out at 1600^0C, it is appropriate to discuss the phase diagram by taking an isothermal section at this temperature. Figure 3.19 [32] shows the system, and it contains FeO iso-activity lines in equilibrium with metallic iron. The areas outlined by line a-b-c-d and e-f represent the regions where the liquid slags exist at 1600^0C. By looking at the saturation areas of both dicalcium and tricalcium silicates, we can see that liquid slags are in equilibrium with the pure compounds and no solid solutions are formed in this case. Moving down to the lime saturation region, it can be seen that the solid phase consist of a solid solution of lime and iron(II)oxide rather than pure lime (already seen in the FeO-Fe_2O_3-CaO system). At 1600^0C, this solution can contain up to 6% FeO

By looking at the isoactivity lines, it can be seen that FeO in these slags does not follow ideal behavior. In By starting in the FeO-SiO_2 binary peripheral system, the activity deviates slightly in the negative direction from the ideal behavior. Moreover, by moving through a line with constant FeO_n concentration of 50 % toward the CaO-FeO_n system, the activity of FeO increases with lime content to a maximum $a_{FeO} = 0.85$ at the quasi-binary FeO_n-$2CaO.SiO_2$. However, by increasing the lime content even further, the activity of FeO decreases again. Hence, in this quasi binary system, positive deviation from ideality is observed. This is explained by the fact that the simultaneous presence of silica and lime in the slag, leads to a stronger attraction between them, then from what they exert individually in respect of iron. Therefore, iron oxide will not be able to combine with wither of them and hence will assume higher activity.

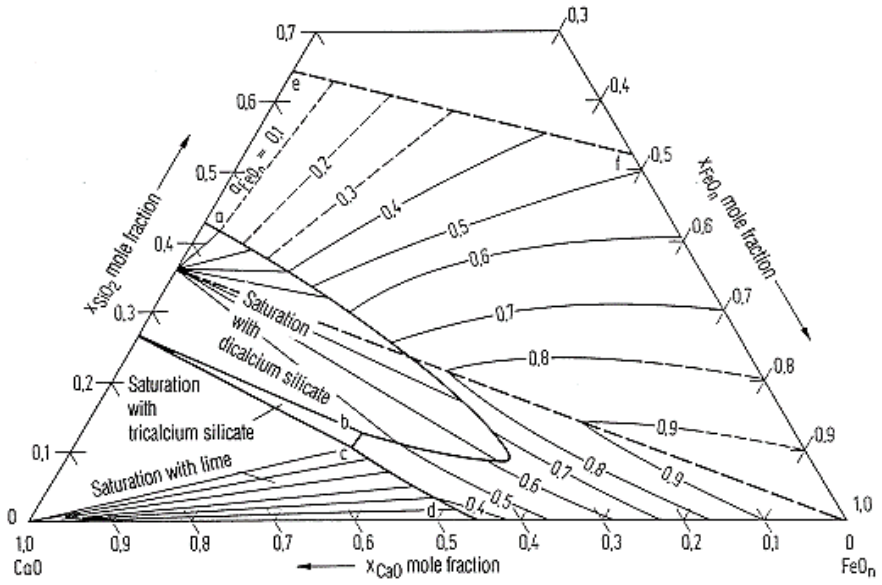

Figure 3.19: CaO-FeO_n-SiO_2 phase diagram with isoactivity lines for iron (II) oxide at 1600 ^{0}C. [32]

As for CaO activity, it increases dramatically past the quasi-binary FeO_n-$2CaO.SiO_2$ system. This is explained by the fact that all silica in the system will be present in the form of Ca_2SiO_4, and any additional lime in the system will remain free and hence the activity of CaO increases. This free lime will dissociate, supplying free oxygen ions to the system.

The components of the CaO-FeO_n-SiO_2 system make up for approximately 80% of the composition of steelwork slags. Other components include MnO (≈10%), MgO (≈2-3%) and P_2O_5, Cr_2O_3, TiO_2 and Al_2O_3 (together mounting up to ≈5-7%). In the basic CaO-FeO_n-SiO_2 system, the saturation regions in the lime-rich regions are shifted by the content values of the aforementioned oxides in the slag. One example is shown in Figure 3.20 [33], where the effect of increasing MnO and MgO content is studied.

In these types of slags, the oxygen contents in iron melt move toward equilibrium with the slag, which is determined by the activity of iron (II) oxide in the slag.

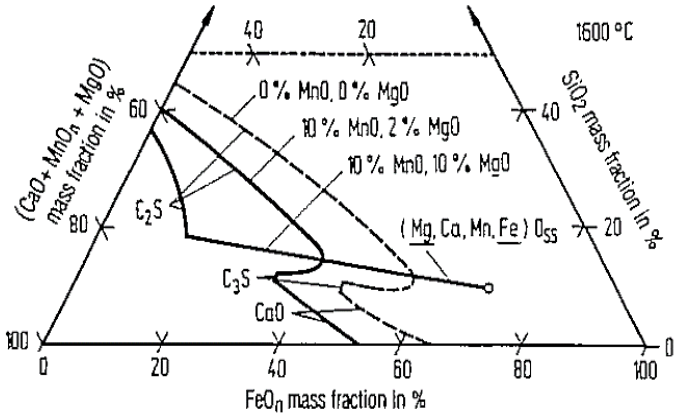

Figure 3.20: MgO and MnO influence on the slag equilibria in the Fe- FeO_n-CaO- SiO_2 system at 1600 °C. [33]

3.4.6 The dephosphorization system CaO-FeO_n-P_2O_5

The reaction describing dephosphorization in iron is given by:

Reaction 3.10

$$[P] + 5/2\,(FeO) + 3/2\,(CaO) = 1/2\,(Ca_3(PO_4)_2) + 5/2\,[Fe]$$

The only possible pathway for phosphorus oxidation and its subsequent transfer to the slag is by combining as phosphate ions. The main reason behind it is that the gaseous species P_2O_5 does not have sufficient thermodynamic stability to be an oxidation product of phosphorus in

iron melts. As a result, the first step in phosphorus removal is its oxidation at the metal-slag interface. This requires the use of a slag with high oxidation potential to oxidize phosphorus, and to be able to form and absorb the resulting phosphate ions by being sufficiently basic. The two conditions mentioned above can be fulfilled by using slags with significant amounts of iron oxide and lime. Moreover, it can be noted that phosphorus oxidation differs from that of manganese and silicon, since the oxides of the latter two can be formed without the presence of a slag, and are then capable of transfer into the slag.

The proportions of iron oxide and lime in the slag, required to ensure effective dephosphorization, are determined by the equilibrium constant of Reaction 3.10. The equilibrium constant is given by:

Equation 3.17

$$K_P = \frac{\left(a_{Ca_3(PO_4)_2}\right)^{1/2}}{(a_{CaO})^{3/2}\left(a_{FeO_n}\right)^{5/2}[a_P]}$$

In addition, the activity of tricalcium phosphate is given by:

$$a_{Ca_3(PO_4)_2} = (P)\left(\gamma_{Ca_3(PO_4)_2}\right)$$

And that of iron oxide by Equation 3.14:

$$\left(a_{FeO_n}\right) = \frac{[a_O]}{K_{FeO_n}}$$

And by substituting these expressions into Equation 3.17, we obtain:

Equation 3.18

$$\frac{(P)}{[a_P]} = \frac{K_P}{K_{FeO_n}^{5/2}} \frac{(a_{CaO})^{3/2}[a_O]^{5/2}}{\left(\gamma_{Ca_3(PO_4)_2}\right)^{1/2}}$$

Moreover, by manipulating Equation 3.18, we can write:

Equation 3.19

$$C_{(PO_4^{3-})} = \frac{K_P}{K_{FeO_n}^{5/2}} \frac{(a_{CaO})^{3/2}}{\left(\gamma_{Ca_3(PO_4)_2}\right)^{1/2}}$$

Where $C_{(PO_4^{3-})}$ is known as the phosphate capacity of the slag and depends only on temperature and slag composition. The phosphate distribution between slag and metal phases can then be written as:

Equation 3.20

$$\frac{(P)}{[a_P]} = \frac{(PO_4^{3-})}{[a_P]} = C_{(PO_4^{3-})}[a_O]^{5/2}$$

Furthermore, one can write the phosphate capacity as:

Equation 3.21

$$C'_{(PO_4^{3-})} = K_P \frac{(a_{CaO})^{3/2}}{\left(\gamma_{Ca_3(PO_4)_2}\right)^{1/2}}$$

As a result, the phosphorus distribution is then:

Equation 3.22

$$\frac{(P)}{[a_P]} = \frac{(PO_4^{3-})}{[a_P]} = C'_{(PO_4^{3-})}\left(a_{FeO_n}\right)^{5/2}$$

As well, the relation between the two phosphate capacities can be given as:

Equation 3.23

$$\frac{C'_{(PO_4^{3-})}}{C_{(PO_4^{3-})}} = K_{FeO_n}^{5/2}$$

The phosphate capacities mentioned above, could be found by measuring the equilibrium distribution of phosphorus between slag and metal, at a given oxygen level in the metal for Equation 3.20 or by the activity of iron oxide in the slag for Equation 3.22.

In modern steel industry, the hot metal usually contains low phosphorus levels. As a result, the main components of the slags formed during refining are CaO, SiO_2 and FeO_n with small amounts of P_2O_5 (approx. 1-2%). The phosphate capacity can be calculated from the properties of the slag. Moreover, the phosphorus' equilibria in these types of slags has been widely investigated [34, 35]. In Figure 3.21 [34, 35], the phosphorus distribution lines are given for the CaO-(SiO_2+P_2O_5)-(FeO_n+MnO) system containing 6% MnO and 2%MgO. It can be noted that these lines runs parallel to the lime saturation line. Furthermore, it has been found that CaF_2 and Na_2O additions have a great positive impact on this distribution [36]. On the other side, in phosphorus-rich pig iron (can contain up to 2% P) the slag formed upon refining will be mainly composed of CaO, P_2O_5 and FeO_n. SiO_2 and other oxides are present but to a much lesser degree. As a result, the CaO-P_2O_5-FeO_n system will be the dominant factor in determining the phosphate capacity of these types of slags. The most widely encountered phosphorus-rich pig iron usually contain between 1.6 and 2.2wt%P and 0.3wt% Si. Hence, after dephosphorization, the slag will contain 18-25wt% P_2O_5 and about 4wt% SiO_2. For both

low and high phosphorus hot metal, the main industrial practice is to add as much lime to the slag to achieve either lime or calcium phosphate saturation and to produce a small lime surplus.

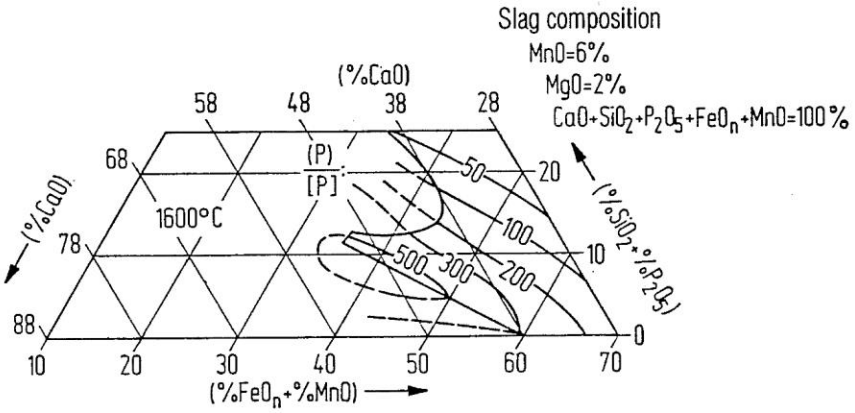

Figure 3.21: Line of equal phosphorus distribution in the system CaO-(SiO_2+P_2O_5)-(FeO_n+MnO). (adapted from [34, 35])

To better understand the CaO- P_2O_5 -FeO_n system, it is beneficial to start with the peripheral CaO- P_2O_5 subsystem. In the lime rich portion, three phases occur: lime, tricalcium phosphate and tetracalcium phosphate. A eutectic exists between the latter two at 1580^0C. When we move from the binary to the ternary system by adding iron oxide, the liquidus lines are transformed to liquidus areas which will fall away toward lower temperatures with increasing FeO_n content (since FeO_n will help in lowering the melting point of the system). In Figure 3.22 [37], the different phases present in the ternary CaO- P_2O_5 -FeO_n system in equilibrium with liquid iron can be seen. In the lime rich region, and at low FeO_n content, the liquidus area of tetracalcium phosphate is dominant. With increasing FeO_n content, the liquidus area transfers into that of calcium oxide. Moreover, at low FeO_n content and higher P_2O_5 contents, the liquidus are of tricalcium phosphate can be seen. With increasing FeO_n content, the aforementioned liquidus area turns into an extended miscibility gap between the iron oxide and tricalcium phosphate.

At the borders of this miscibility gap, two liquid phases exist in equilibrium, with one phase being rich in FeO_n while the other is rich in $3CaO.P_2O_5$. The points C1 and C2 present the upper and lower critical de-mixing limit, respectively. In addition, at high FeO_n and P_2O_5 contents, liquidus area of $3FeO.P_2O_5$ exist. To get a deeper look into this system, an isothermal section at 1600^0C is shown in Figure 3.23 [38]. The line (5, 16) is the saturation isotherm of tetracalcium phosphate, line 1-16 that of lime, and lines (6, 19) and (8, 20) those of tricalcium phosphate. Between points 5 and 6, a FeO_n free melt exist, with the eutectic lying at 1580^0. The (19, 23) and (20, 22) lines outline the miscibility gap. Between the points 22 and 23, solid tricalcium phosphate is in equilibrium with CaO -FeO_n rich melts.

Further investigation of the miscibility gap, shows that the activities of the components in the two coexistent phases, and especially those of FeO_n, are approximately the same. The co-nodes hence present isoactivity lines. As an example, iron oxide rich slags will have high FeO_n activity, which will also be the case in phosphate melts containing low iron oxide in equilibrium with the aforementioned slag. If $CaO-P_2O_5-FeO_n$ system is in in equilibrium with air, the miscibility gap is slightly affected from when the system is in equilibrium with iron [39].

During dephosphorization of high phosphorus pig iron, the resulting slags usually occur in the region delimited by the points (6, 9, 23) and (1, 16, 5), and are usually saturated with lime. In addition, since these slags have high FeO_n activities, they are very effective at dephosphorization. Hence by using these, low iron phosphate slags, significant savings can be made in steel production, by cutting the losses on iron slagging.

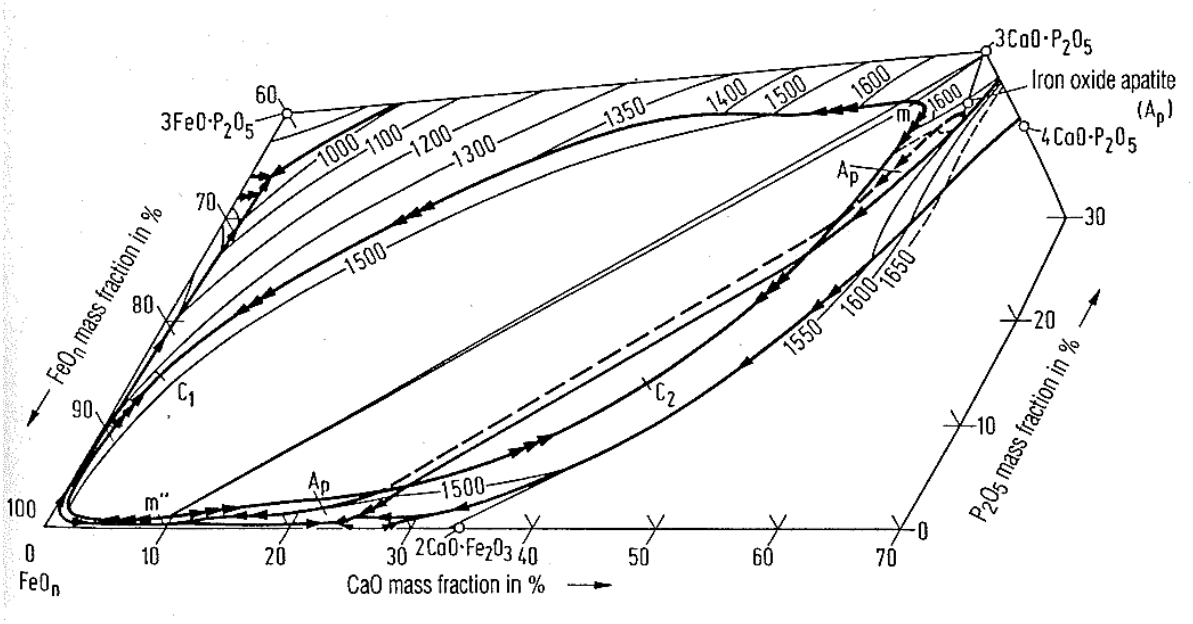

Figure 3.22: A section of the CaO- P_2O_5 -FeO_n constitutional phase diagram, saturated in iron. [37]

As mentioned before, in the lime-rich region of the system, lime saturation line is dominant. This in different from the case of the $CaO-SiO_2-FeO_n$ system, where the dicalcium silicate saturation line dominate the same region. This is because tricalcium phosphate has a much lower melting point than dicalcium phosphate, and as a result, its saturation area cannot penetrate too much into the lime saturation area. This is beneficial for the dephosphorization process, since lime-saturated slags are easy to obtain. If silica is added to the system, the miscibility gap will get narrower and lime saturation line will move toward the lime corner. Moreover, saturation will occur with solid solutions of tri- and di- calcium silicates instead of tricalcium phosphate.

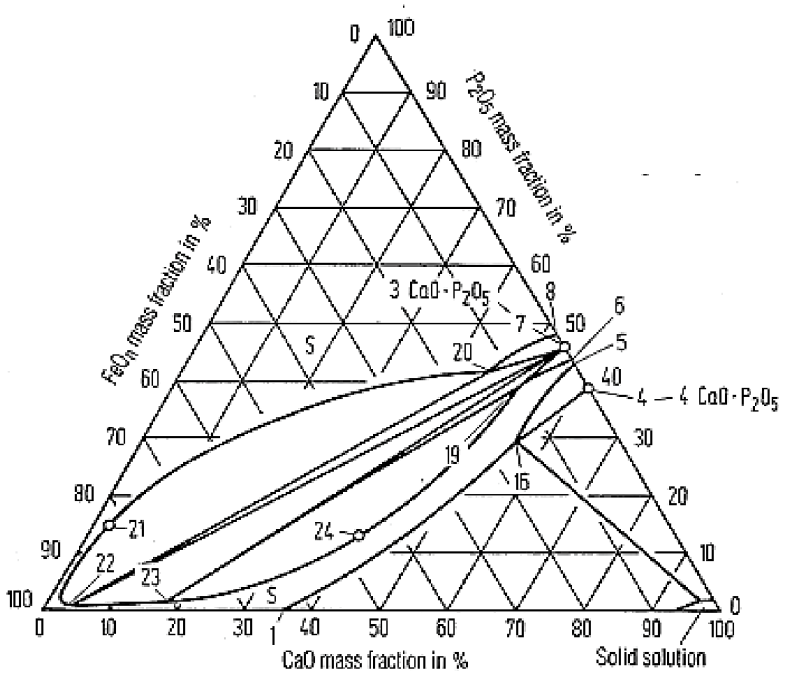

Figure 3.23: Isothermal section of the CaO- P_2O_5 -FeO_n constitutional phase diagram, in equilibrium with iron at 1600 °C. [38]

To achieve significant dephosphorization effect of slags, a prerequisite is a high phosphate activity. This can be achieved by high a_{CaO} according to Equation 3.19, i.e. the slags should be saturated with lime (a_{CaO}=1). Other important factors can be extracted by looking at Equation 3.20 or Equation 3.22. In Equation 3.22, the phosphorus content in the iron melt at $[a_P] = [P].\gamma_{[P]}$, assuming $\gamma_{[P]}$ to be constant, obeys the following relation:

Equation 3.24

$$[P] = \frac{(P)}{C'_{(PO_4^{3-})}\left(a_{FeO_n}\right)^{5/2}}\frac{1}{\gamma_{[P]}}$$

According to the equation above, we can see that the phosphorus content will be determined, in addition to the phosphate capacity, by both iron oxide activity and phosphate content in the slag. Hence, the phosphorus content in the metal is only determined by the slag composition and each of the factors mentioned above have varying potential effects (e.g. the activity of iron oxide is raised the power -5/2).

In Figure 3.24, phosphorus and oxygen contents of iron in equilibrium with lime saturated slags of the CaO- P_2O_5 -FeO_n system are plotted as a function of iron oxide content in the slag (expressed as %Fe) [40, 41, 42, 43, 44]. At wt% Fe >10, the equilibrium values of both oxygen

and phosphorus are approximately constant. This is due to the constancy of both iron oxide activity and that of calcium phosphate. The phosphorus content lie between 0.010 and 0.005wt%, and lower levels can be reached if P_2O_5 content of the slag are less than 1% [35]. This has important applications in secondary dephosphorization processes. The aforementioned process is used when extremely low-levels of phosphorus are required and is achieved by the use of CaO -FeO_n with the possibility of adding CaF_2.

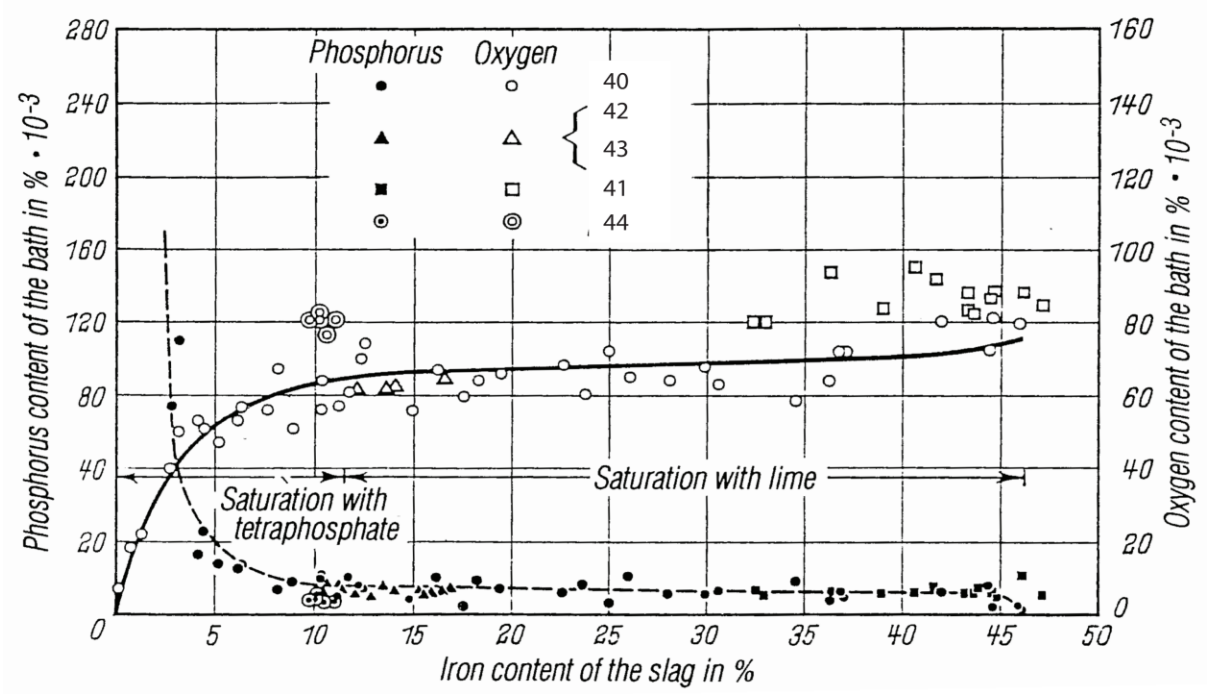

Figure 3.24: Oxygen and phosphorus contents in iron melts saturated with tetracalcium phosphates and lime slags of the CaO- P_2O_5 -FeO_n system at 1600 °C. (adapted from [40, 41, 42, 43, 44])

Figure 3.25 [36] shows the phosphorus distribution under different slags obtained from equilibrium measurements plotted against iron oxide contents in these slags. The CaO-SiO_2-FeO_n and CaO-Al_2O_3-FeO_n systems show similar pattern, and their phosphate capacities coincide. However, the CaO- CaF_2-FeO_n system exhibits a much higher phosphate capacities and as a result lower phosphorus levels can be achieved by using this type of slag. For example, the phosphorus distribution is equal to one at 20% FeO_n in the CaO- CaF_2-FeO_n. This translates to a phosphorus content in the metal [P] =$5.6*10^{-4}$ wt% at 1wt% P_2O_5 content in the slag.

The positive effect of CaF_2 additions on the dephosphorization process is related to the fact that it increases the activity of FeO_n while at the same time reducing that of P_2O_5 [45].

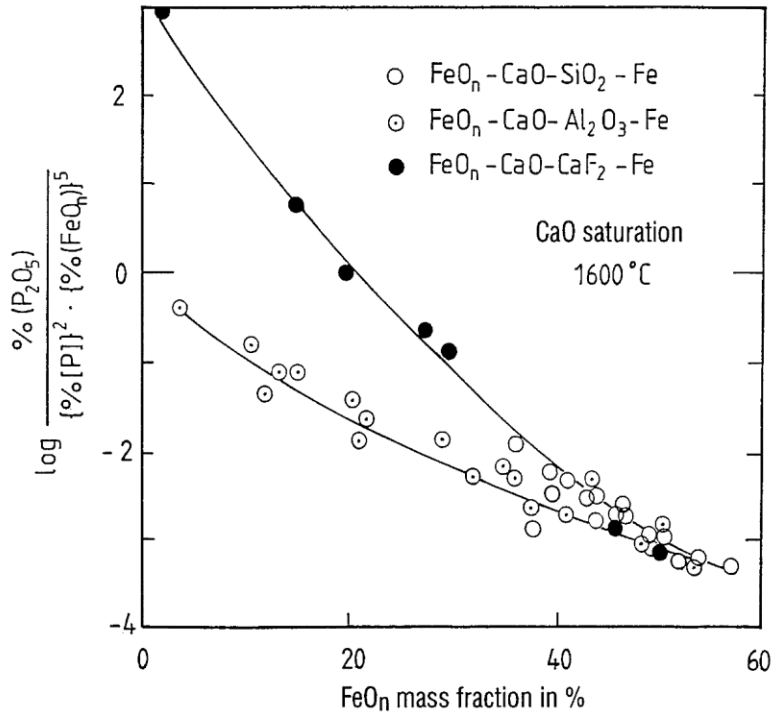

Figure 3.25: Equilibrium ratio as a function of the iron oxide content in different types of slags. [36]

3.5 The total mass transfer coefficient

This section and the following subsections (3.5.1, 3.5.2) are based on the work of T. Abel Engh in Principles of Metal Refining [46]. In the interface between the metal and the slag, a resistance to flow exist in the "films" on both sides. These two resistance could be combined into a total resistance, k_t. By taking on the electric circuit theory, the two resistances given as the inverse of the mass transfer coefficients, $(1/k)$ and $(1/k_{slag})$, can be easily combined. However, since the driving forces (voltages) used in the rate equations for the two phases have different units, a more complicated procedure should be followed.

In the metal phase, the molar flux of an impurity x, can be written as:

Equation 3.25

$$\dot{n} = \frac{k\rho}{100M_x}([\%x] - [\%x]_i) \ \ [kmol/(m^2 s)]$$

Where $\dot{n}$ is the molar flux, k mass transfer coefficient in the melts, ρ the density and M_x the molar weight of species x. Since the process is carried out at high temperatures, high reaction rates are expected hence the metal and slag concentration at the interface, $(\%x)_i$ and $[\%x]_i$respectively, can be assumed to be at equilibrium:

Equation 3.26

$$K = \frac{(\%x)_i \gamma_x}{[\%x]_i f_x}$$

We can rewrite Equation 3.25 to give us the driving force, expressed as:

Equation 3.27

$$[\%x] - [\%x]_i = \frac{\dot{n} 100 M_x}{k\rho}$$

Same approach can be applied to the slag phase, giving:

Equation 3.28

$$\dot{n} = \frac{k_{slag}\rho_{slag}}{100 M_x}\left((\%x)_i - (\%x)\right)$$

It follows also for the driving force:

Equation 3.29

$$(\%x)_i - (\%x) = \frac{\dot{n} 100 M_x}{k_{slag}\rho_{slag}}$$

The difference between the driving force in the metal and in the slag is the units, where the first is given by mass percent metal and the second mass percent slag. However, by using the partition coefficient,

Equation 3.30

$$\frac{f_x K}{\gamma_x} = \frac{(\%x)_i}{[\%x]_i}$$

Equation 3.29 becomes:

Equation 3.31

$$[\%x]_i - \frac{(\%x)\gamma_x}{K f_x} = \frac{\dot{n} 100 M_x \gamma_x}{k_{slag}\rho_{slag} K f_x}$$

The molar flux can be written now as the sum of the driving force in the metal and slag phase. So by adding Equation 3.27 and Equation 3.31 we obtain:

Equation 3.32

$$[\%x] - \frac{(\%x)\gamma_x}{Kf_x} = \dot{n}100M_x\left(\frac{1}{\rho k} + \frac{\gamma_x}{k_{slag}\rho_{slag}Kf_x}\right)$$

In the end, by defining a total resistance equal to the sum of both the resistance in the metal and in the slag Equation 3.32 becomes:

Equation 3.33

$$\dot{n} = \frac{\rho k_t}{100M_x}\left([\%x] - \frac{(\%x)\gamma_x}{Kf_x}\right)$$

It can be noted that $(\%x)\gamma_x/Kf_x$ is the hypothetical equilibrium concentration in the metal and slag phase. The concentration profiles can be seen in Figure 3.26. The final equation has a very important role in modeling refining processes.

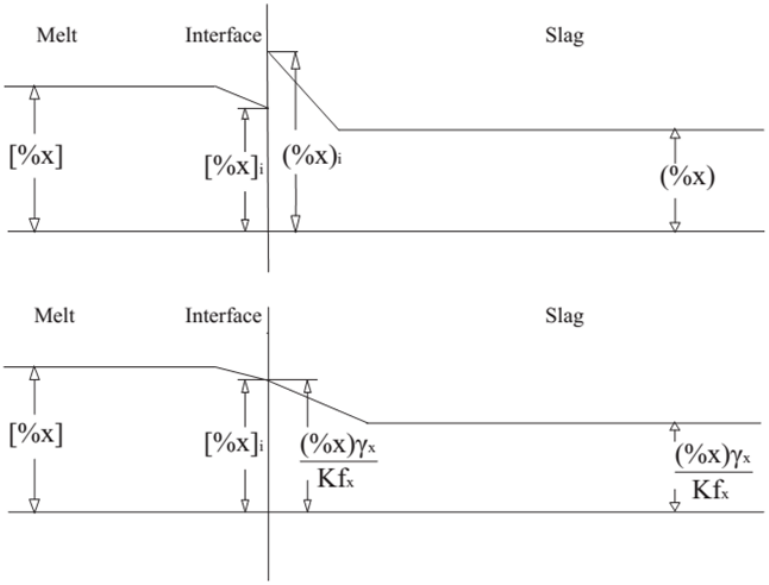

Figure 3.26: Concentration profiles in the melt and the slag[46]

3.5.1 Continuous back mix reactor

Although continuous reactors are simpler than batch reactor, they are not widely employed on industrial scale. The main use of this technology is in aluminum cast houses where gas purging is carried out.

To simplify the process, a good approximation will be to assume complete mixing in the melt. Figure 3.27 shows that the concentration of the impurity, x, changes discontinuously from $[\%x]_{in}$ when entering the reactor to a constant value $[\%x]$ throughout the melt. Hence, the mass balance for x can be written as:

x (kmols/second), flowing into the reactor = x (kmols/second) flowing out from the reactor

+ x removed from the melt per unit time

Or

Equation 3.34

$$\frac{\dot{M}[\%x]_{in}}{100M_x} = \frac{\dot{M}[\%x]}{100M_x} + \dot{G}_x$$

Where $\dot{M}$ is the flow of the metal into the reactor in kg/s and $\dot{G}_x$ is the removal rate of impurity x by different mechanisms, for example by gas purging.

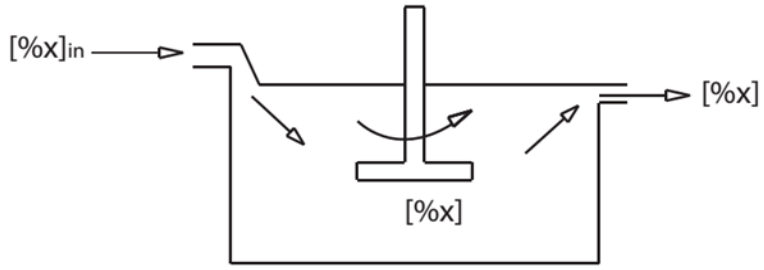

Figure 3.27: Mixing reactor [46]

Assuming that impurities are removed partly by evaporation from the top surface of the melt and partly as gas in the bubbles (given by the gas law, $\dot{G} = p_x^0/p_{inert}$), we can write the following equation:

Equation 3.35

$$\dot{G}_x = \frac{\dot{G}Kf_x[\%x]Z}{p_{inert}} + \frac{k_{ts}A_s\rho[\%x]}{100M_x}$$

k_{ts} *total mass transfer coefficent*

$$A_s \textit{ is the melt top surface area}$$

$$Z \textit{ is the efficency of removal technique}$$

It can be noted that both terms in Equation 3.35 of $\dot{G}_x$ are proportional to $[\%x]$. Hence, we can calculate the reduction ratio $[\%x]/[\%x]_{in}$ for the process. By combining Equation 3.34 and Equation 3.35, we obtain:

Equation 3.36

$$\frac{[\%x]}{[\%x]_{in}} = \left(1 + \frac{\dot{G}Kf_x Z100M_x}{p_{inert}\dot{M}} + \frac{k_{ts}A_s\rho}{\dot{M}}\right)^{-1}$$

If the impurity has a low vapor pressure, the term expressing the removal as gas in the bubbles is negligible compared to that of the removal from the top surface of the melt. In this case, the role of gas purging is to stir the melt and hence give a higher value of the mass transfer coefficient, k_{ts}. Moreover, it can be noted that a higher metal flow $\dot{M}$, leads to a less favorable reduction.

Usually in industrial practices, many reactors are coupled in series to give a better reduction ratio. This can be explained by the fact that instead of reducing the impurity content in one single step from $[\%x]_{in}$ to $[\%x]$, and by this losing the driving force for refining , a different approach is employed. In this case, the concentration is reduced in successive steps: from $[\%x]_{in}$to $[\%x]_1$, from $[\%x]_{N-1}$ to $[\%x]_N$ and finaly from $[\%x]_n$ to $[\%x]$, where N is the number of reactors. In addition, the flow of inert gas $\dot{G}$ will be distributed to N reactors and the contact area will be A_s/N in each reactor. Equation becomes:

Equation 3.37

$$\frac{[\%x]}{[\%x]_{in}} = \left(1 + \frac{a\dot{G}}{N\dot{M}} + \frac{bA_s}{N\dot{M}}\right)^{-N}$$

In this case, $[\%x]$ is the output after passing through N^{th} unit and

Equation 3.38

$$a = \frac{Kf_x Z100M_x}{p_{inert}} \;, b = k_{ts}\rho$$

Finally, assuming N increases to infinity, we can use the following mathematical approximation:

Equation 3.39

$$\left(1+\frac{a\dot{G}}{N\dot{M}}+\frac{bA_s}{N\dot{M}}\right)^{-N} \rightarrow exp\left(-\frac{a\dot{G}}{\dot{M}}-\frac{bA_s}{\dot{M}}\right)$$

The main application of this approach is when reduction ratios $[\%x]/[\%x]_{in}$ of less than $^1/_4$ are required. Systems with $N \rightarrow \infty$ reactors will give much better performance than a single back-mix reactor, which can be seen in Figure 3.28. In addition, the large number of reactors will give the same residence time for all elements of the fluid:

$$\tau = \frac{M}{\dot{M}}$$

where M is the total melt mass across all N reactors.

As mentioned before, the main use of this process is in aluminum refining. Three reactors are used to obtain low $[\%x]/[\%x]_{in}$ ratios and to ensure an equivalent approach to the "constant residence time continuous reactor".

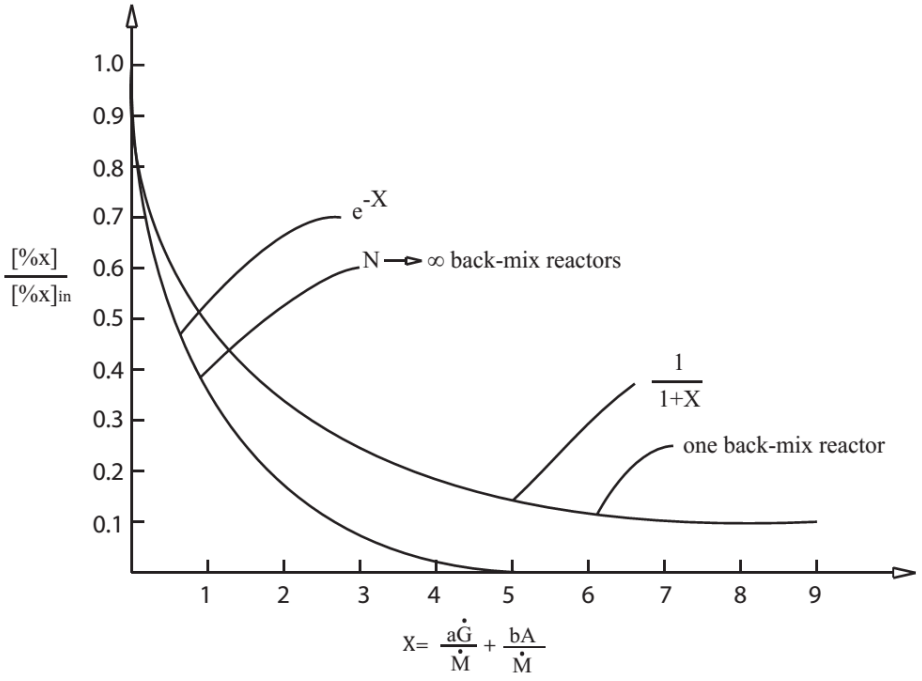

Figure 3.28: $[\%x]/[\%x]_{in}$ ratio versus X [46]

3.5.2 Batch reactors

The most commonly used reactors for metal refining are the batch reactors. In steelmaking, all industrial units handles batches of metal. The mass balances is given by:

Reduction of impurity, x (kmols/second), contained in the melt per unit time =

impurity, x (kmols/second), transferred from melt per unit time

Equivalent to:

Equation 3.40

$$-\frac{M}{100M_x}\frac{d[\%x]}{dt} = \dot{G}_x$$

The removal rate of x, $\dot{G}_x$, can be written as:

Equation 3.41

$$\dot{G}_x = \left(a\dot{G} + bA_s\right)\frac{[\%x]}{(100M_x)}$$

Hence, Equation 3.40 becomes:

Equation 3.42

$$\frac{d[\%x]}{[\%x]} = -\left(a\dot{G} + bA_s\right)\frac{dt}{M}$$

Then carrying the integration, taking $[\%x] = [\%x]_i$ at time $t = 0$ to $[\%x]$ at time t

Equation 3.43

$$\int_{[\%x]_i}^{[\%x]} \frac{d[\%x]}{[\%x]} = -\int_0^t \left(a\dot{G} + bA_s\right)\frac{dt}{M}$$

Then if we assume constant operating conditions, i.e. $\left(a\dot{G} + bA_s\right)$ is independent of time, the integration gives us:

Equation 3.44

$$ln\frac{[\%x]}{[\%x]_i} = -\left(a\dot{G} + bA_s\right)\frac{t}{M}$$

Or

Equation 3.45

$$\frac{[\%x]}{[\%x]_i} = exp\left\{\frac{-(a\dot{G} + bA_s)t}{M}\right\}$$

It can be noted that the reduction rate drops exponentially with time. By replacing, t in Equation 3.45 by $\tau = M/\dot{M}$, we obtain Equation 3.39. Hence, it can be noted that by using a batch reactor, one could obtain the best achievable results from a back-mix reactor. However, the problem with batch process are that they are difficult to control due to their time dependence, and are very labor consuming.

3.5.3 Slag metal refining in the ladle (batch reactor)

The main problem that accompanies the use of slag in the refining of metals is mixing in the slag phase. The relatively high viscosity of slags leads to an uneven distribution of the impurity in this phase. For this part, we also assume "complete mixing" in the slag phase. Equation 3.40 thus becomes:

Equation 3.46

$$-M\frac{d[\%x]}{dt} = k_t \rho A_s([\%x] - [\%x]_e)$$

Where $[\%x]_e$ is the hypothetical concentration in the metal in equilibrium with the actual concentration in the slag $(\%x)$, given as:

Equation 3.47

$$[\%x]_e K f_x = \gamma_x (\%x)$$

To be able to integrate Equation 3.46, $[\%x]_e$ must be replaced by a function of$[\%x]$. This operation can be carried out by noting that the impurities leaving the melt will enter the slag, given by:

Equation 3.48

$$M([\%x]_{in} - [\%x]) = M_s(\%x)$$

Where M_s is the slag mass. Assuming that the slag did not contain any impurities at the start of refining, Equation 3.47 and Equation 3.48 can be combined to give:

Equation 3.49

$$[\%x]_e = \frac{\gamma_x}{Kf_x}\frac{M}{M_s}([\%x]_{in} - [\%x])$$

Hence, the driving force in Equation 3.46 becomes:

Equation 3.50

$$[\%x] - [\%x]_e = [\%x]\left(1 + \frac{\gamma_x M}{Kf_x M_s}\right) - \frac{\gamma_x M}{Kf_x M_s}[\%x]_{in}$$

The lowest value of $[\%x]$ is attained when the driving force reaches zero. This is expressed by:

Equation 3.51

$$[\%x] = [\%x]_\infty = \frac{M[\%x]_{in}}{M + Kf_x M_s/\gamma_x}$$

It can be noted that $[\%x]_\infty$ is the value of $[\%x]$ when the thermodynamic equilibrium between the melt and the slag is finally reached (when $t \to \infty$). The driving force can be written as a function of $[\%x]_\infty$:

Equation 3.52

$$[\%x] - [\%x]_e = \left(1 + \frac{\gamma_x M}{Kf_x M_s}\right)([\%x] - [\%x]_\infty)$$

Introducing Equation 3.52 into Equation 3.46 yields:

Equation 3.53

$$\int_{[\%x]_{in}}^{[\%x]} \frac{d[\%x]}{[\%x] - [\%x]_\infty} = -\int_0^t \frac{k_t \rho A_s}{M}\left(1 + \frac{\gamma_x M}{Kf_x M_s}\right)dt$$

Upon integrating and assuming k_t, γ_x, f_x do not change with time, we obtain:

Equation 3.54

$$\frac{[\%x] - [\%x]_\infty}{[\%x]_{in} - [\%x]_\infty} = exp\left\{-\frac{k_t \rho A_s}{M}\left(1 + \frac{\gamma_x M}{Kf_x M_s}\right)t\right\}$$

We can see from Figure 3.29 that $[\%x]$ drops exponentially until it reaches $[\%x]_\infty$ given by the equilibrium between x in the two phases, metal and slag. At $t = \tau$, we have the following:

Equation 3.55

$$t = \tau = \frac{M}{k_t \rho A_s \left(1 + \frac{\gamma_x M}{K f_x M_s}\right)}$$

The difference between $[\%x]$ and the final value $[\%x]_\infty$ is reduced to $1/e = 0.37$ of the difference at time $t = 0$. It can also be seen that τ is inversely proportional to the total mass transfer coefficient, k_t. Hence, a bigger mass transfer coefficient leads to a faster refining process.

However, it is important to note that this approach is only applicable if we have complete mixing in the slag phase. If mixing is incomplete, $[\%x]$ will then remain higher than that given by Equation 3.54.

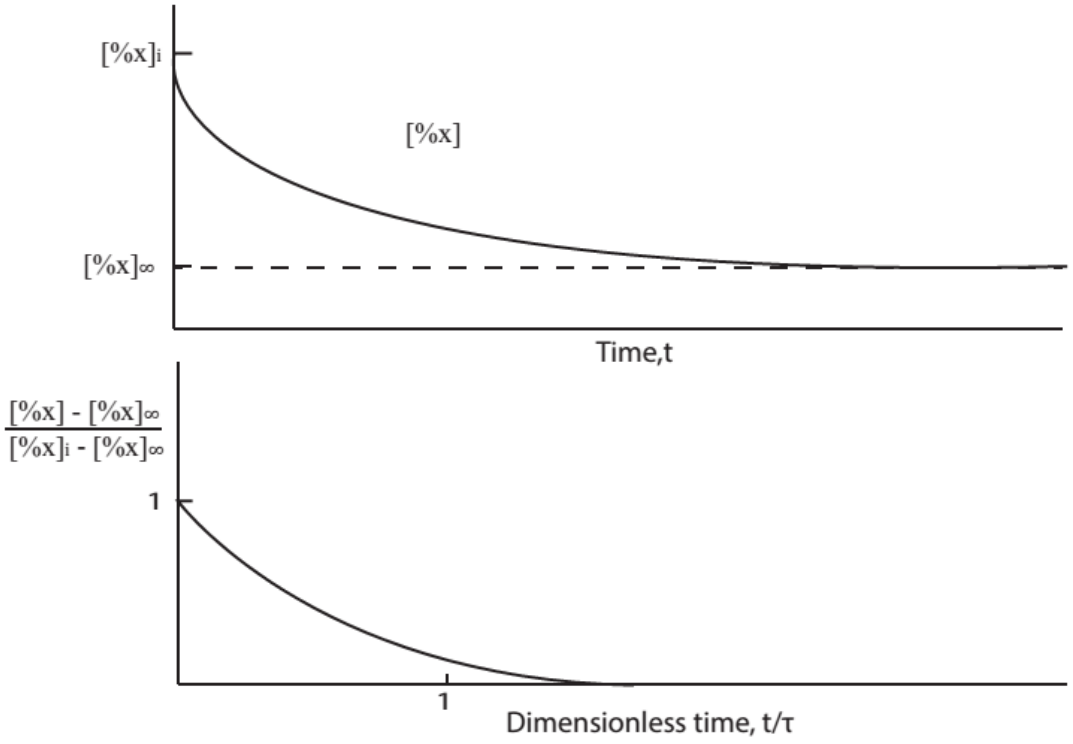

Figure 3.29: Exponantial drop of the concetration in the melt $[\%x]$ versus time [46]

4 Experimental

4.1 Materials

4.1.1 Crucible materials

Three types of crucible were used through the master thesis work:

1. Alumina (Al_2O_3) crucibles: These crucibles were used to alloy the iron with phosphorus, by mixing iron and iron phosphide in predetermined quantities.
2. Magnesia (MgO) crucibles: Dephosphorization experiments were carried in this type of crucibles.
3. Graphite crucible: It acted as an additional safety measure, where the magnesia crucibles where placed inside of it. In case the magnesia crucible cracked or spillage, the molten slag and metal will be contained in the graphite crucible and damage to the furnace will be prevented.

The use of basic oxides in the slag requires a suitable crucible material. It is generally known that a crucible made from acidic oxide cannot be used in this case; hence, neither silica (SiO_2) nor alumina crucibles were used. As a result, two possible choices of materials were investigated: magnesia or platinum (Pt). However, the presence of molten iron (Fe) will lead to the corrosion of the Pt crucible due to the alloying of Fe and Pt. As a result, MgO was the suitable crucible to carry out the refining experiments.

MgO crucibles show limited solubility in basic slags, have good mechanical strength and high temperature stability, are widely available and are relatively cheap. The crucibles were purchased from Aremco, a USA based company. They are flat-bottomed cylindrical crucibles with the following dimensions (38.10mm OD X 50.80mm L X 3.81mm T).

The graphite and alumina crucibles were available at NTNU and were provided by the department of materials science and engineering.

4.1.2 Iron

Two types of iron were used through the master thesis work:

1. Pure electrolytic iron: It had 99.99% purity and was in the form of iron granules. This was used to smelt a pure Fe-P alloy.
2. Iron from Tizir, Tyssedal: It is Fe-800 quality and it was in the form of small iron discs weighing each ≈50g. The average chemical composition of this type of iron is given in Table 4.1, the balance being Iron. This iron was used to smelt a second Fe-P alloy of lower purity, to try to simulate industrial conditions, where dephosphorization will be carried on this specific iron quality.

Table 4.1: Chemical composition of Tizir iron, 800 quality

Element	C	Si	S	P	Mn	Ni	Cr	Mo	V	Cu	Ti
Mass %	3.89	0.14	0.01	0.03	0.02	0.04	0.03	0.00	0.02	0.00	0.01
Std. Dev.	0.003	0.002	0.001	0.000	0.000	0.000	0.000	0.000	0.000	0.000	0.000

4.1.3 Iron phosphide

Two types of iron-phosphide were also used through the master thesis work:

1. Pure iron-phosphide (Fe_3P): It was bought from Sigma-Aldrich as a fine powder and has 99.5% purity. It was used to smelt the Fe-P of high purity.

Industrial grade iron-phosphide: It is in the form of small lumps (10*50mm) and was used to smelt another, less pure, Fe-P alloy. The chemical analysis of this iron phosphide is given in Table 4.2, the balance being Iron. The analysis was carried out by William Rowland Limited.

Table 4.2: Industrial iron-phosphide chemical composition

Element	P	Mn	Ti	Si	C
Mass %	25.06	2.98	1.38	0.5	0.041

4.1.4 Oxides

Three types were used through the master thesis work:

1. Iron oxide (Fe_2O_3): It was bought from Sigma-Aldrich as a fine powder of 99% purity.
2. Silicon dioxide or silica (SiO_2): It was available at NTNU as a fine powder of 99% purity and was provided by the department of materials science and engineering.

3. Calcium oxide or lime (CaO): It was also available at NTNU as a fine powder of 99% purity and was provided by the department of materials science and engineering.

These oxides were used in order to obtain slags with different compositions. The slags were prepared individually for each experiment, by mixing predetermined quantities of each oxide. No pre-melting was carried out and the slags were melted simultaneously with the iron.

4.2 Experiments

4.2.1 Iron-Phosphorus alloys

Two different iron phosphorus alloys were smelted:

1. **Alloy A**: To eliminate the effect of impurities on the dephosphorization process, an "impurity-free" Iron-Phosphorus alloy was smelted. For this purpose, 850g of pure electrolytic iron granules were alloyed with 15.5g of iron phosphide (99.5%pure), which will theoretically lead to a relatively pure alloy containing about 0.3wt% P. This process was carried out in an alumina crucible under argon atmosphere and once the mixture was molten it was cast in a copper mold and left to cool down. However, phosphorus segregation in the alloy was observed and hence a re-melting was carried out in a graphite tube resistance furnace. The re-melting lead to a better phosphorus distribution across the alloy.

2. **Alloy B**: To simulate the conditions in the industrial process, another iron-phosphorus alloy was smelted. For this purpose, 420g of 800-quality iron were alloyed with 5.2g of industrial grade iron-phosphide. This process was carried out in an alumina crucible but this time in a graphite tube resistance furnace under argon atmosphere. The melt was allowed to solidify and was re-melted a couple of times. The exact cycle is available in the appendix. This one carried out to ensure proper phosphorus distribution in the alloy.

4.2.2 Refining experiments

All refining experiments were done in a graphite tube resistance furnace under argon atmosphere. The specific furnace is called the Resina furnace (Figure 4.1). The oxides were mixed together to give the desired initial composition and then added to the crucible. Moreover the Fe_2O_3 amount added was calculated based on the fact that it will react with the iron melt to give FeO, which is referred to as FeO_X. The iron was placed on top of the oxides mix. The experimental setup is shown in Figure 4.2. The temperature measurement in these experiments is done by a thermocouple at $T<1300^0C$ and by a spectro-pyrometer at $T\geq1300^0C$ and both of them measure the temperature of the heating element and not that of the sample.

Figure 4.1: The Resina furnace

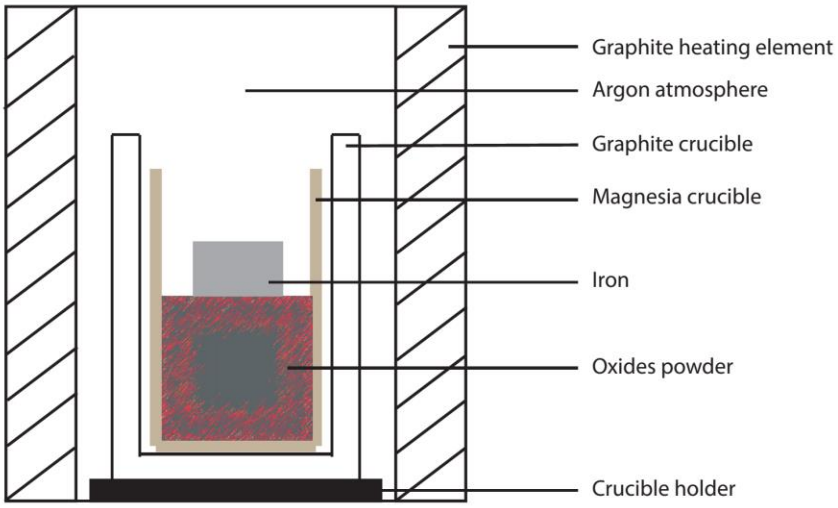

Figure 4.2: Experimental setup used in Set A and B of experiments

It can be noted that the MgO crucible is placed in a bigger graphite crucible for added safety in the case of thermal or mechanical failure of the MgO crucible. In this case, the melt will be contained in the graphite crucible and damage to the furnace will be avoided. Fortunately, not a single accident occurred during this work. In total, twelve experiments were carried out. These can be divided into two sets:

1. **Set A**: It consisted of nine experiments. In these experiments, 60-65g of Alloy A were used. The experimental protocol consisted of three steps. First, the temperature was increased to 1600^0C during the first hour. Once this temperature was reached, it was maintained during 30minutes, and this period is considered as the refining time. Lastly, the heating was stopped and argon purging was performed for 1 hour in order to cool down the sample and prevent oxidation of the melt. The main variable in these experiments was slag composition. The specific composition in each experiment can be found in Table 4.3. It is worth noting that duplicates were carried out for three of the slags composition to test for reproducibility. Upon chemical analysis, duplicates showed the same results, hence reproducibility was validated and further compositions were tested only once. Moreover, experiment 1 was considered as a test run to study if the metal-slag ratio used w suitable for further experiments. The main reason why these compositions were used was to study the effect of iron oxide and calcium oxide on the dephosphorization and how silica additions could affect the system.

Table 4.3: Slag composition in first set of experiments (Set A)

Experiment	metal-slag ratio	Slag composition (mass%)		
		% FeO_X	% CaO	% SiO_2
1	**5:1**	**100.0**	**0.0**	**0.0**
2	**2.5:1**	**82.7**	**17.3**	**0.0**
3	**2.5:1**	**82.7**	**17.3**	**0.0**
4	**2.5:1**	**74.5**	**25.5**	**0.0**
5	**2.5:1**	**74.4**	**25.6**	**0.0**
6	**2.5:1**	**65.6**	**34.4**	**0.0**
7	**2.5:1**	**65.6**	**34.4**	**0.0**
8	**2.5:1**	**50.2**	**30.6**	**19.2**
9	**2.5:1**	**50.4**	**44.7**	**4.9**

2. **Set B:** In these experiments, 60-65g of Alloy B were used. The same experimental protocol as the one mentioned above was followed with some changes to the refining temperature and the refining time. These changes are stated in Table 4.4.
   The slag composition was the same across the three experiments in this set (50% FeO_X, 45 %CaO and 5% SiO_2, given as mass %). In addition, the metal-slag ratio is 2.5:1.

Table 4.4: Experimental conditions in second set of experiments (Set B)

Experiment number	Temperature(^{0}C)	Refining time (min)
10	**1600**	**30**
11	**1500**	**30**
12	**1600**	**15**

4.3 Analysis tests

Analytical tests were performed on both the iron and the slag and as a result will be divided into two categories.

1. **Iron analysis tests:** These tests were carried out to obtain the chemical composition of the metal. Two methods were used: LECO CS600 for carbon and sulfur. Spark analysis for the rest of the elements done on Thermo ARL 3460/Metal analyzer. In addition, these tests were carried out at TiZir Titanium and Iron AS.

2. **Slag analysis tests:** X-Ray Diffraction (XRD) were used to characterize the slag phase and the analysis was carried out at the department of materials science and engineering, NTNU. The equipment used was Bruker DAVINCI D8 and the database PDF -4+ 2013 RDB. The slags from the experiments were crushed and XRD was carried out to determine the different crystal structures present in the slag and hence the possible species/oxides in it.

Moreover, Electro Probe Micro Analysis (EPMA) was also carried on Set B of experiments, since the obtained results were complex and need further investigation. This included structure investigation, quantitative point analysis and quantitative mapping. These tests were carried out using the Jeol JXA-8500F Electron probe microanalyzer at the department of materials

science and engineering, NTNU. Table 4.5 shows the different tests carried out on the different samples.

Table 4.5: Analysis tests performed on the different samples (+=done, /= not done)

Experiment		Analytical tests				
		Spark/Leco	XRD	EPMA		
				Structure	Point analysis	Mapping
Alloy	A	+	/	/	/	/
	B	+	/	/	/	/
Set A	1	+	+	/	/	/
	2	+	+	/	/	/
	3	+	+	/	/	/
	4	+	+	/	/	/
	5	+	+	/	/	/
	6	+	+	/	/	/
	7	+	+	/	/	/
	8	+	+	/	/	/
	9	+	+	/	/	/
Set B	10	/	+	+	+	+
	11	+	/	+	+	/
	12	/	+	+	+	+

5 Results

5.1 Iron alloys

5.1.1 Alloy A

As was mentioned before, phosphorus segregation was observed after the primary melting. The chemical composition was measured at two points one at the top and bottom of the alloy (Table 5.1).

Table 5.1: Initial Chemical composition of Alloy A

Element		C	Si	S	P	Mn	Ni	Cr	Mo	V	Cu	Ti
Mass %	Top	0.32	<0.01	<0.001	0.83	0.001	0.007	0.004	0.005	<0.01	0.016	<0.01
	Bot	0.29	<0.01	<0.001	0.06	0.001	0.007	0.005	0.005	<0.01	0.016	<0.01

A re-melt was done and analysis were carried out on Alloy A. Nine different points in the alloy were analyzed and the average composition is given in Table 5.2. A more detailed analysis of all the different point is given in the appendix. It can be seen that phosphorus addition was successful (wt% P=0.28) and the alloy was more homogenous.

Table 5.2:Final Chemical composition of Alloy A (After the re-melting)

Element	C	Si	S	P	Mn	Ni	Cr	Mo	V	Cu	Ti
Mass% -	0.330	<0.001	0.005	0.285	<0.001	0.004	0.002	0.002	<0.001	0.004	<0.001
Std. Dev.	0.000	0.000	0.001	0.041	0.000	0.000	0.000	0.000	0.000	0.001	0.000

5.1.2 Alloy B

To prevent the problem of phosphorus segregation this alloy went through couple of re-melting steps as was mentioned in the experimental part. However, phosphorus segregation was still observed and is expressed by the relatively large standard deviation. Five different points in the alloy were analyzed and the average composition is given in Table 5.3. A more detailed analysis of all the different point is given in the appendix. No further re-melting was done to improve the distribution.

Table 5.3: Chemical composition of Alloy B

Element	C	Si	S	P	Mn	Ni	Cr	Mo	V	Cu	Ti
Mass %	3.99	0.13	0.01	0.05	0.01	0.03	0.02	<0,001	0.02	0.00	0.01
Std. Dev.	0.030	0.006	0.000	0.018	0.001	0.001	0.003	0.000	0.005	0.001	0.003

5.2 Refining experiments

5.2.1 Temperature measurements

We can see from Figure 5.1, the heating curves for the different experiments are quite similar and consistent where the desired refining temperature is reached with one hour after the heating starts. It is then kept at that temperature for the predetermined refining time and later left to cool. Experiment 11 and 12 show the only noticeable difference since in the former the refining temperature was changed 1500^0C whereas in the latter the refining time was changed to 15minutes. One important point to note is that when the refining period was done, the heating element was turned off and the chamber was purged with argon.

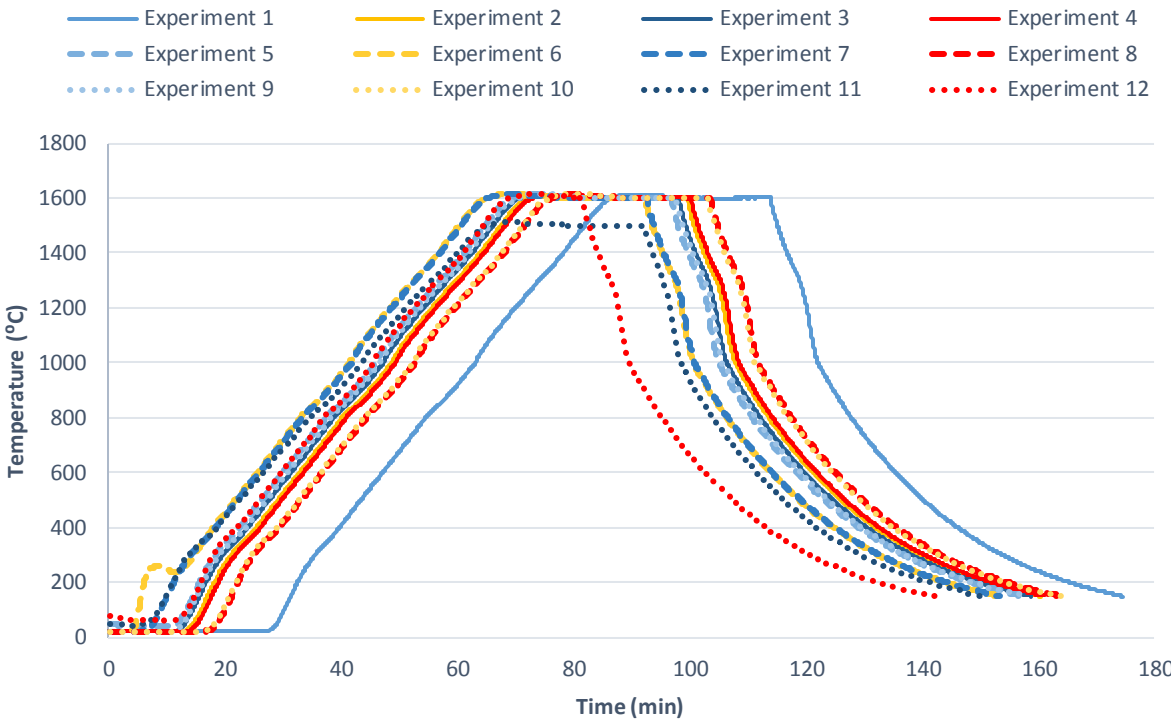

Figure 5.1: Temperature curves for all the refining experiments

5.2.2 Physical appearance

In this section, the physical appearance of the experiments in Set A and Set B will be presented. It consists of different pictures taken after the refining process. A description of the most important features will be also given.

1. Set A

Figure 5.3 shows the appearance of the different samples in set A. it is worth noting that the inner diameter of the crucibles (white color) is 3cm. These experiments have similar appearance where the metal (silver color) and slag phase (dark gray color) form two separate layers and the duplicates looks more or less the same. In addition, it can be seen from experiment 1 that the volume of the slag was not sufficient to cover the whole surface of the metal. As a result, the metal-slag ratio was changed from (5:1) to (2.5:1). Moreover, the color of the slag sifted toward lighter shades of grey with increasing lime and silica contents. It can also be seen that the slag wetted the crucible pretty well.

Upon further inspection of the samples, it was observed that in experiments 1-7, the slag was tightly bound to the metal, and as a result, slag was difficult to remove from the surface from the metal. On the other hand, in experiments 8 and 9, the slag could be easily removed from the metal since it formed a glassy like phase. The surface of the metal and slag in experiment 8 can be seen in Figure 5.2. The grove on the metal surface is the result of the saw blade hitting it while trying to remove parts of the crucible.

In addition, the total mass of the crucible, metal and slag was measured before and after the refining process and mass loss was negligible.

Slag surface **Metal surface**

Figure 5.2: Pictures showing the slag and metal surfaces in Experiment 8

Figure 5.3: Pictures showing the physical appearance of the samples in Set A

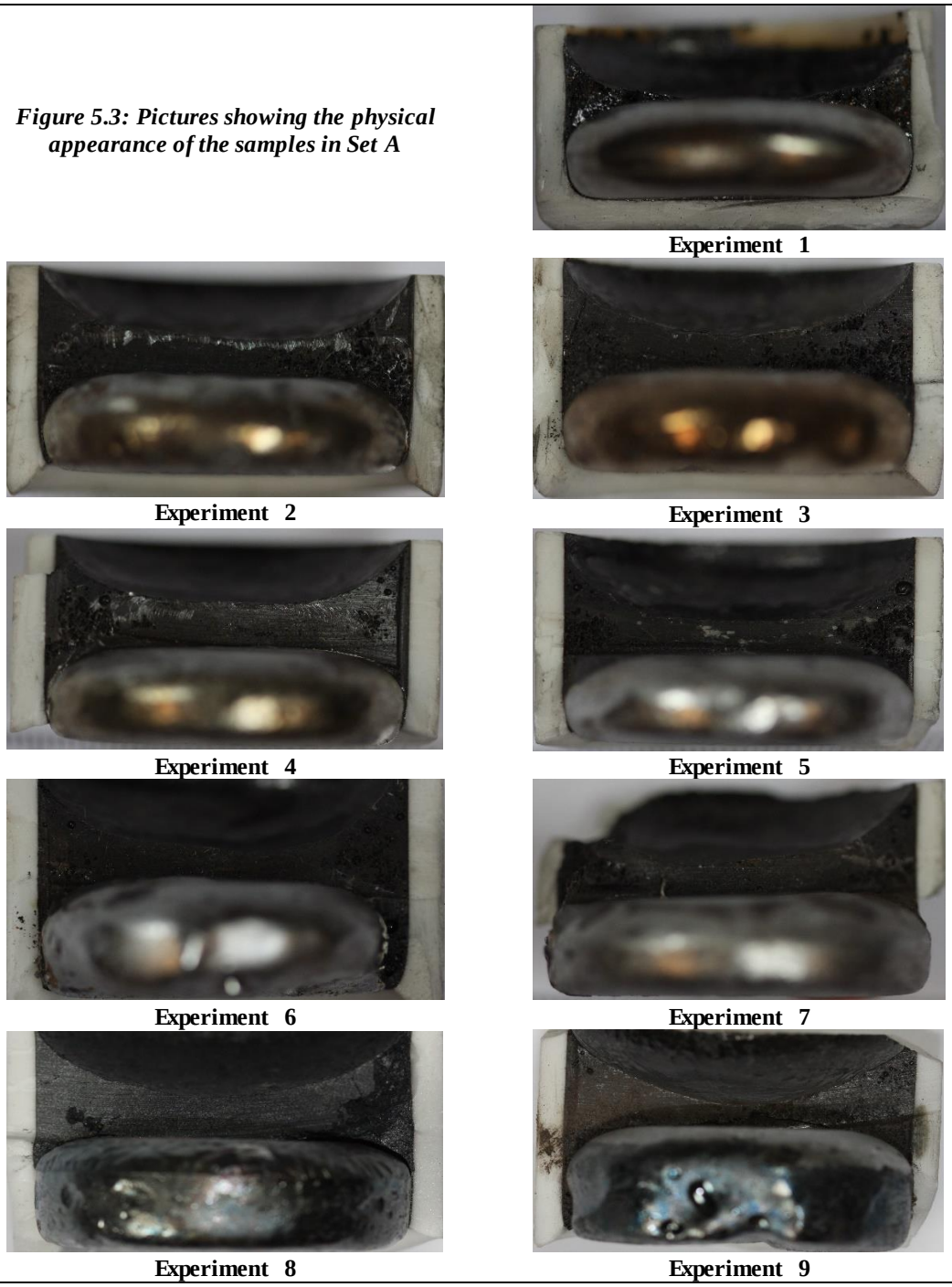

Experiment 1

Experiment 2

Experiment 3

Experiment 4

Experiment 5

Experiment 6

Experiment 7

Experiment 8

Experiment 9

2. Set B

In experiments 10-12, the appearance of the samples differs greatly from the one observed in Set A. the main difference is that the metal and slag were intermixed and formed some sort of

emulsification and it was impossible to separate the metal from the slag. In addition, small iron droplets were observed on the walls of the crucible (Figure 5.4). However, after being left for a couple of days in air, the slag disintegrated in experiments 10 and 12, changing its color from dark grey to brownish and at this stage it was easily removed from the metal (Figure 5.5). For experiment 11, the sample kept its shape however at later stages, part of the slag started to be brownish. Detailed images of the different samples can be found in the appendix.

In addition, the total mass of the crucible, metal and slag was measured before and after the refining process. However in this set of experiments, mass loss was significant (≈2.5% of initial total mass) and was consistent through the different experiments.

Figure 5.4: The appearance of the different samples right after the completion of the experiments 10-11-12 (from left to right)

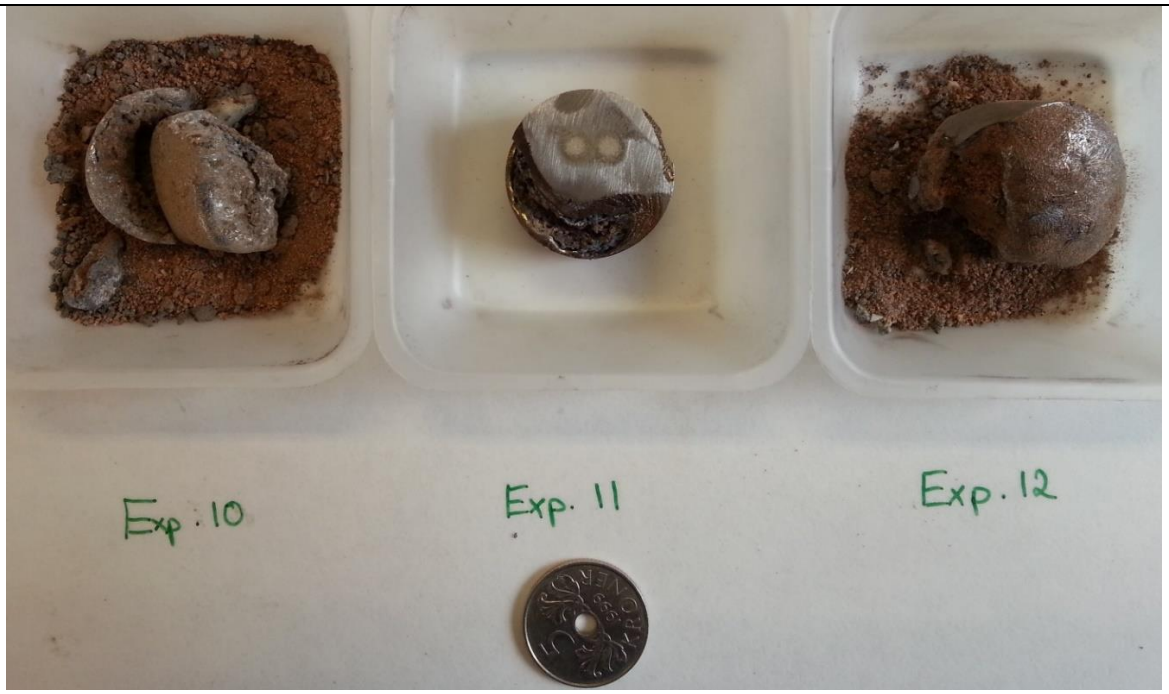

Figure 5.5: The appearance of the different samples after being left couple of days in the air

5.2.3 Spark/carbon analysis

In this section, the iron analysis of the experiments in Set A and B will be presented. However, due to the strong mixing between slag and metal in Set B, it was only possible to analyze the iron sample from experiment 11. The composition of the elements carbon, phosphorus and silicon will be the focus of this section and the detailed analysis for all the different elements can be found in the appendix.

1. **Set A:**

In this set of experiment, analysis was done on four different points on the iron sample from each experiment. The results are shown in Table 5.4. As a reminder, the composition of the slags moves toward higher lime and lower iron oxide contents from experiment 1 to 7. In experiments 8 and 9, silica was added in different amounts (20wt% and 5wt% respectively) while maintaining the iron oxide content 50wt%.

Table 5.4: Chemical composition of the samples from set A of experiments after refining

Experiment	Element					
	C		P		Si	
	Mass %	Std. Dev.	Mass %	Std. Dev.	Mass %	Std. Dev.
Initial (Alloy A)	0.330	0.000	0.285	0.039	<0.001	0.000
1	0.086	0.001	0.283	0.026	<0.001	0.000
2	0.317	0.002	0.010	0.001	<0.001	0.000
3	0.291	0.028	0.011	0.001	<0.001	0.000
4	0.301	0.003	0.006	0.000	<0.001	0.000
5	0.303	0.009	0.006	0.000	<0.001	0.000
6	0.308	0.011	0.004	0.001	<0.001	0.000
7	0.313	0.003	0.006	0.000	<0.001	0.000
8	0.029	0.022	0.017	0.001	<0.001	0.000
9	0.015	0.022	0.003	0.000	<0.001	0.000

In experiment 1, the only significant difference is in the carbon content where it decreased from 0.33wt% to 0.086wt%.

Moving to experiments 2-7, we can see that the carbon content in these samples did not change significantly. However, the phosphorus content decreased. The lowest level achieved was achieved in experiment 6, where it reached 0.004wt%. In addition, it can be noted that the duplicates yielded very similar results. The trend here is that more phosphorus is removed with increasing CaO content.

In experiments 8 and 9, the silica content was 20wt% and 5wt% respectively. The carbon levels in these experiments decreased largely compared to experiments 2-7 and reached 0.015wt% in experiment 9. In addition, phosphorus was also removed with experiment 9 being much more successful (0.003wt% in experiment 9 compared to 0.017wt% in experiment 8).

Moreover, the silicon content in the metal remained negligible in all of the experiment. In addition, even when silica was present in the slag (experiment 8-9), the oxide was not reduced and no silicon was transferred to the metal.

On the other hand, it was possible in Set A to weigh the iron sample at the end of the experiments (as mentioned earlier the slag and iron can be separated from each other). As a result, carbon and phosphorus removal as well as iron loss can be calculated and are given as percentage of the initial amount in Table 5.5.

Table 5.5: Iron loss as well as phosphorus and carbon removal in Set A of experiments

Experiment	% Fe	% P	% C
1	5.41	6.20	75.35
2	9.15	96.96	12.72
3	9.30	96.50	20.02
4	8.30	98.22	16.36
5	8.10	98.08	15.62
6	6.37	98.82	12.61
7	6.82	97.92	11.62
8	5.73	94.14	91.21
9	5.62	98.96	95.45

These results also translate what was already mentioned for phosphorus and carbon earlier in this section. As for iron loss, we can see that it is the lowest in experiment 1. In addition, it is the highest in experiment 3 (9.30%) shows a decreasing trend when moving toward experiment 9 (5.62%).

2. Set B:

In this set, it was only possible to do this type of analysis on experiment 11 due to the strong mixing between the metal and the slag and as a result the absence of a flat metal surface big enough to meet the requirements of the analysis equipment. The chemical composition of the metal in experiment 11 is given in Table 5.6. Moreover, the analysis was only possible on two different points on the iron.

It can be seen that all three elements were removed to some extent from the metal. The amount of carbon was nearly halved (≈4wt% to ≈2wt%) whereas silicon was completely removed. As for phosphorus, its amount decreased from 0.05wt% to 0.011wt%. However, these

observations are not absolutely accurate since the level of phosphorus in the alloy showed big deviations across the different areas and the analysis in experiment 11 only covers two point on the top surface of the metal.

Finally, since the slag and metal were intermixed, it was not possible to measure the final mass of iron. As a result, carbon and phosphorus removal as well as iron loss cannot be presented as in Table 5.5 in the previous section.

Table 5.6: Chemical composition of the iron in experiment 11 after refining compared to that of Alloy B

Experiment	Element					
	C		P		Si	
	Mass %	Std. Dev.	Mass %	Std. Dev.	Mass %	Std. Dev.
Initial (Alloy B)	**3.99**	**0.030**	**0.05**	**0.018**	**0.13**	**0.006**
11	**1.993**	**0.065**	**0.011**	**0.002**	**<0,001**	**0.000**

5.2.4 XRD

The XRD analysis was performed on the powder from the crushed slags in most of the experiments in Set A and Set B. It is important to note that the results from XRD are qualitative where they can only point out the species present but not the exact slag composition. However, the intensities of the peak can give an approximation of the quantities of the different species, e.g. which one is more dominant. The XRD patterns of all the experiments are given in the appendix.

1. **Set A:**

The XRD diffraction patterns are given in figures (5.6-5.10) and the different species present are found in Table 5.7.

Table 5.7 : Species present in the slag from the different experiments accorindg to XRD analysis

Experiment	Species			
	Metallic	Iron oxides only	Calcium oxides only	Others
1 (Figure 5.6)		wustite ($Fe_{0.944}O$)		dicalcium silicate ($Ca_2(SiO_4)$)
2-5 (Figure 5.7)	synthetic iron (Fe)	wustite ($Fe_{0.944}O$)		srebrodolskite ($Ca_2Fe_2O_5$)
6-7 (Figure 5.8)	synthetic iron (Fe)	wustite (FeO)	lime (CaO)	srebrodolskite ($Ca_2Fe_2O_5$)
8 (Figure 5.9)		wustite (FeO)		kirschsteinite ($CaFe^{+2}(SiO_4)$)
9 (Figure 5.10)	synthetic iron (Fe)	wustite ($Fe_{0.9}O$)	lime (CaO)	srebrodolskite ($Ca_2Fe_2O_5$) kilchoanite ($Ca_6.SiO_4.Si_3O_{10}$)

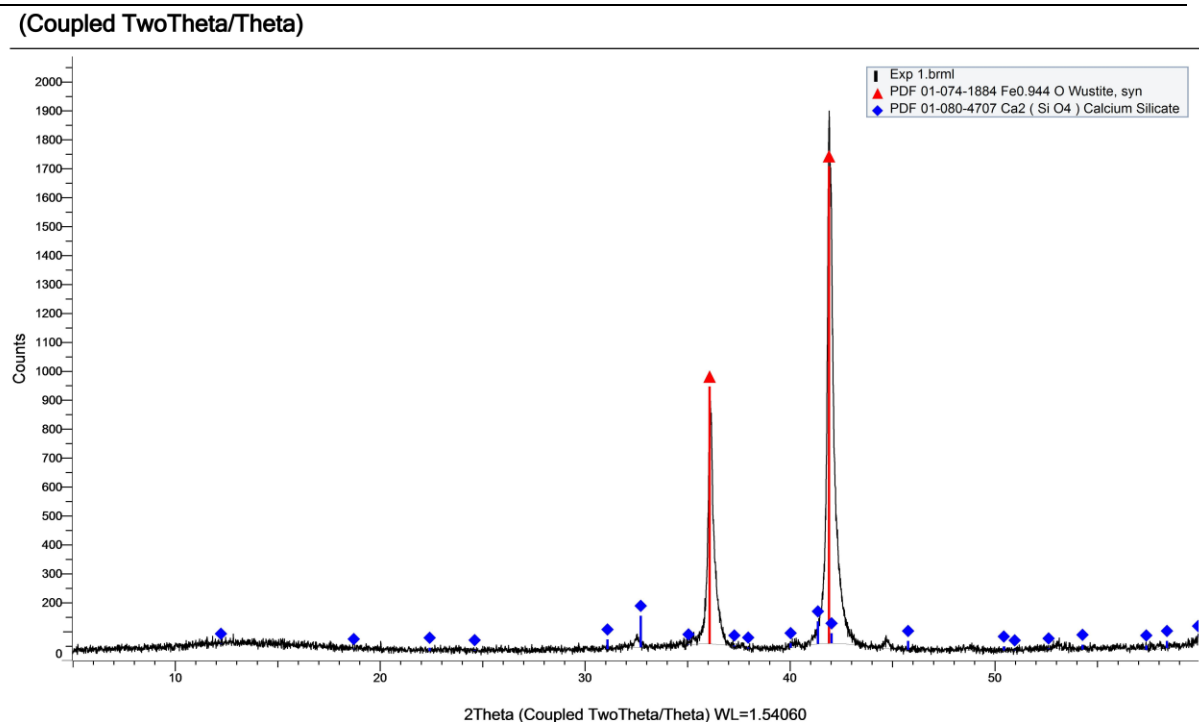

Figure 5.6: XRD pattern of the slag powder in experiment 1

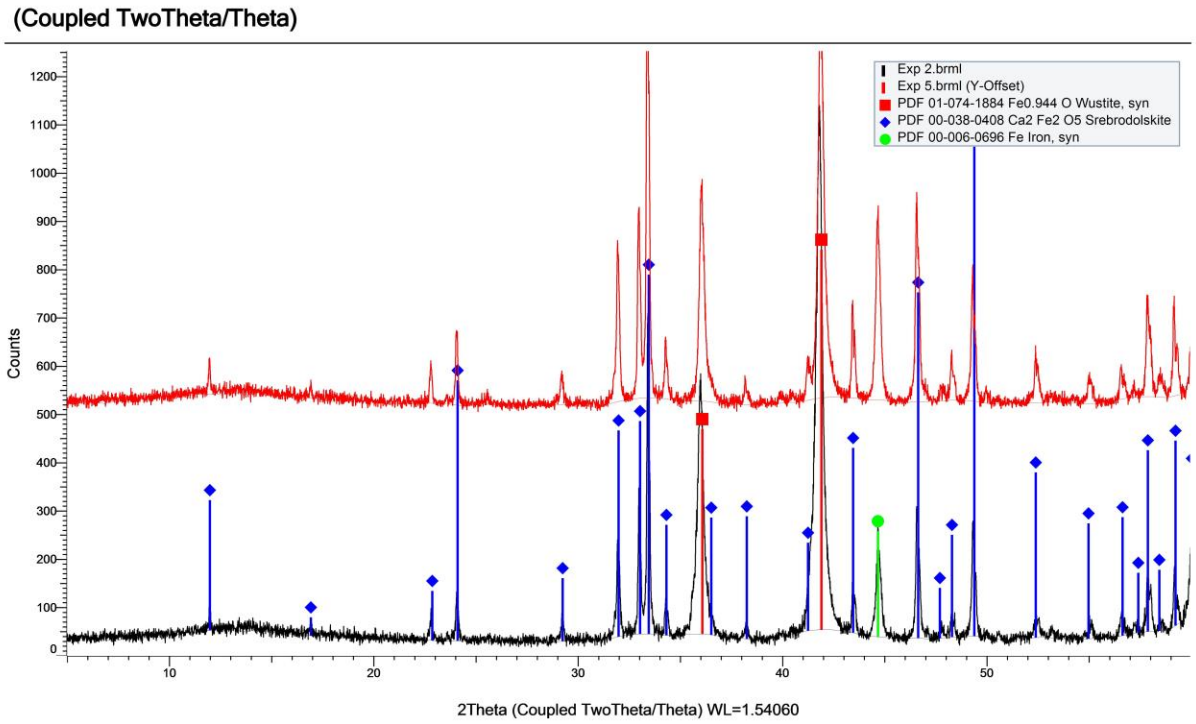

Figure 5.7: XRD pattern of the slag powder in experiment 2 and 5

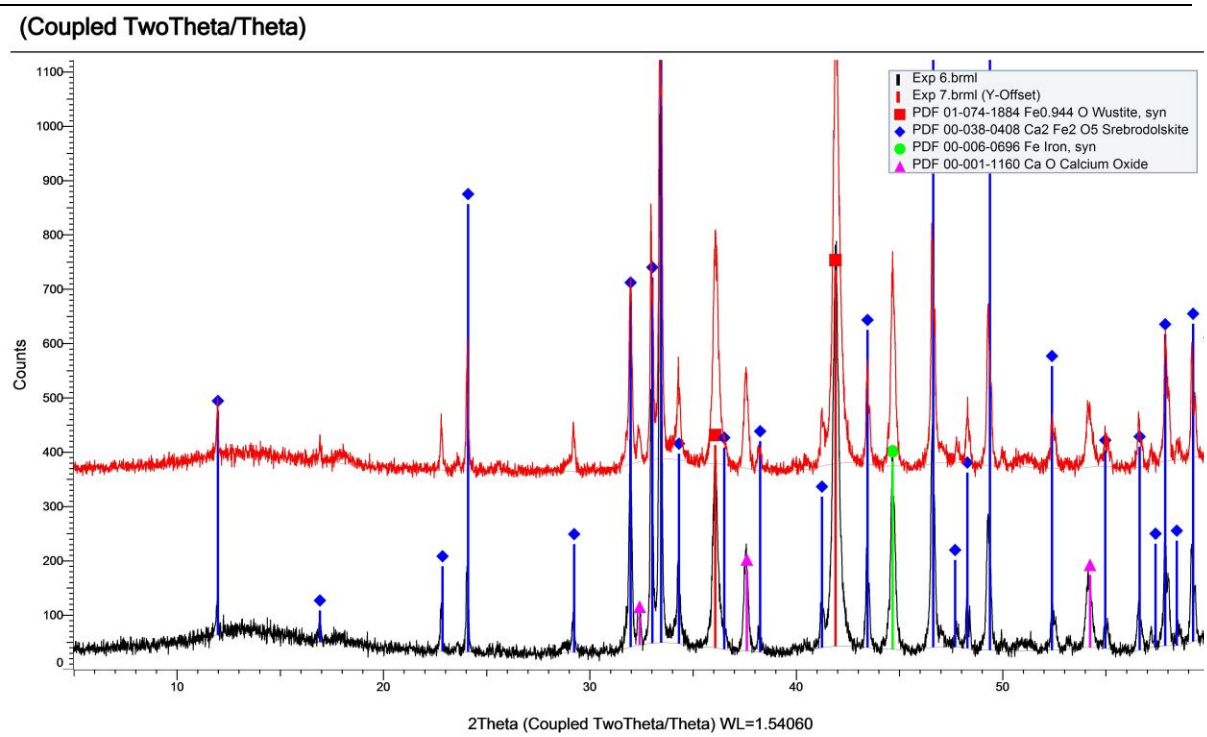

Figure 5.8: XRD pattern of the slag powder in experiment 6 and 7

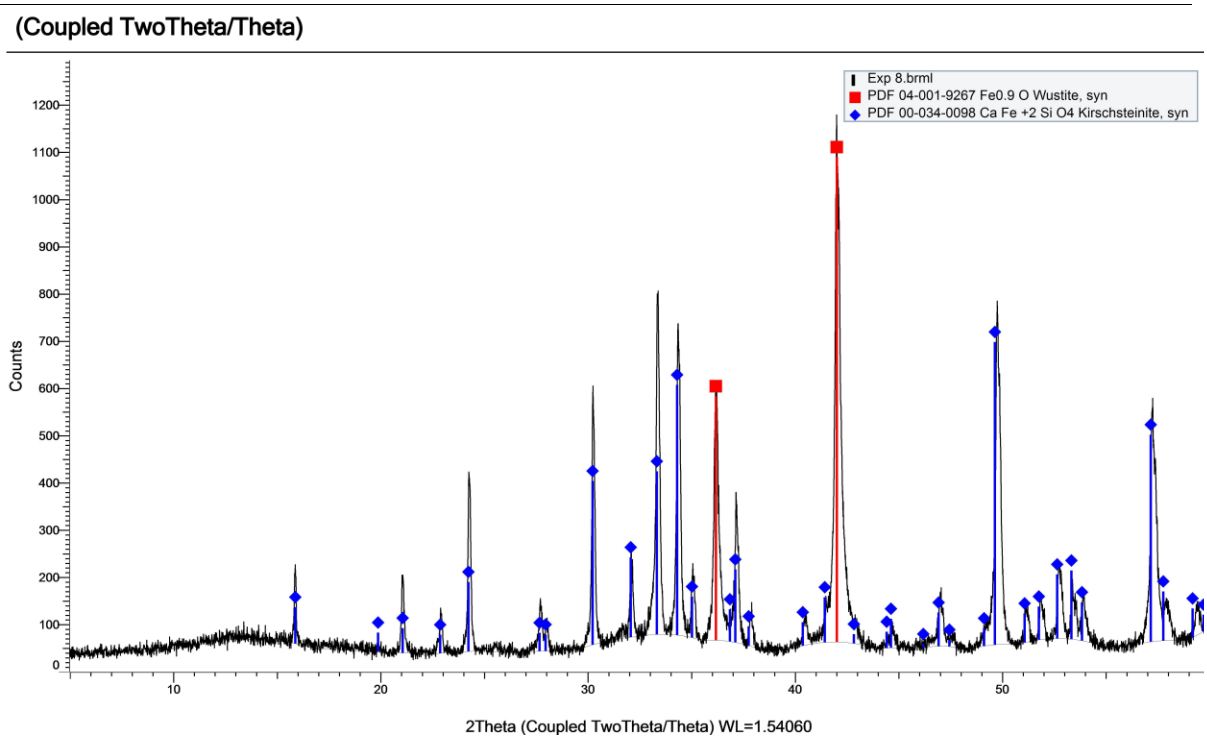

Figure 5.9: XRD pattern of the slag powder in experiment 8

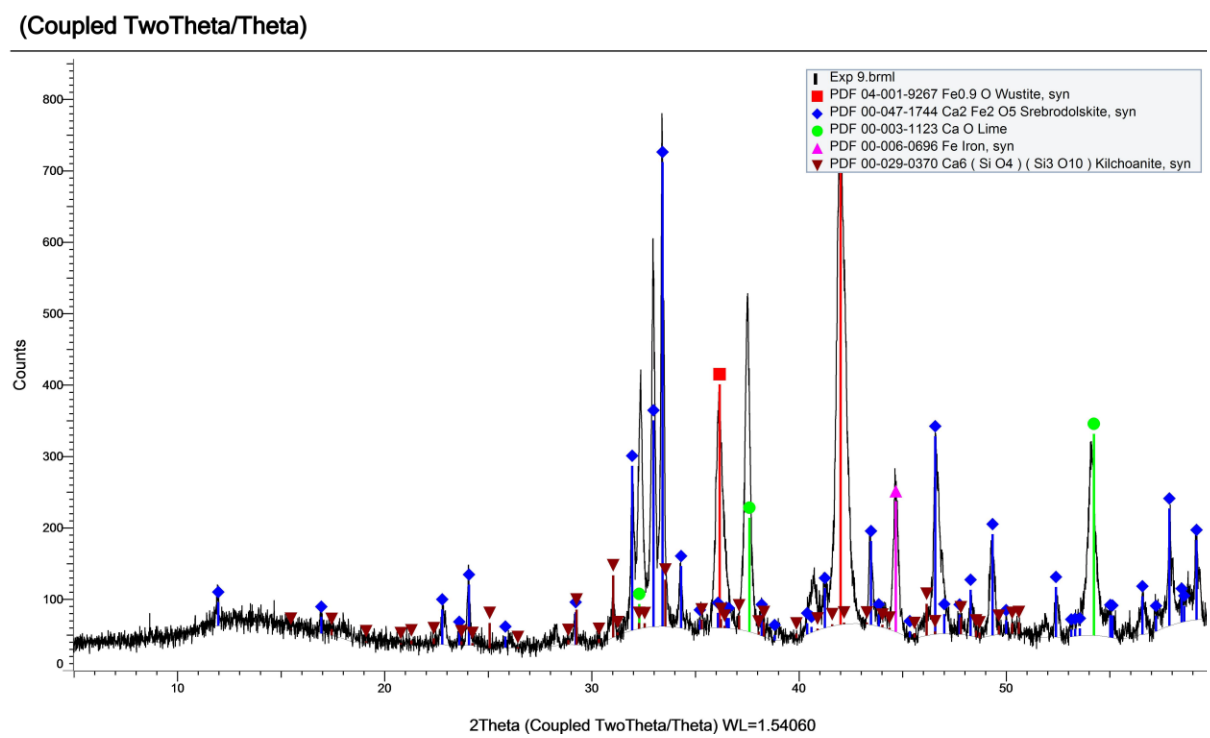

Figure 5.10: XRD pattern of the slag powder in experiment 9

2. Set B:

The slag from experiment 10 and 12 were the only ones to be analyzed by XRD. In experiment 10, it was possible to carry out the analysis both on the dark grey and brownish slag.

In experiment 10a (Figure 5.11), where the 'a' stands for grey slag, the main component is synthetic iron. In addition, three other components are present Hatrurite ($Ca_3(SiO_4)O$), Lime (CaO) and Magnesium-Iron oxide ($Mg_{1-x}Fe_xO$). Lastly, some small quantity of Portlandite ($Ca(OH)_2$) also exist.

In experiment 10b and 12b (Figure 5.11), where the 'b' stands for brown slag, the XRD patterns are similar where only the intensities of the peaks is slightly different and they are also similar to experiment 10a. However, in these two experiments, synthetic iron is no longer the dominant species and all the different components exist in approximately equal amounts. And we can see that the quantity of Portlandite ($Ca(OH)_2$) increases drastically.

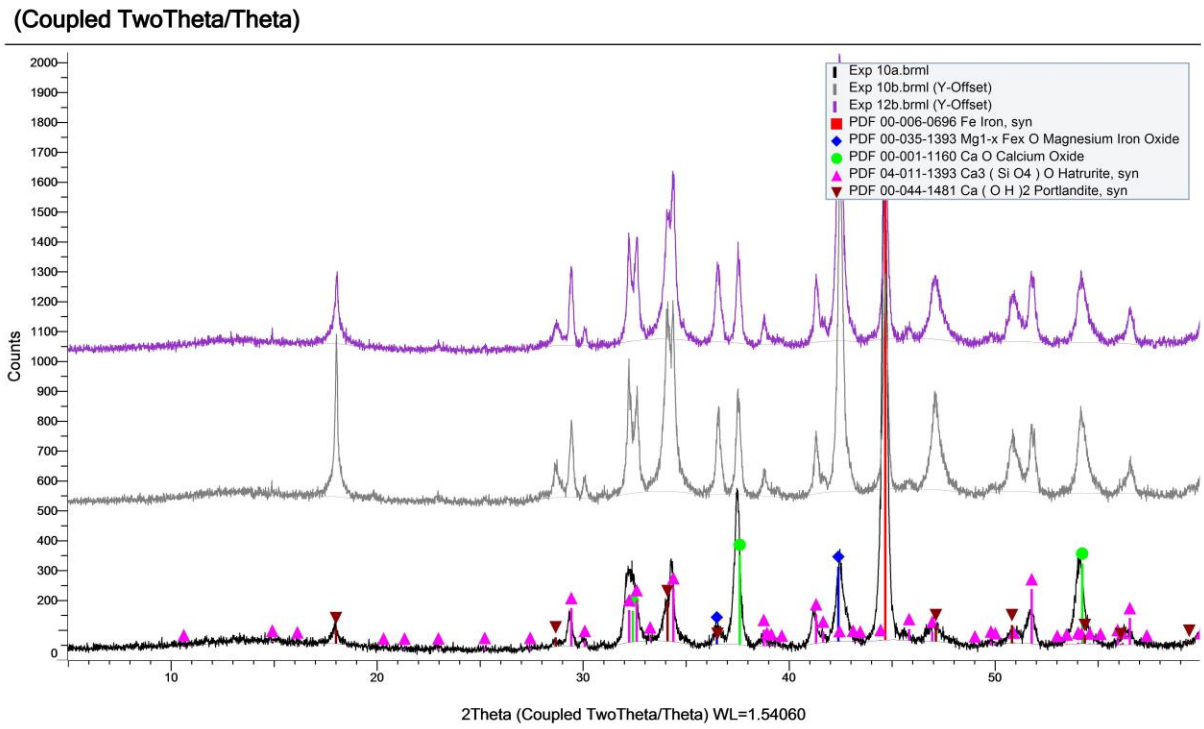

Figure 5.11: XRD pattern of the slag powder in experiments 10a, 10b and 12b

5.2.5 EPMA

EPMA analysis was only carried on Set B of experiments. It can be divided into three parts: imaging, quantitative point analysis and quantitative mapping. The images showing the most important features will be presented in this section and the rest will be available in the appendix.

The different samples used for EPMA can be seen in Figure 5.12. It can be noted that two different parts from experiment 10 were analyzed (named 10.1, 10.2).

Figure 5.12: Different samples used for EPMA (from left to right: experiment 10.1, 10.2, 11, 12)

1. Imaging/quantitative point analysis:

All the figures below show that the metal and slag are intermixed and the mixture is very porous. In addition, we can see that different phases in the slag exist by looking at the color, shape or surface topology. In all the experiments, three slag phases exist: CaO rich phase, CaO-SiO_2 phase and MgO-FeO phase. However, the appearance of these phases is not identical across all the figures, and it is important to refer to the quantitative point analysis. It is worth noting that the total amount of all elements is more than 100wt%. This is due to the surface topology, since it is not perfectly flat and due to the inaccuracy in measuring the carbon levels due to interference from the carbon coating (part of the sample preparation).

One important observation that can be made is that the phosphorus levels tend to be higher in the CaO containing phase than the levels of the metal. For example, by looking at Figure 5.13, points 1-3 which are located in the metal contain P levels between (0wt%-0.042wt%) and then by moving to points 7-9 which are located in the CaO containing phases these levels rises and range between (0.759wt%-2.161wt%).

As for silicon, it can be seen across all the figures that silicon content in the metallic iron is very small, which is in line with that observed in the spark analysis. In addition, it can also be seen that the silicon levels are lower in the main body of the metal and relatively higher in the iron droplets found in the slag phase. So if we take a look at Figure 5.13 , looking at point 1-3 which are located in the main body of the metal the levels of silicon ranged between (0wt%-0.048wt%) , and by moving to the iron droplets, depicted by points 4-6, the silicon levels rise and range between (0.142wt%-0.184wt%).

Moreover, accurate observations related to carbon distribution cannot be made because the carbon coating of the samples interfere with the analysis and might lead to false conclusions. In addition, we can see that aluminum levels in both slag and metal are very low across all the samples.

The final point to be made here is that these observations might or might not be valid for the whole metal-slag volume since the analysis in only carried on very small areas. However, since results from imaging on wider areas have shown similar patterns, we can assume that these results can describe the totality of the metal-slag volume.

Figure 5.13: Surface image and point analysis of experiment 10.1

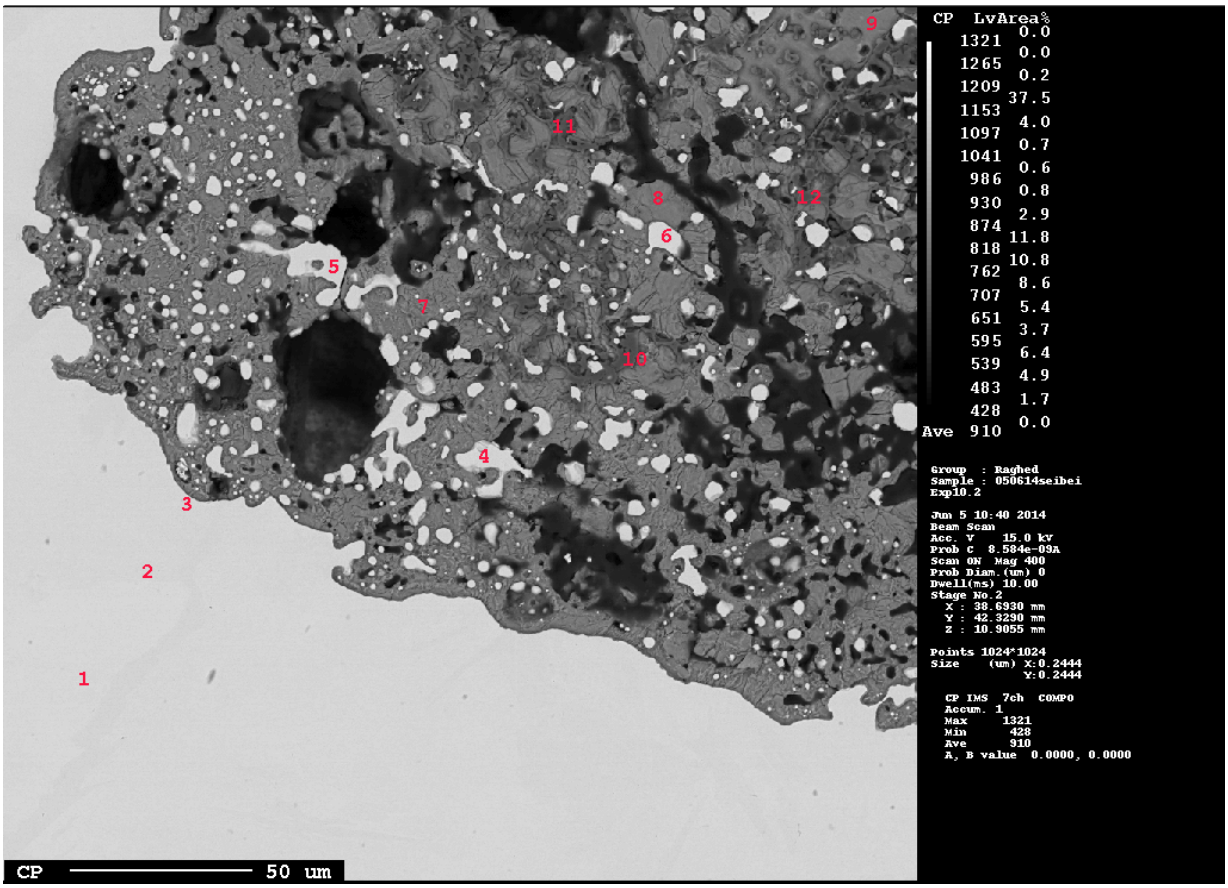

Point	Composition (mass %)								Total
	Mg	O	P	C	Al	Ca	Si	Fe	
1	0	0.252	0.042	8.376	0	0	0.02	101.28	109.97
2	0	0.238	0	8.308	0.01	0	0	101.79	110.346
3	0.004	0.326	0	8.456	0	0.308	0.048	100.859	110.001
4	0.052	0.57	0.08	8.969	0	1.049	0.184	99.23	110.134
5	0.016	0.455	0.619	8.37	0	0.978	0.142	100.101	110.681
6	0.25	0.487	1	8.251	0	1.421	0.184	98.278	109.871
7	0.332	27.653	0.759	9.964	0.09	45.42	15.29	1.018	100.526
8	0.17	30.845	2.161	8.605	0.054	45.597	14.061	0.841	102.334
9	0.518	26.085	1.473	9.738	0.028	51.255	10.804	0.815	100.716
10	55.442	41.051	0.039	10.565	0.002	3	0.62	0.776	111.495
11	58.076	39.011	0.033	10.743	0	1.176	0.105	1.069	110.213
12	57.614	39.971	0.058	11.071	0	1.457	0.331	0.713	111.215

Figure 5.14: Surface image and point analysis of experiment 10.2

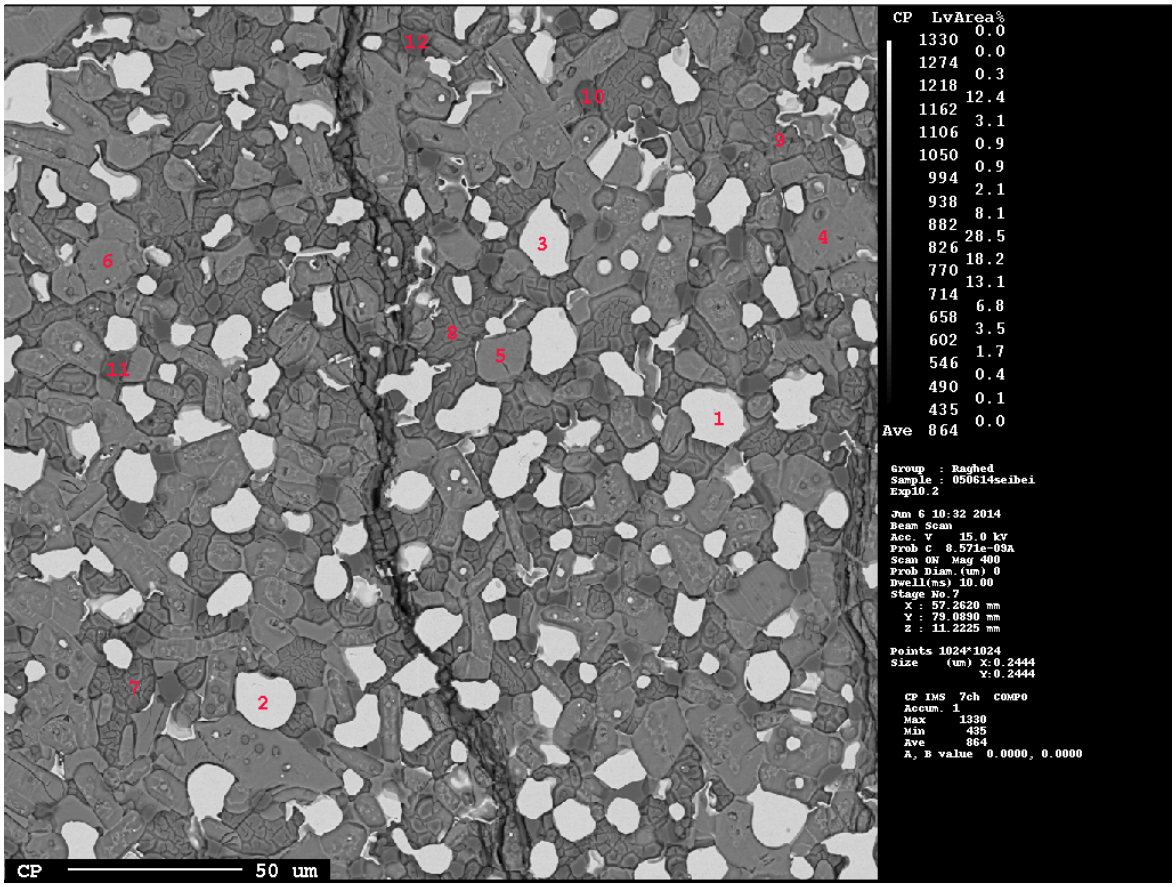

Point	Composition (mass %)								Total
	Mg	O	P	C	Al	Ca	Si	Fe	
1	0.135	0.607	0.017	3.584	0.005	1.301	0.119	101.19	106.958
2	0.099	0.466	0.015	3.36	0	1.298	0.118	101.243	106.599
3	0.13	0.48	0.004	3.402	0	1.188	0.091	101.313	106.608
4	0.302	32.45	0.602	3.891	0.093	51.482	10.964	2.048	101.832
5	0.817	32.036	0.446	3.471	0.055	50.547	11.1	2.098	100.57
6	0.409	32.733	1.046	3.533	0.071	52.046	10.955	1.737	102.53
7	3.122	38.157	0.01	5.907	0.015	57.65	0.606	7.139	112.606
8	2.378	36.208	0.009	5.963	0.036	59.469	0.579	6.873	111.515
9	2.862	36.349	0.022	6.513	0	56.848	0.529	7.884	111.007
10	49.84	39.685	0.004	4.645	0.012	1.682	0.134	9.732	105.734
11	49.521	38.946	0	4.495	0	1.667	0.149	10.905	105.683
12	48.296	38.252	0.029	4.525	0.01	1.942	0.154	11.136	104.344

Figure 5.15: Surface image and point analysis of experiment 11

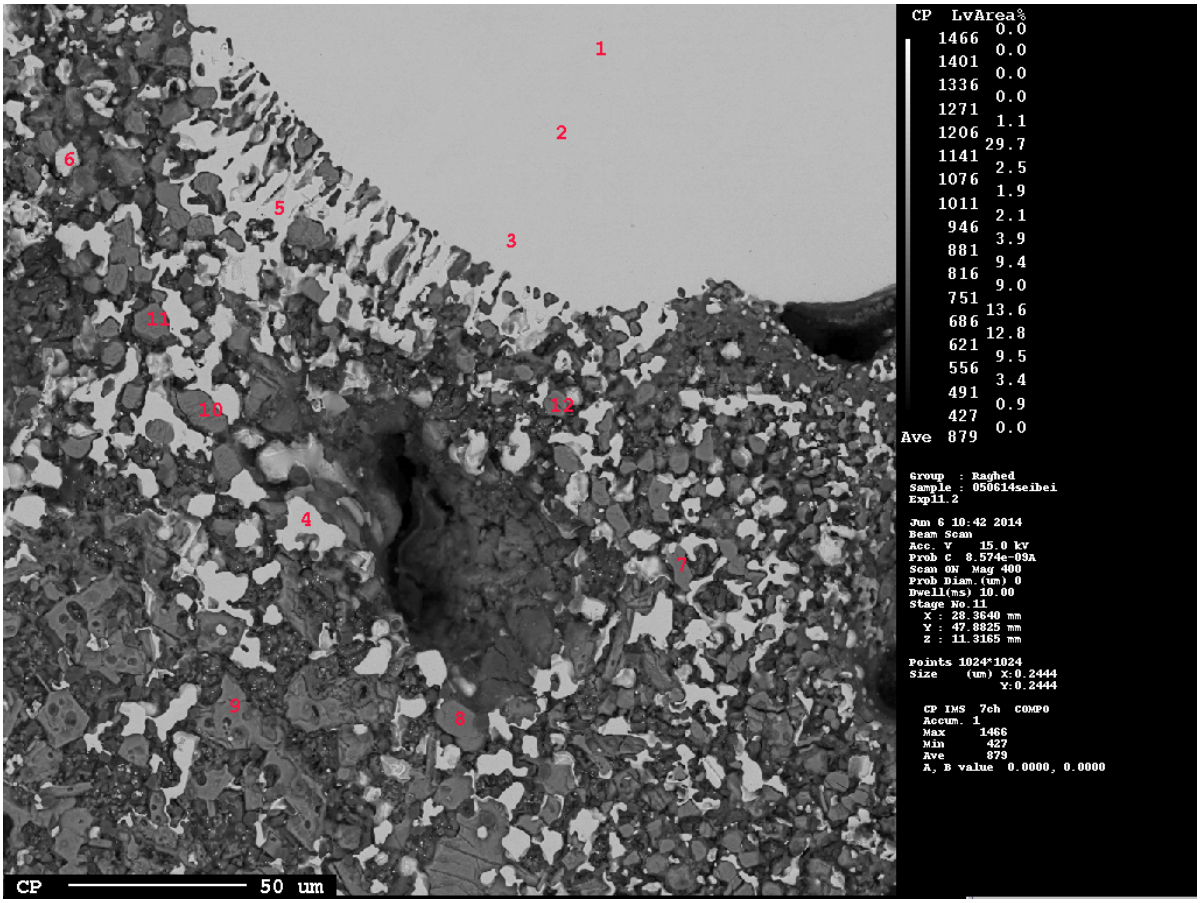

Point	Composition (mass %)								Total
	Mg	O	P	C	Al	Ca	Si	Fe	
1	0.004	0.162	0.013	4.524	0.011	0	0	103.285	107.999
2	0.023	0.195	0.013	3.969	0.002	0	0	102.175	106.377
3	0.061	0.244	0	4.455	0	0.074	0.022	100.479	105.335
4	0.067	0.498	0.021	4.605	0	0.74	0	96.64	102.571
5	0.048	0.336	0.017	4.528	0	0.663	0	96.612	102.204
6	0.099	0.343	0.023	4.847	0.003	0.64	0	92.589	98.544
7	0.241	28.778	2.485	4.62	0.056	39.886	12.705	1.733	90.504
8	0.198	31.567	2.046	4.488	0.043	40.072	12.401	1.333	92.148
9	0.512	33.349	0.931	4.794	0.066	49.02	10.936	0.769	100.377
10	0.238	29.228	2.129	5.076	0.055	43.426	13.169	1.965	95.286
11	0.474	30.043	0.835	4.416	0.039	49.099	11.321	1.494	97.721
12	0.173	28.219	2.316	5.259	0.053	43.701	13.674	1.773	95.168

Figure 5.16: Surface image and point analysis of experiment 12

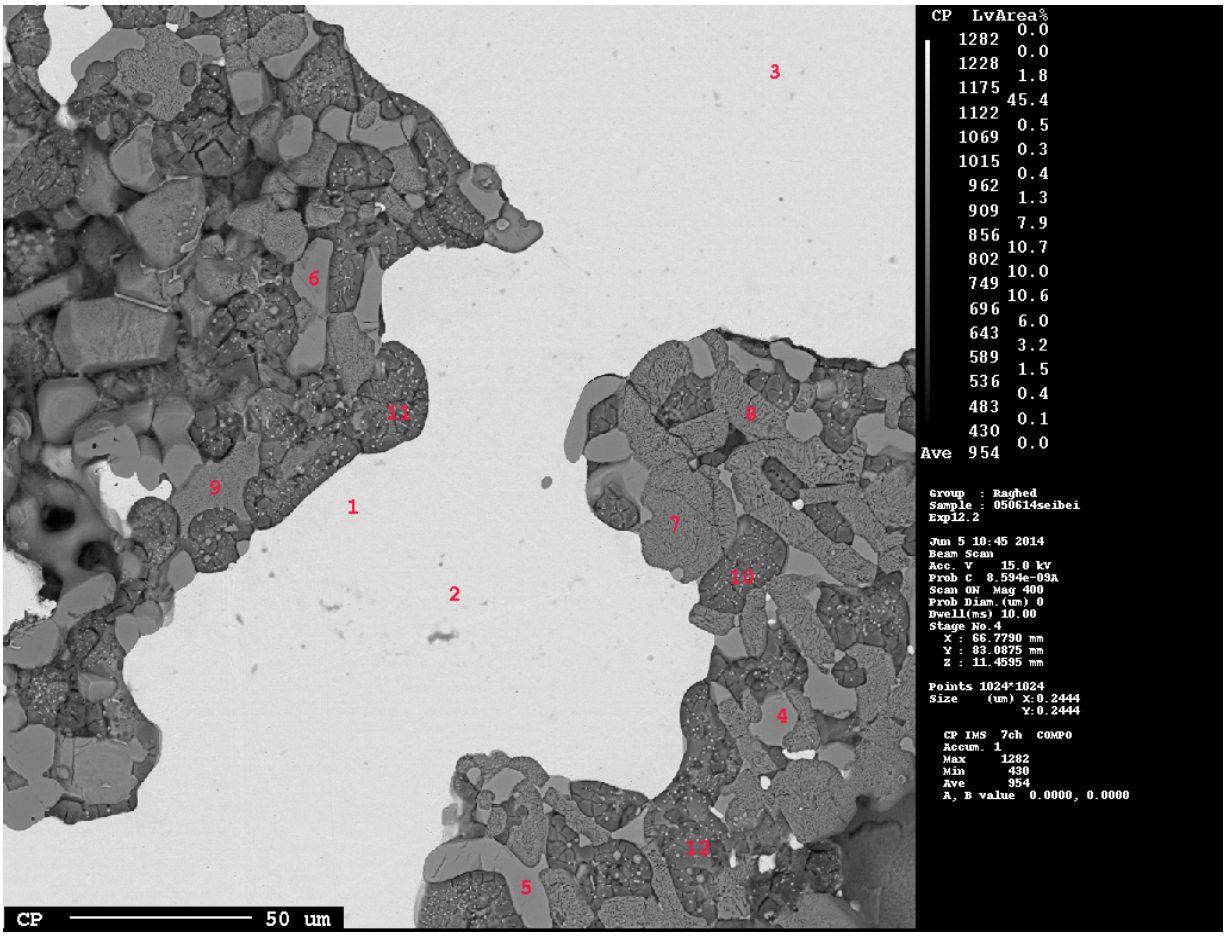

Point	Composition (mass %)								Total
	Mg	O	P	C	Al	Ca	Si	Fe	
1	0.098	0.464	0.021	7.676	0	0.295	0	102.331	110.885
2	0.025	0.333	0	7.557	0	0	0.01	102.651	110.576
3	0	0.285	0	7.535	0	0	0	102.814	110.634
4	26.631	31.087	0	8.593	0.01	1.853	0.133	39.695	108.002
5	25.988	30.436	0	8.473	0	1.73	0.019	41.029	107.675
6	31.398	29.975	0	8.946	0.017	1.779	0.077	35.063	107.255
7	0.217	29.977	0.405	9.205	0.07	46.295	12.907	3.358	102.434
8	0.134	29.719	0.407	11.266	0.101	42.311	13.634	2.764	100.336
9	0.387	31.783	0.267	8.503	0.036	46.444	12.978	3.37	103.768
10	2.625	36.985	0.012	13.596	0.031	47.213	0.433	14.59	115.485
11	2.916	30.673	0.019	11.683	0.019	51.182	0.336	11.918	108.746
12	0.366	31.227	0.005	15.8	0.011	54.244	0.402	6.277	108.332

1. Quantitative Mapping:

It was only carried out on the samples from experiment 10.1 and 12 due to time constraints. In this section, results from experiment 10.1 will be presented since they offer a complete overview of the situation in the different experiments. The results from the other experiment are available in the appendix.

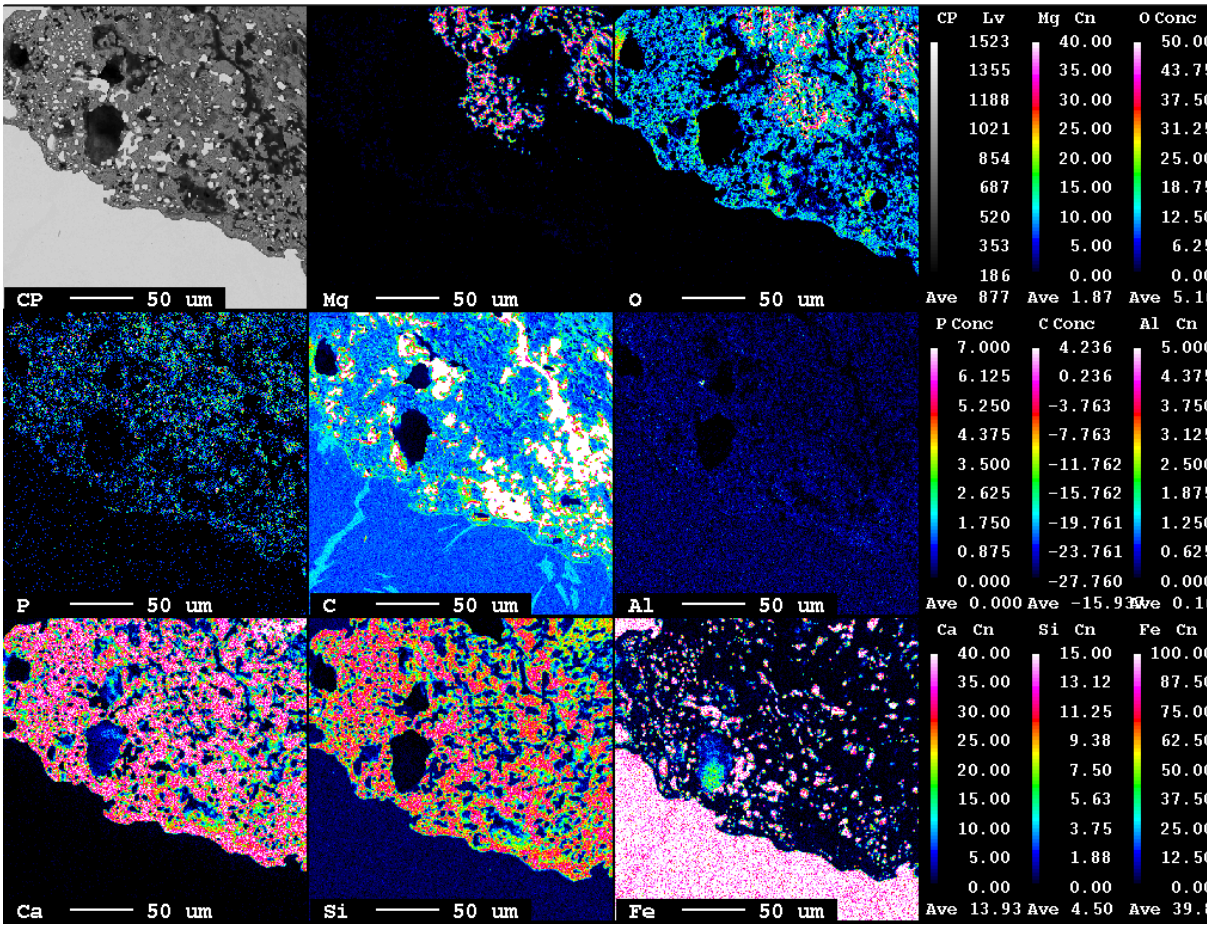

Figure 5.17: Quantitative mapping of the sample in experiment 10.1

Figure 5.17 show the quantitative mapping of the same area presented in Figure 5.13. By looking at O distribution, we can see it is exclusively present in the slag phase which also exclusively contain the Ca, Si and Mg. As for iron, it is present in the biggest amount in the bottom of the area (the metal) and in lower quantities in the slag most probably as FeO. For phosphorus, we can see that it is present in the highest amounts in the slag phase (green color). The interesting observation is related to carbon, where it can be seen that it is segregating in the metal and is found in larger amounts in the interface between slag and metal (light blue lines).

6 Discussion

6.1 Iron alloys

6.1.1 Alloy A

As it can be seen from table 1 and 2, phosphorus levels were increased in the alloy A to the desired levels and the re-melting assured homogenous composition. This is related to the fact that upon re-melting the metal will be mixed. In addition, the use of pure iron phosphide kept the alloy relatively pure where no significant impurities were introduced in the metal. As for the relatively high carbon level, its main source might be the graphite crucible used as protection. Since, at high temperature, some carbon dust might have been formed which later contaminated the metal.

6.1.2 Alloy B

By comparing the composition of Fe-800 (Table 4.1) and that of alloy B (Table 5.3) it can be seen that phosphorus level was not increased as was expected. In addition, segregation was also observed even after a series of re-melts (high standard deviation). This can be attributed to the fact that industrial iron phosphide was used which was in the form of small lumps. The appearance of these lumps showed big variations with some showing shiny silver color, which might be caused by high iron levels. Hence, the composition of the iron phosphide in single lumps might not be the same as stated in Table 4.2. This discrepancy might introduce errors when calculating the amount of iron phosphide needed and hence lead to the observed result.

6.2 Refining experiments

6.2.1 Physical appearance

1. **Set A:**

In experiment 1, the metal:slag ratio of 5:1 was deemed insufficient since it wasn't covering the whole surface of the metal and lead to the use of a 2.5:1 ratio in later experiments. In addition, the presence of wustite in the slag (reaction between iron and iron (III) oxide gave it the dark grey color (Figure 5.3). Moving to experiments 2-9, the slag color changed to lighter shades of grey. This can be explained by the fact that calcium oxide and silica (only in experiments 8-9) were present, which have white color.

The perfect separation between slag and metal might be related to the fact that pure iron was used which have high melting temperature. As a result, upon cooling the metal solidified first and due to its high density will have solidified at the bottom, which then was covered by the

slag. In addition, when silica was added, the metal and slag were easily separated which can be explained by the fact that silicate slags have higher viscosity and form glassy slags (figure).

Finally, the combined mass of crucible, metal and slag remained approximately constant which can be explained by the fact that the experiments were carried out in argon atmosphere and as a result what leaved the metal will have to enter the slag and no further oxidation into the atmosphere could take place.

2. **Set B:**

The results in this set of experiments differ greatly from Set A. Although the slag composition in these experiments is similar to that of experiment 9, strong mixing and even emulsification between the metal and slag was observed in Set B (Figure 5.4). The only major difference is the carbon content in the iron from Alloy B. The carbon level has been increased from 0.33wt% to 3.99wt%. This affect will the properties of the iron melt directly and indirectly those of the slag. First, the melting point of iron with 4wt% carbon is around 1200^0C (from 1538^0C for pure iron) and the slag has a melting temperature around 1450^0C. In this case, the slag will solidify first and iron droplets can be trapped inside the slag. Secondly, the surface tension of liquid iron is dramatically reduced at high carbon levels where it decreases from 1600 ergs/cm^2 for pure iron to 1200 ergs/cm^2 at 4wt% carbon [47]. This will lead to an enhanced mixing effect. Moreover, the viscosity of iron is also lowered from ≈6.2cp for pure iron to ≈4.8cp for iron with 4.4wt% carbon at 1600^0C [47]. To summarize, it can be noted that the increased carbon content in the metal will change its properties and might lead to a better mixing and emulsification.

On the other hand, the carbon content was reduced at the end of these experiments to ≈2wt%. The carbon lost could have reduced some of the iron oxide in the slag and hence changing its composition and moving the equilibrium to another area of the CaO-SiO_2-FeO phase diagram. In addition, if the carbon was removed as CO_2 (an assumption since the outlet gas was not analyzed during the refining experiments), it will enhance the stirring in the melt and might lead to the observed physical appearance. In addition, this fact might also explain the presence of the small iron droplets on the surface of the crucible.

As for the loss in the combined mass of crucible, metal and slag at the end of the experiments, it can be explained by both the reduction in the carbon content and by the fact that the small iron droplets imply that some iron might have been also lost from the crucible.

Finally, for the observed disintegration of the slag (Figure 5.5), where it changed color from grey to brown, two possible explanations can be given. First, some of the slag components were not stable and after being left in the air the slag composition was changed. The second might be due to reaction with water since when the crucibles were cut, water was used to cool the blade. However, the XRD analysis did not show any major difference in the components of the two slags, the only difference was in the amount of each component.

6.2.2 Spark analysis

1. **Set A:** (Table 5.4, Table 5.5)

In experiment 1, around 75% of the carbon content was lost. This was expected since in this experiment iron and iron oxide were the only components of the system and carbon would have reduced some of the iron oxide in the slag. On the other hand, phosphorus levels remained constant which can be explained by the absence of lime since phosphorus can be only removed from the iron as calcium phosphates in the slag according to Reaction 3.10. Lastly, iron loss in this experiment was the smallest since the metal to slag ratio was the biggest, and hence only a small amount of iron reacted with iron (III) oxide.

Moving to experiments 2-7, the carbon loss was much smaller, ranging between (11.62%-20.02%). The main reason behind this observation is that some of the iron oxide will be bound to the lime forming stable compounds that could not be reduced by carbon. On the other hand, dephosphorization was very successful and between 96%-99% of the phosphorus was removed lowering its level in the metal to the desired levels (<0.03 wt%). The best dephosphorization was observed with the highest lime contents (experiments 6-7) which is to be expected since lime will lower the activity of P_2O_5. In addition, the high slag volume will also enhance dephosphorization by both diluting the P_2O_5 and by increasing the oxygen potential in the slag. Lastly, iron loss decreases by moving from experiment 2 to 7, which is explained by the decreasing amount of Fe_2O_3 in the slag reacting with iron according to the following equation:

Reaction 6.1

$$(Fe_2O_3) + [Fe] = 3(FeO)$$

For experiments 8-9, carbon loss increased drastically to above 90%. The possible explanation is first that silica addition to the slag will lead to the formation of calcium silicate compounds instead of iron oxide and lime compounds. Hence, an increased quantity of free iron oxide exists in the slag, which can be reduced by carbon. As for dephosphorization, it can be seen that only big additions of silica (experiment 8) will affect the process. But still the slag was effective in removing up to 95% of P. This can be explained by the fact that silica will bound to lime, and as a result less free lime will be available in the slag and hence P_2O_5 will slightly increase. In addition, silica will consume some of the free oxygen in the slag melt (to form silicates) hence reducing the oxygen potential. Moreover, the increased viscosity in silicate melts can lower the mass transfer coefficient of the impurities in the slag. In experiment 9, the effect of silica addition was masked by the increased lime content (45%), which in turn lead to the best dephosphorization results observed (99% removal). Lastly, the iron loss in these experiments was the lowest since the amount of Iron (III) oxide in these slags was the lowest.

To sum up, all of these observations fall in line with those encountered in the literature and discussed in an early part of the thesis where high CaO and FeO contents, low SiO_2 contents and large slag volume will lead to a better dephosphorization.

2. **Set B:** (Table 5.6)

As it was mentioned before, the iron from experiment 11 was the only sample to be analyzed and data from only two points was possible to collect. In this experiment, the decrease in the carbon level was high which is similar to what was observed in case of experiment 9 in Set A. This can be related to the fact that the same slag composition was used in this experiment and hence big quantity of free iron oxide exist in the slag, which can be reduced by carbon. As for phosphorus, its amount has been decreased from 0.05% to 0.011%. As was mentioned before, this is due to the fact that phosphorus will be oxidized to P_2O_5 and then transferred to the slag as calcium phosphates. Finally, silicon was completely removed. The main explanation revolves around the oxidation of Si to SiO_2 due to the high oxidation potential of the slag. However, all of these observation can serve only as a qualitative reference since the analysis was only done on two points and they only represent a small proportion of the metal and might be as a result just a local distribution.

6.2.3 XRD

1. **Set A:**

In experiment 1, the main slag component is wustite (FeO). The main reason behind this observation is the reducing conditions in the experiments since hematite (Fe_2O_3) is in equilibrium with Fe under argon atmosphere. As a result, the following reaction will take place:

As a result, hematite will be replaced by wustite in the molten slag. However, by looking at the phase diagram (Figure 3.10) wustite should not be stable at low temperatures and will be replaced by magnetite (Fe_3O_4). Nevertheless, the presence of wustite can be explained by the fact that the sample was cooled fast enough for it to remain a stable phase and hence thermodynamic equilibrium was not reached. As for the presence of dicalcium silicate, the only possible explanation is that it was formed from the impurities either in the slag or in the metal since it is found in very small quantities.

Moving to experiments 2-5, which showed the same XRD pattern but with varying intensities for the different species, the two main components are wustite (FeO) and srebrodolskite ($Ca_2Fe_2O_5$) and synthetic iron is also present. By looking at the phase diagram in Figure 3.11 between 17-25wt% CaO, the stable phases, at high temperatures, are Fe, $Ca_2Fe_2O_5$ and calciowustite. At lower temperatures, calciowustite will change to ($CaO.FeO.Fe_2O_3$). However, this species was not detected in XRD analysis. The only reason which can help explain this observation might be related to rapid cooling and its ability to stabilize these phases.

In experiments 6-7, the CaO content increases to ≈35wt%, the XRD showed that the main species are wustite (FeO) and srebrodolskite ($Ca_2Fe_2O_5$). In addition, lime (CaO) and synthetic iron are also present. The presence of Fe, FeO and $Ca_2Fe_2O_5$ can be explained by referring to the phase diagram (Figure 3.11) where it can be seen that these phases should be stable in this region. However, the reason behind the presence of wustite is unclear.

In experiment 8, where silicate slag (50 wt% FeO, 30wt% CaO, 20wt% SiO2) was used, two main components exist Kirschsteinite ($CaFe^{+2}(SiO_4)$) and wustite (FeO). Kirschsteinite is a member of the olivine mineral group. By looking at the phase diagram (Figure 3.18), it can be seen that it lies on the borders of the olivine and wustite region. This explains why the two aforementioned components were obtained.

In experiment 9, three main components exist srebrodolskite ($Ca_2Fe_2O_5$), lime (CaO) and wustite ($Fe_{0.9}O$). In addition, synthetic iron (Fe) and a very small quantity of Kilchoanite ($Ca_6.SiO_4.Si_3O_{10}$) also exist. According to the phase diagram in (Figure 3.18), it is seen that it lies in the region of the subsystem $3CaO.SiO_2$, CaO and FeO_n, however this is only true at high temperatures. Upon cooling down, the system will change and other phases might be formed. The presence of wustite (FeO) and srebrodolskite ($Ca_2Fe_2O_5$), in addition to lime (CaO) and synthetic iron agree with what was observed in experiment 6-7 where high amount of lime were used. Moreover, since this is a ternary system, the presence of all these species is justified.

Finally, it should be pointed out that the absence of phosphate containing species in the experiments where refining was successful (experiment 2-9) is likely due to the technical limitations of the XRD analyzer where the limit for detection is 0.5wt%. Therefore, the phosphate species theoretically should be present but in small quantities, which is to be expected since the levels of P in the metal, are lower than 0.3wt%.

2. Set B:

All the experiments in this set showed the same XRD pattern but with carrying intensities. The main components are synthetic iron, hatrurite ($Ca_3(SiO_4)O$), lime (CaO) and magnesium-iron oxide ($Mg_{1-x}Fe_xO$). Lastly, portlandite ($Ca(OH)_2$) also exist. The first thing to note here is the presence of magnesium containing compounds which wasn't detected before. However, this is not unexpected since the crucible material is magnesia. One of the reasons that might have led to this change is the reduction of Fe_2O_3 in the slag by the high carbon content in the metal. This might have shifted the equilibrium to a different region in the phase diagram where MgO can substitute for CaO. The other interesting observation is the presence of portlandite ($Ca(OH)_2$). This helps explain why the slag has disintegrated by assuming that some of the calcium containing species have reacted with water (used when the samples were cut) or with moisture in the air. The reason why such reaction took place is the high porosity of the slag obtained in

these experiments. All other species observed in the analysis can all be possibly formed in this system.

In the end, I would like to point out that the phase diagrams predict the possible species that might be present. However, And due to the small scale of my experiments, cooling is relatively fast and the species that should be present at equilibrium under normal conditions, might not be present in this work.

6.2.4 EPMA

As was mentioned before, the different figures shows the metal and slag are intermixed and the mixture is very porous. In addition, different phases in the slag cab be seen by looking at the color, shape or surface topology. In all the experiments, three slag phases exist: CaO rich phase, $CaO\text{-}SiO_2$ phase and MgO-FeO phase. For example by looking at Figure 5.13, the slag phase and the metal phase show some sort of boundary layer and some small iron droplets can be found in the slag. These small iron droplets are the reason why synthetic Fe was observed in the XRD pattern. However, by looking at Figure 5.14, it can be seen that the iron is more dispersed in the slag and different slag phases can be identified. By looking at the quantitative point analysis, three slag phases exist: Ca-rich region, which might be either Lime (CaO) or Portlandite (Ca(OH)2) based on the XRD analysis, Ca-Si-O phase which is the Hatrurite (Ca3(SiO4)O) species and an Mg-Fe-O phase which is the Magnesium-Iron oxide (Mg1-xFexO) species. Moreover, it is interesting to note that in different areas of the sample the distribution of these species differs. For example, by looking at Figure 5.15, it can be seen that only the iron and Ca-Si-O phase exist. In the oxide phase, high levels of phosphorus were observed and strong intermixing is observed hence it can be concluded that dephosphorization occur in this region and the Ca-Si-O phase is the main dephosphorizing agent. All of these observations agree with the physical appearance of the samples, where in some areas the metal and slag phases are well separated whereas in other parts of the samples small iron droplets can be seen in the slag and these parts are especially porous.

Lastly by looking at the mapping (Figure 5.17), one can get a qualitative overview of what is happening. The most interesting observation is the fact that phosphorus is mainly present in the slag phase. This was expected since removal of the phosphates to the slag phase is the only possible mechanism of refining in my experiments and this effect is enhanced by the presence of big amounts of lime. Moreover, some sort of segregation of carbon was observed at the interface between slag and metal (not totally accurate due to the carbon coating), and this kind of explains the decrease in carbon content in the metal which is either by reaction with oxygen or by reducing iron oxide in the slag to release CO.

In the end, it is worth mentioning that these images only show small areas of the sample and might be only representing the local distribution and hence general conclusions have not been made.

7 Conclusion

Two types of Fe-P alloy were smelted during the thesis work. The use of two different types of iron-phosphide lead to different results, especially in the case of industrial iron-phosphide where the levels of phosphorus was not increased as expected and segregation was observed.

- For future work, the use of pure iron phosphide is recommended since it leads to predictable and consistent results.

In set A of experiments, different binary and ternary slag systems were studied on pure iron alloy (alloy A). It was concluded that:

- The use of metal:slag ratio of 2.5:1 was the best in this work, since the slag will cover the whole area of the metal and will lead to more consistent results
- Higher Fe_2O_3 content led to high Fe loss to the slag , an expected result of having a reducing medium
- Higher CaO contents lead to a better dephosphorization by lowering the activity of P_2O_5
- Silica additions should be avoided since they adversely affect dephosphorization and should be only used if slags with low melting temperatures are required. In addition, when silicate slags were used carbon content in the metal was reduced.
- The best dephosphorization was observed in experiment 9 with a slag containing 50wt% FeO, 45wt% CaO and 5wt% SiO_2. Up to 99% of the initial amount of phosphorus was removed.

In set B, dephosphorization was studied in alloy B using the slag composition from experiment 9. The results obtained were not expected and led to the following conclusions:

- Impurities in the iron, mainly carbon and silicon, will affect drastically the refining process. However, the exact mechanism is still unclear and needs further investigation.
- Slag and metal were extremely mixed and porous. As a result, analysis on the iron was difficult.
- The physical appearance of the samples changed after being left a couple of days in the air, where the slag disintegrated.
- No decisive conclusion can be made on the extent of dephosphorization in these experiments, nor on the effect of refining time and temperature.

The XRD and EPMA analysis agree with each other and with the observations from the literature.

- In the case of binary CaO-FeO slags, the main species were wustite and calcium ferrites
- In case of ternary silicate slags, silicate compounds were observed, e.g. kirschsteinite ($CaFe^{+2}(SiO_4)$) and kilchoanite ($Ca_6.SiO_4.Si_3O_{10}$)

- The presence of portlandite ($Ca(OH)_2$) due to the reaction between calcium containing species and water/moisture can be the reason behind the disintegration of the slag observed in Set B of experiments.
- EPMA quantitative imaging showed that the majority of the phosphorus will be present in the slag phase.

8 Future work

Even if this project work reached many important conclusion, complete understanding of the dephosphorization process requires more investigation and experiments. The next step would be a more in depth study on the effect of impurities. The following suggestions are a possible start.

- Smelt new type of alloys, with different carbon levels and/or silicon, which will be used in the refining experiments. The influence of carbon and silicon on the dephosphorization process can then be unveiled.
- Carry out EPMA analysis on a larger set of samples, which will provide valuable input for improvement in the refining process.
- Carry out more experiments to study the effect of refining time and temperature.
- Study rephosphirization reaction by using P_2O_5-containing slags, and hence shedding light on the phosphate capacities of the different slags used in this study.

Lastly, it is very important to understand the kinetics of dephosphorization and hence a new experimental protocol should be applied. One suggestion is to increase the samples size and find a way to take out small amounts of metal and slag at fixed time intervals and analyzing them.

Bibliography

[1] Zikeev, V. N., Gulyaev, A. P., & Marchenko, V. A. (1973). Effect of Phosphorus on the Properties of Structural Steels. *Translated from Metallovedenie i Termicheskaya Obrabotka Metallov*, 9-12.

[2] Oberg, E. ,et al. (1996). *Machinery's Handbook (25th ed.)*. Industrial Press Inc.

[3] Hou, Y., Qing, S., Wang, H., Shi, Z., & Li, H. (2012). Mixture of Ilmenite and High Phosphorus Iron Ore Smelted by Oxygen-Enriched Top-Blown Smelting Reduction. *J. Cent. South Univ.*, 2760−2767.

[4] Swaren, S. B., & Ram, S. (2013). Removal of Phosphorous from Steel Produced by Melting Sponge Iron in Induction Furnace. *Trans Indian Inst Met*, 207-211.

[5] Jin, Y., Jiang, T., Yang, Y., Li, Q., Li, G., & Guo, Y. (2006). Removal of Phosphorus from Iron Ores by Chemical Leaching. *J. Cent. South Univ. Technol.*, 673-677.

[6] Mamoun, M., & Yu, Z. (1989). A Hydrometallurgical Process for the Dephosphorization of Iron Ore. *Hydrometallurgy*, 277-292.

[7] Delvasto, P., Ballester, A., Muñoz, J., González, F., Blázquez, M., Igual, J., . . . García-Balboa, C. (2009). Mobilization of Phosphorus from Iron Ore by the Bacterium Burkholderia Caribensis FeGL03. *Minerals Engineering*, 1-9.

[8] Fruehan, R. J. (1990). *Vacuum Degassing of Steel.* Iron and Steel Society.

[9] Kenji, A., & Seiichi, T. (1999). Ultra-Purification of Iron by Ultra-High Vacuum Melting. *Vacuum*, 93-96.

[10] Solheim, J. J. (1988). The Tyssedal Ilmenite Smelting Process. *Proceedings on the Norwegian Conference on Ilmenite Smelter*, (pp. 177-199).

[11] *Grande Côte Mineral Sands Project*. (2014). Retrieved from TiZir Limited: http://www.tizir.co.uk/projects-operations/grande-cote-mineral-sands/

[12] Rosenqvist, T. (2004). *Principles of Extractive Metallurgy*. Tapir academic press.

[13] Oeters, F. (1994). *Metallurgy of Steelmaking*. (P. Knighton, Trans.) Düsseldorf: Verlag Stahleisen mbH.

[14] Herasymenko, P. (1938). Electrochemical Theory of Slag-Metal Equilibria Part I. *Trans. Farad. Soc*(34), 1245.

[15] Bockris, J. O., Mackenzie, J. D., & Kitchener, J. A. (1955). Viscous Flow in Silica and Binary Liquid Silicates. *Trans. Farad. Soc.*(51), 1734-1748.

[16] Richardson, F. D., & Elliott, J. F. (1956). *The Physical Chemistry of Steelmaking. Proc. Conf.* Cambridge Massachusetts.

[17] Masson, C. R. (1972). Thermodynamics and Constitution of Silicate Slags. *J. Iron Steel Inst.*(210), 89-96.

[18] Frohberg, M. G., & Kapoor, M. L. (1970). Die elektrolytische Dissoziation flüssiger Schlacken und ihre Bedeutung für metallurgische Reaktionen. *Arch. Eisenhüttenwes.*(41), 209-212.

[19] Basu, S., & Lahiri, A. K. (2013). Production of Low-P steel. *Trans Indian Inst Met*, 555-559.

[20] Bardenheuer , F., vom Ende, H., & Speith, K. G. (1970). *Blast Furn Steel Plant58*, 401.

[21] Turkdogan, E. T. (1984). Physicochemical Aspects of Reactions in Ironmaking and Steelmaking Processes. *Trans ISIJ, 24*, 591.

[22] Basu, S., Seetharaman, S., & Lahiri, A. K. (2010). Thermodynamics of Phosphorus and Sulphur Removal during Basic Oxygen Steelmaking. *Steel Res Int, 81*, 932-939.

[23] Darken, L. S., & Gurry, R. W. (1946). The System Iron Oxygen II. Equilbrium and Thermodynamics of Liquid Oxide and Other Phases. *J. Chem. Soc.*(A68), 798-816.

[24] Distin, P. A., Whiteway, S. G., & Masson, C. R. (1971). Solubility of Oxygen in Liquid Iron from 1785^0C to 1960^0C. A New Technique for the Study of Slag-Metal Equilbria. *Can. Metall. Q.*(10), 13-18.

[25] Turkdogan, E. T. (1980). *Physical Chemistry of High Temperature Technology.* New York: Academic Press.

[26] Verein Deutscher Eisenhüttenleute (ed). (1995). *Slag Atlas.* Düsseldorf: Verlag Stahleisen GmbH.

[27] Fujita, H., Iritani, Y., & Maruhashi, S. (1968). Activities in the Iron-Oxide Lime Slags. *Tetsu To Hagane*(54), 359-370.

[28] Scheel, R. (1974). Untersuchungen zum System Kalk-Eisen-Sauerstoff. *Arch. Eisenhüttenwes*(45), 359-370.

[29] Schürmann, E., & Kraume, G. (1976). Schmelzgleichgewichte im System FeO-Fe2O3-CaO. *Arch. Eisenhüttenwes.*(47), 435-439.

[30] Hara, S., Araki, T., & Ogino, K. (1984). Phase Equilbrium Studies in the FeO-Fe2O3-CaO and FeO-Fe2O3-2CaO-SiO2 Systems. *Metall.Soc. Aime*, 441-451.

[31] Valet, P. M., Pluschkell, W., & Engell, H. J. (1975). Gleichgewichte von MgO-FeO-Fe2O3-Mischkristallen mit Sauerstoff. *Arch. Esienhüttenwes.*(46), 383-388.

[32] Oeters, F. (1964). Grundlagen der Frischreaktionen. *Schlackenarbeit*, 159-162.

[33] Janke, D., & Fischer, W. A. (1976). Desoxidationsgleichgewichte von Titan, Aluminium und Zirkonium in Eisenschmelzen bei 1600^0C. *Arch. Eisenhüttenwes., 47*, 195-198.

[34] Riboud, P. V., Gaye, H., & Grosjean, H. C. (1978). Estimation de l'equilbre metal-laitiers basiques d'aciérie. Application à l'étude des performances des réacteurs industriels. *Physico-Chimie en Sidérurgie, 4*(Communication C2).

[35] Hammerschmid, P., Janke, D., Kreutzer, H. W., Reichenstein, E., & Steffen, R. (1985). Metallurgie und Verfahrenstechniken der Entphosphorung von Roheisen-und Stahlschmelzen. *Stahl Eisen*(105), 433-442.

[36] Wrampelmeyer, J. C., & Janke, D. (1986). Partition Equilibria of Phosphorus between pure liquid iron and CaO-saturated slags at 1600^0C. *Proc.5th Int. Iron Steel Congr.*, (pp. 653-659). Washington D.C.

[37] Trömel, G., Fix, W., & Bongers, U. (1969). Der Eisenoxydapatit im Zustandsschaubild Fe-FeOn-CaO-P2O5. *Arch. Eisenhüttenwes.*(40), 813-818.

[38] Koch, K., Domröse, W., & Ganzow, J. (1984). Kalkphosphatische Stahlwerksschlacken. In K. Koch, & D. Janke (Eds.), *Schlacken in der Metallurgie* (pp. 207-219). Düsseldorf: Verlag Stahleisen.

[39] Schwerdtfeger, K., & Turkdogan, E. T. (1967). Miscibility Gap in the System Iron Oxide-CaO-P2O5 in Air at 1625^0C. *Trans. Metall. Soc. AIME*(239), 589-590.

[40] Knüppel, H., & Oeters, F. (1961). Das Phosphor-Sauerstoff-Gleichgewicht zwischen flüssigem Eisen und kalkgesättigten Phosphatschlacken. *Stahl Eisen*(81), 1437-1449.

[41] Fischer, W. A., & Ende, H. v. (1952). Die Verteilung des Phosphors zwischen Eisenschmelzen und kalkgesättigten Schlacken für Temperaturen von 1530^0C-1700^0C. *Stahl Eisen*(72), 1398-1408.

[42] Trömel, G., & Oelsen, W. (1955). Die Grenzen der Entphosphorung des Eisens mit Kalk. *Arch. Eisenhüttenwes.*(26), 497-506.

[43] Trömel, G., & Fritze, H. W. (1957). Weitere Untersuchungen über die Entphophorung des Eisens mit kalkreichen Schlacken. *Arch. Eisenhüttwenwes*(28), 489-495.

[44] Trömel, G., & Fritze, H. W. (1959). Gleichgewichte zwischen Eisen und kalkhaltigen Phosphatschlacken. *Arch. Eisenhüttwenwes*(30), 461-472.

[45] Turkdogan, E. T., & Pearson, J. (1953). Activities of Constituents of Iron and Steelmaking Slags.Part I. *J. Iron Steel Inst.*(173), 217-223.

[46] Abel Engh, T. (1992). *Principles of Metal Refining*. New York: Oxford University Press Inc.

[47] Elliott, J. F., Gleiser, M., & Ramakrishna, V. (1963). *Thermochemistry for Steelmaking* (Vol. II). Massachusetts, United States of America: Addison-Wesley Publishing Company, Inc.

A. Temperature curve

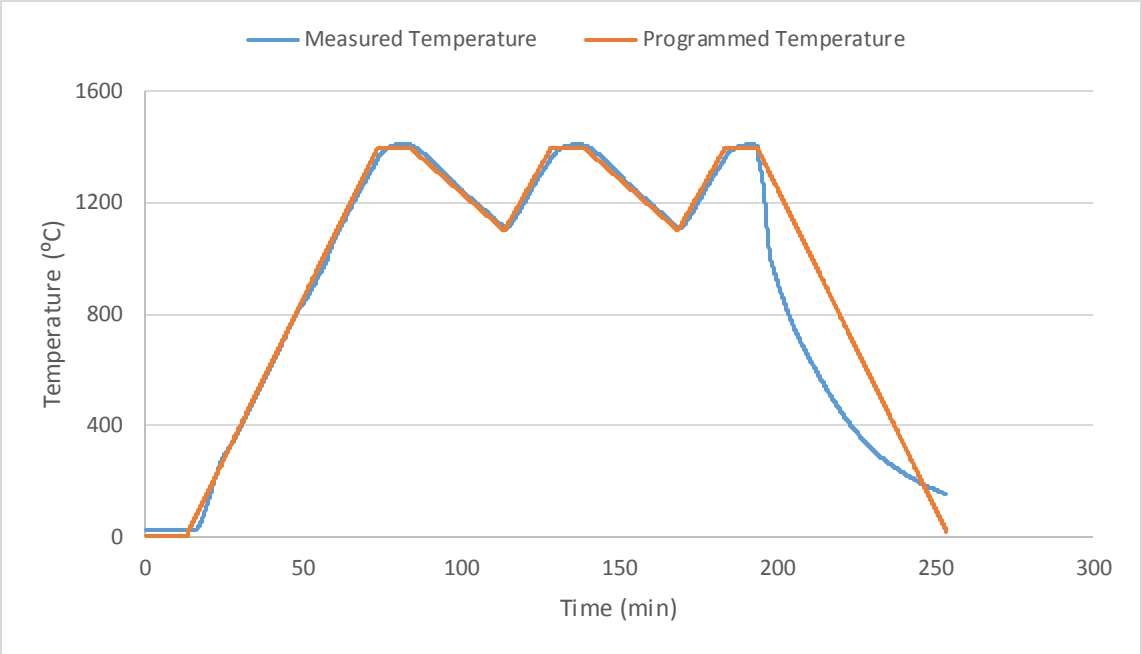

Figure A.1: Temperature curve for the smelting of alloy B

B. Iron analysis

Table B.1: Detailed chemical composition of the different points in Alloy A

Point	Chemical composition (wt%)										
	C	Si	S	P	Mn	Ni	Cr	Mo	V	Cu	Ti
1	0.329	0.000	0.007	0.357	0.000	0.005	0.002	0.002	0.001	0.004	0.000
2	0.330	0.000	0.004	0.249	0.000	0.004	0.001	0.001	0.000	0.003	0.000
3	0.330	0.000	0.006	0.314	0.000	0.004	0.002	0.002	0.000	0.004	0.000
4	0.330	0.000	0.006	0.291	0.000	0.004	0.002	0.002	0.000	0.004	0.000
5	0.330	0.000	0.006	0.297	0.000	0.004	0.002	0.002	0.000	0.003	0.000
6	0.330	0.000	0.004	0.211	0.000	0.004	0.002	0.002	0.000	0.004	0.000
7	0.330	0.000	0.005	0.301	0.000	0.004	0.002	0.002	0.000	0.005	0.000
8	0.330	0.000	0.004	0.265	0.000	0.004	0.002	0.002	0.000	0.005	0.000
9	0.330	0.000	0.005	0.278	0.000	0.005	0.002	0.002	0.000	0.006	0.000

Point	Chemical composition (wt%)(continued)									
	Co	Pb	B	Al	Sb	Sn	W	Zn	Bi	Fe
1	0.002	0.002	0.000	0.002	0.003	0.001	0.000	0.000	0.003	99.280
2	0.002	0.000	0.000	0.001	0.001	0.000	0.000	0.000	0.001	99.400
3	0.002	0.002	0.000	0.002	0.003	0.001	0.000	0.000	0.004	99.330
4	0.002	0.001	0.000	0.002	0.003	0.001	0.000	0.000	0.003	99.350
5	0.002	0.001	0.000	0.002	0.002	0.001	0.000	0.000	0.003	99.350
6	0.002	0.001	0.000	0.002	0.003	0.001	0.000	0.000	0.003	99.430
7	0.002	0.002	0.000	0.002	0.003	0.001	0.000	0.000	0.005	99.340
8	0.002	0.001	0.000	0.002	0.003	0.001	0.000	0.000	0.004	99.380
9	0.002	0.002	0.000	0.002	0.003	0.001	0.000	0.000	0.005	99.360

Table B.2: Detailed chemical composition of the different points in Alloy B

Point	Chemical composition (wt%)										
	C	Si	S	P	Mn	Ni	Cr	Mo	V	Cu	Ti
1	4.005	0.120	0.013	0.060	0.014	0.032	0.028	0.000	0.029	0.000	0.017
2	4.017	0.123	0.013	0.066	0.013	0.033	0.026	0.000	0.027	0.001	0.014
3	3.960	0.130	0.013	0.024	0.011	0.034	0.020	0.000	0.017	0.000	0.008
4		0.134		0.036	0.013	0.034	0.023	0.000	0.020	0.002	0.010
5		0.129		0.039	0.012	0.034	0.023	0.000	0.022	0.000	0.013

Point	Chemical composition (wt%) (continued)	
	Co	Al
1	0.000	0.000
2	0.000	0.000
3	0.000	0.000
4	0.001	0.000
5	0.000	0.000

Table B.3: Detailed chemical composition of the iron in experiments 1-7

Exp.	Pt.	Chemical composition (wt%)										
		C	Si	S	P	Mn	Ni	Cr	Mo	V	Cu	Ti
1	1	0.087	0.000	0.051	0.262	0.000	0.006	0.001	0.001	0.000	0.001	0.000
	2	0.086	0.000	0.007	0.267	0.000	0.007	0.003	0.004	0.001	0.006	0.000
	3		0.000	0.009	0.281	0.000	0.007	0.003	0.004	0.001	0.006	0.000
	4		0.000	0.008	0.320	0.000	0.007	0.003	0.004	0.001	0.006	0.000
2	1	0.316	0.000	0.007	0.010	0.000	0.008	0.003	0.004	0.001	0.007	0.000
	2	0.320	0.000	0.007	0.010	0.000	0.008	0.002	0.003	0.000	0.005	0.000
	3	0.316	0.000	0.006	0.008	0.000	0.007	0.001	0.002	0.000	0.002	0.000
	4		0.000	0.007	0.010	0.000	0.008	0.002	0.031	0.000	0.005	0.000
3	1	0.323	0.000	0.007	0.012	0.000	0.008	0.001	0.001	0.000	0.001	0.000
	2	0.279	0.000	0.006	0.009	0.000	0.007	0.001	0.001	0.000	0.001	0.000
	3	0.271	0.000	0.007	0.011	0.000	0.008	0.002	0.033	0.000	0.005	0.000
	4		0.000	0.007	0.012	0.000	0.008	0.003	0.003	0.000	0.004	0.000
4	1	0.304	0.000	0.055	0.005	0.000	0.007	0.001	0.001	0.000	0.001	0.000
	2	0.298	0.000	0.006	0.005	0.000	0.007	0.001	0.001	0.000	0.002	0.000
	3	0.300	0.000	0.006	0.006	0.000	0.008	0.003	0.004	0.000	0.006	0.000
	4		0.000	0.006	0.006	0.000	0.007	0.002	0.003	0.003	0.005	0.000
5	1	0.308	0.000	0.007	0.006	0.002	0.008	0.003	0.004	0.001	0.022	0.000
	2	0.293	0.000	0.006	0.006	0.000	0.007	0.001	0.001	0.000	0.002	0.000
	3	0.309	0.000	0.007	0.006	0.000	0.008	0.003	0.004	0.005	0.006	0.000
	4		0.000	0.006	0.006	0.002	0.008	0.003	0.004	0.001	0.008	0.000
6	1	0.313	0.000	0.002	0.003	0.000	0.007	0.002	0.003	0.000	0.003	0.000
	2	0.295	0.000	0.003	0.003	0.000	0.006	0.001	0.002	0.000	0.001	0.000
	3	0.315	0.000	0.004	0.004	0.000	0.007	0.002	0.003	0.000	0.004	0.000
	4		0.000	0.004	0.004	0.000	0.006	0.002	0.002	0.000	0.003	0.000
7	1	0.311	0.000	0.005	0.007	0.000	0.007	0.003	0.004	0.001	0.006	0.000
	2	0.315	0.000	0.005	0.006	0.000	0.007	0.001	0.001	0.000	0.001	0.000
	3		0.000	0.005	0.006	0.000	0.007	0.001	0.001	0.000	0.002	0.000
	4		0.000	0.005	0.007	0.000	0.007	0.002	0.003	0.000	0.005	0.000

Table B.4: Detailed chemical composition of the iron in experiments 8-9

Exp.	Pt.	Chemical composition (wt%)										
		C	Si	S	P	Mn	Ni	Cr	Mo	V	Cu	Ti
8	1	0.006	0.000	0.007	0.016	0.000	0.006	0.001	0.000	0.000	0.000	0.000
	2	0.030	0.000	0.008	0.017	0.000	0.006	0.002	0.002	0.000	0.000	0.000
	3	0.050	0.000	0.009	0.018	0.000	0.006	0.001	0.000	0.000	0.000	0.000
	4		0.000	0.008	0.016	0.000	0.006	0.002	0.001	0.000	0.000	0.000
9	1	0.003	0.000	0.004	0.003	0.000	0.005	0.000	0.000	0.000	0.000	0.000
	2	0.002	0.000	0.003	0.002	0.000	0.005	0.000	0.000	0.000	0.000	0.000
	3	0.040	0.000	0.004	0.003	0.000	0.005	0.001	0.001	0.000	0.000	0.000
	4		0.000	0.004	0.003	0.000	0.005	0.001	0.001	0.000	0.000	0.000

Table B.5: Detailed chemical composition of the iron in experiment 11

Point	Chemical composition (wt%)										
	C	Si	S	P	Mn	Ni	Cr	Mo	V	Cu	Ti
1	2.060	0.000	0.012	0.018	0.011	0.037	0.021	0.000	0.010	0.000	0.000
2	1.930	0.000	0.012	0.021	0.011	0.036	0.023	0.000	0.012	0.000	0.000
3	1.990		0.013								

C. Physical appearance

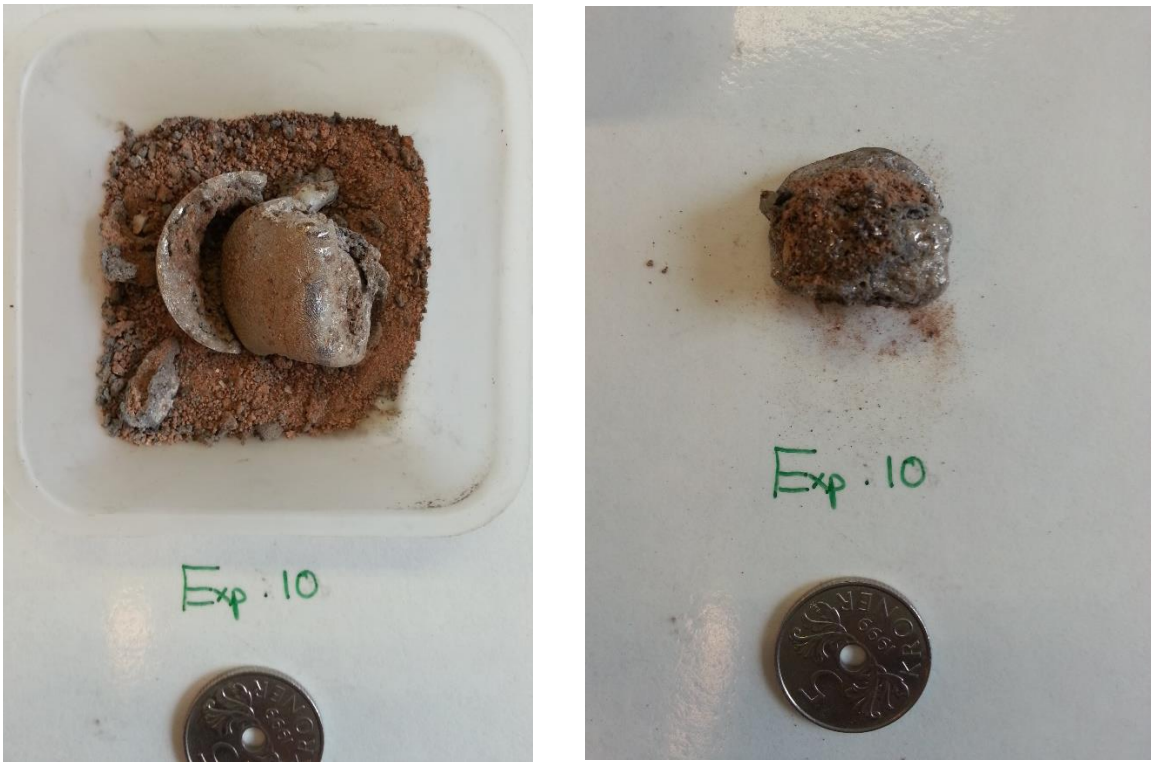

Figure C.1: Physical appearance of the sample from experiment 10

Figure C.2: Physical appearance of the sample from experiment 11

Figure C.3: Physical appearance of the sample from experiment 12

D. XRD

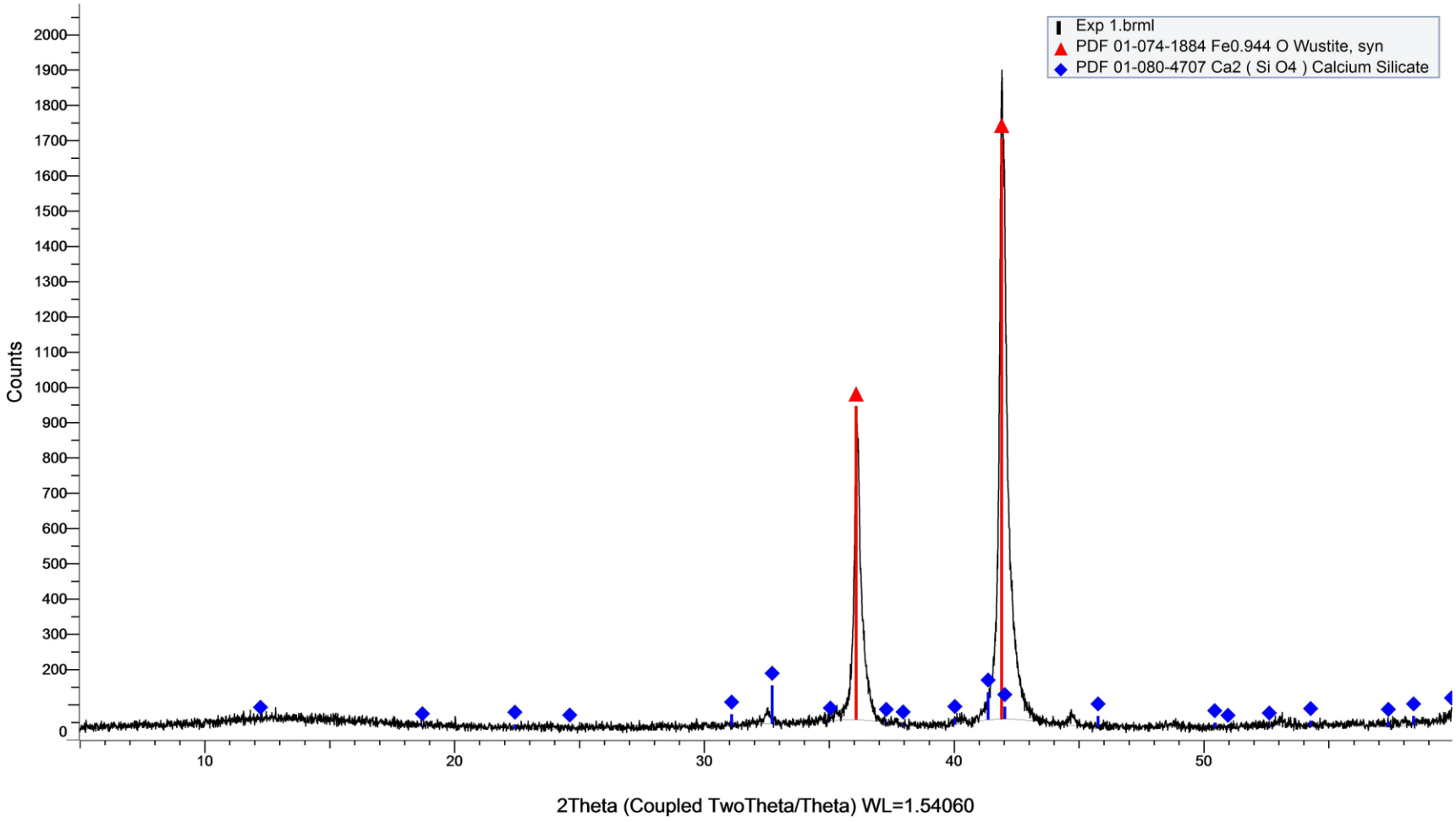

Figure D.1: XRD pattern for experiment 1

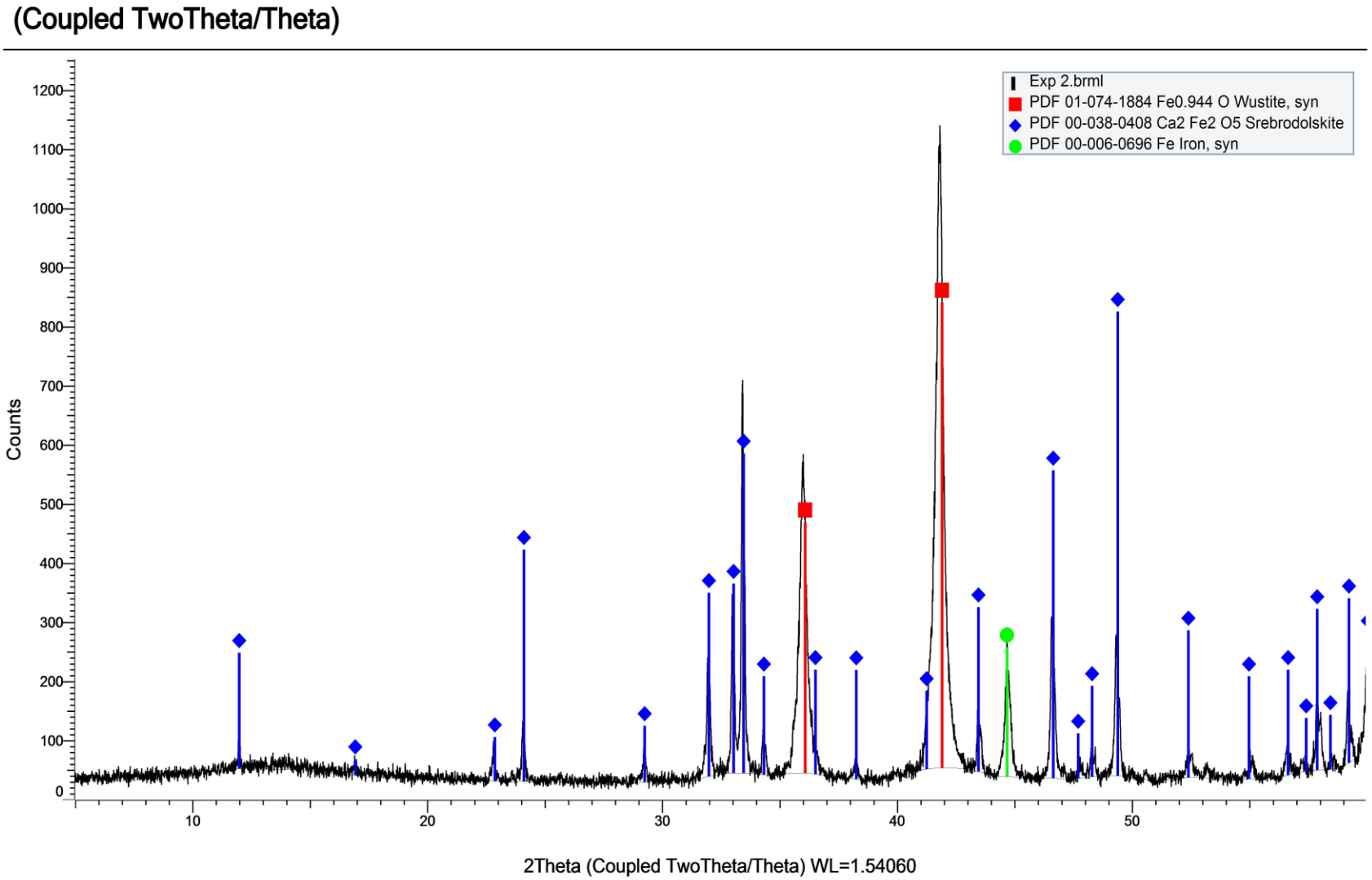

Figure D.2: XRD pattern for experiment 2

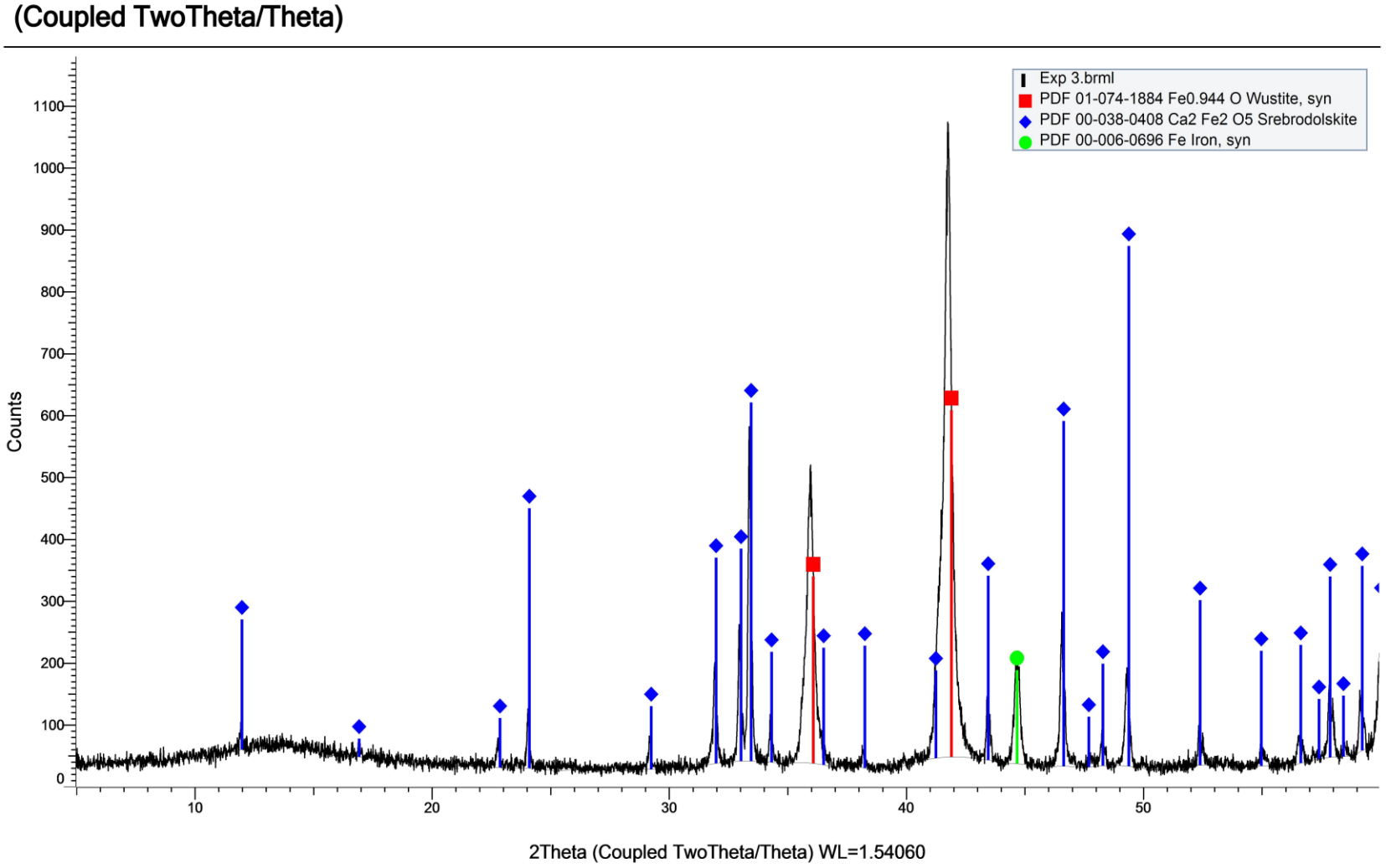

Figure D.3: XRD pattern for experiment 3

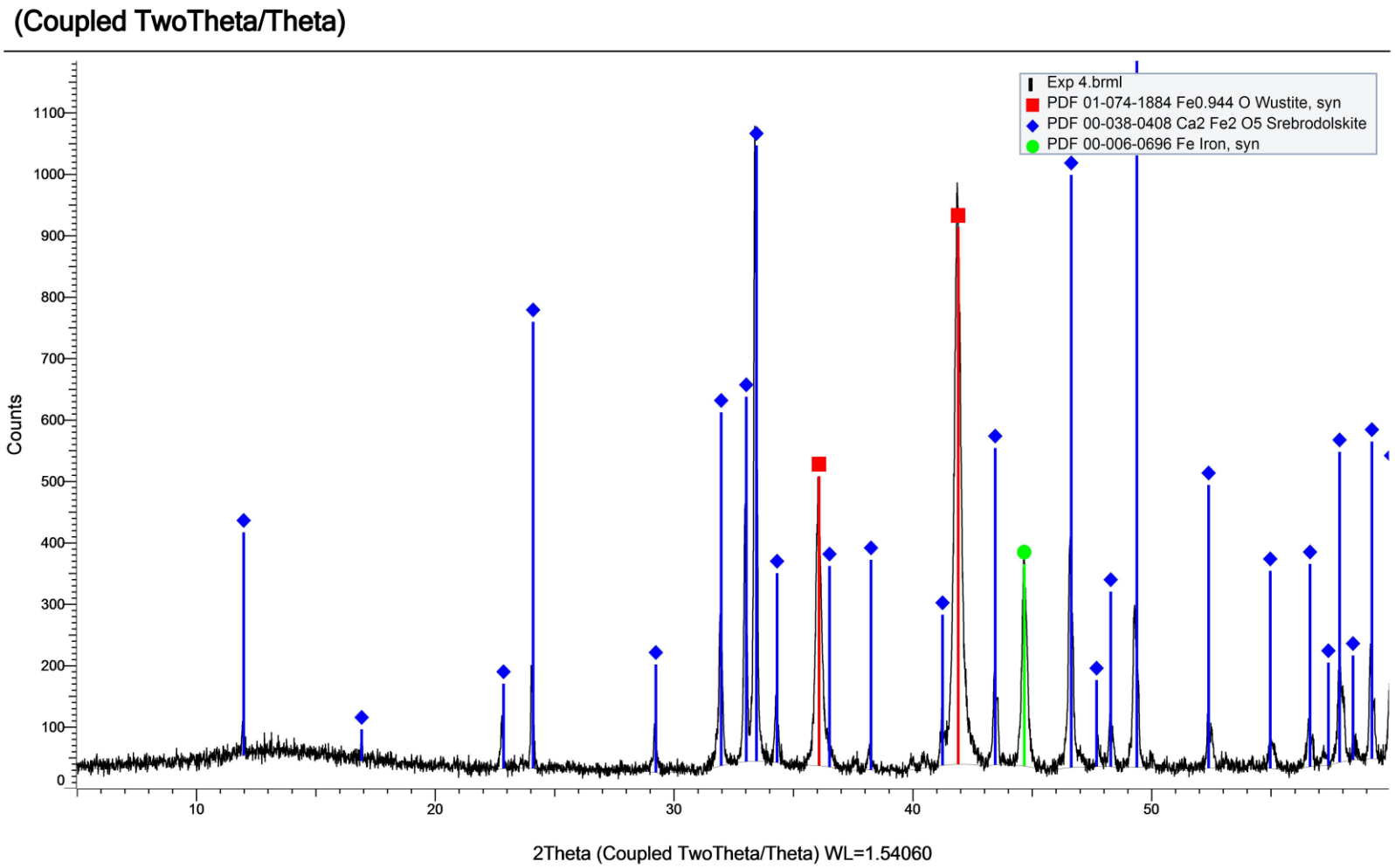

Figure D.4: XRD pattern for experiment 4

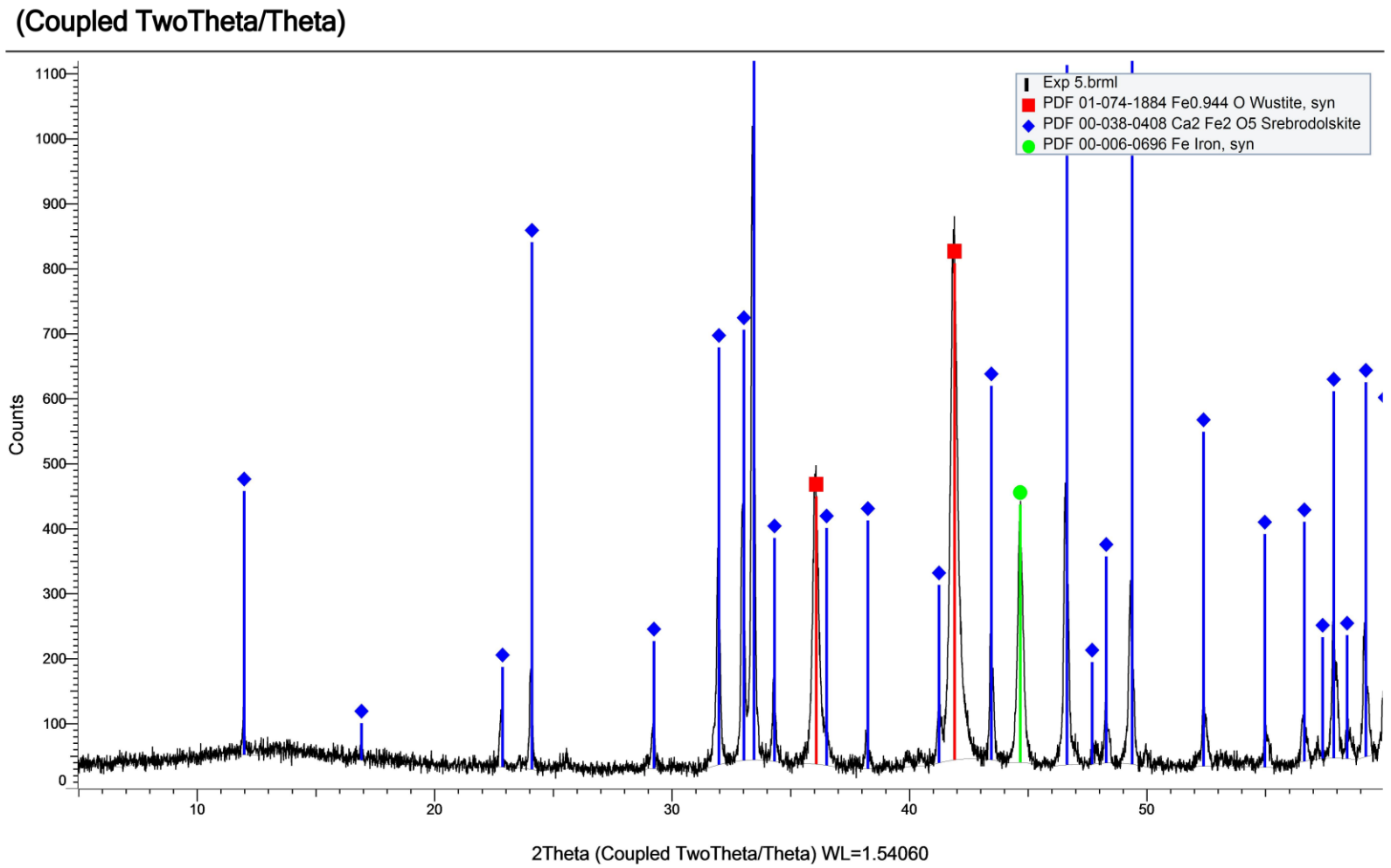

Figure D.5: XRD pattern for experiment 5

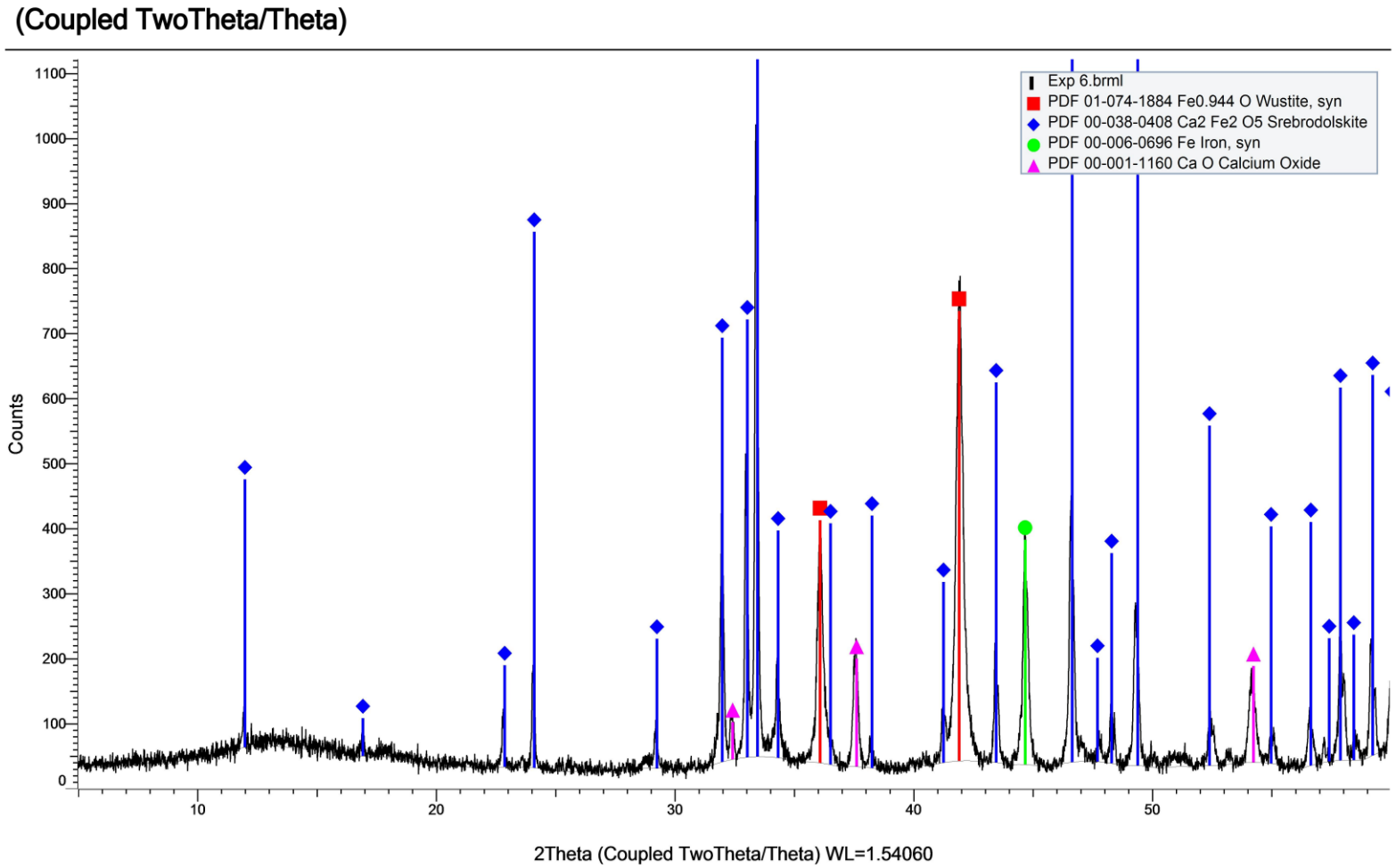

Figure D.6: XRD pattern for experiment 6

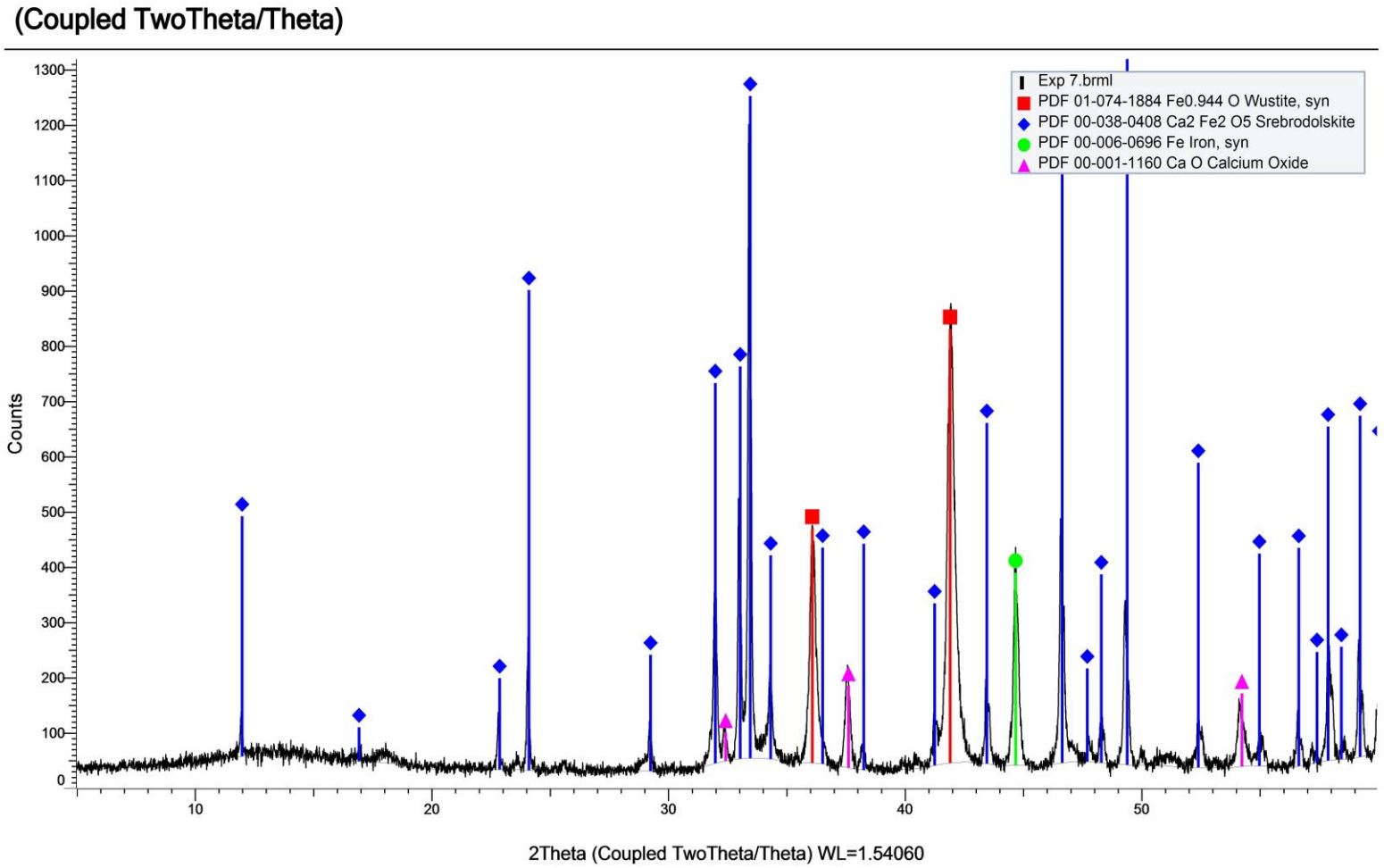

Figure D.7: XRD pattern for experiment 7

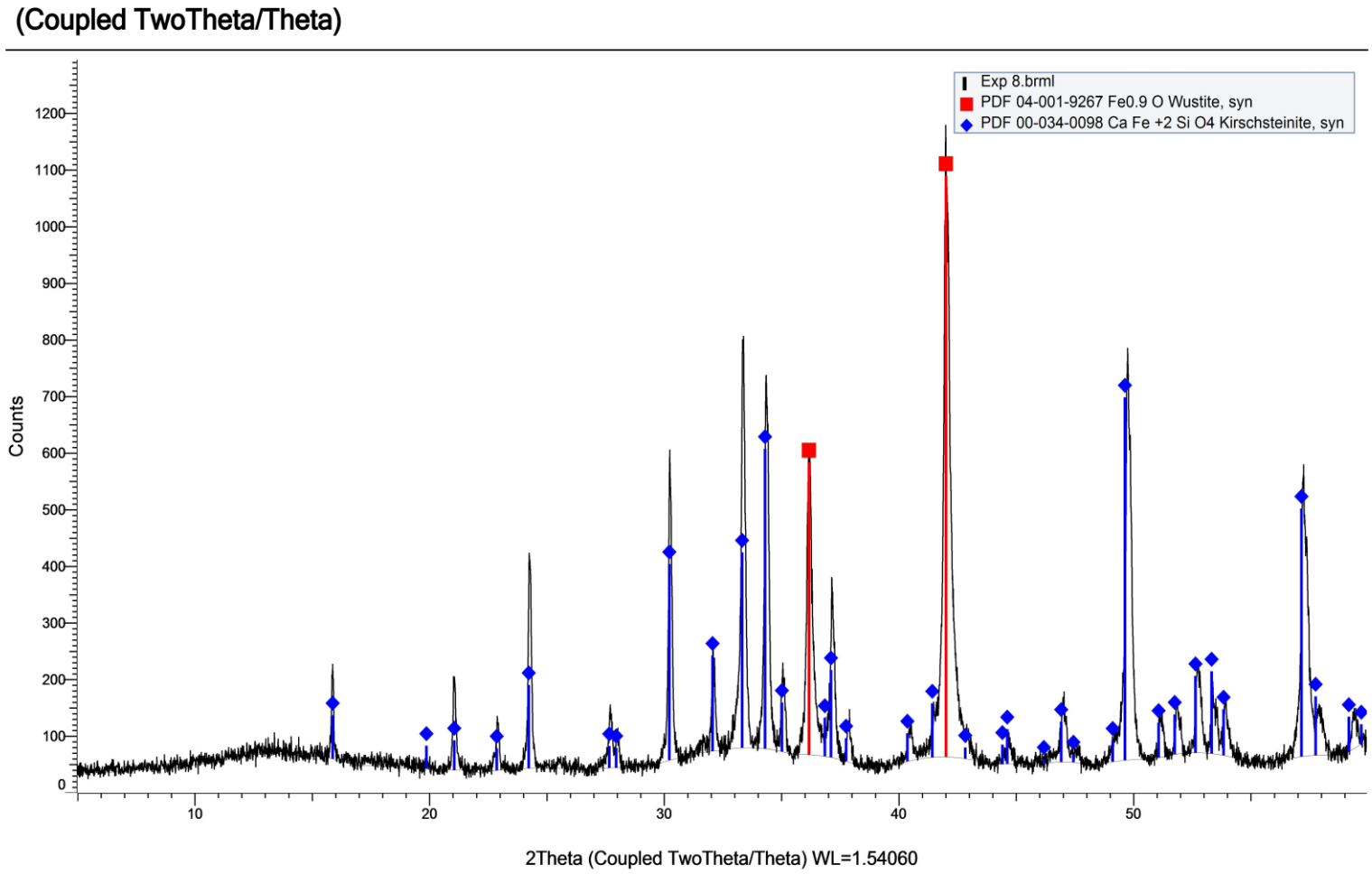

Figure D.8: XRD pattern for experiment 8

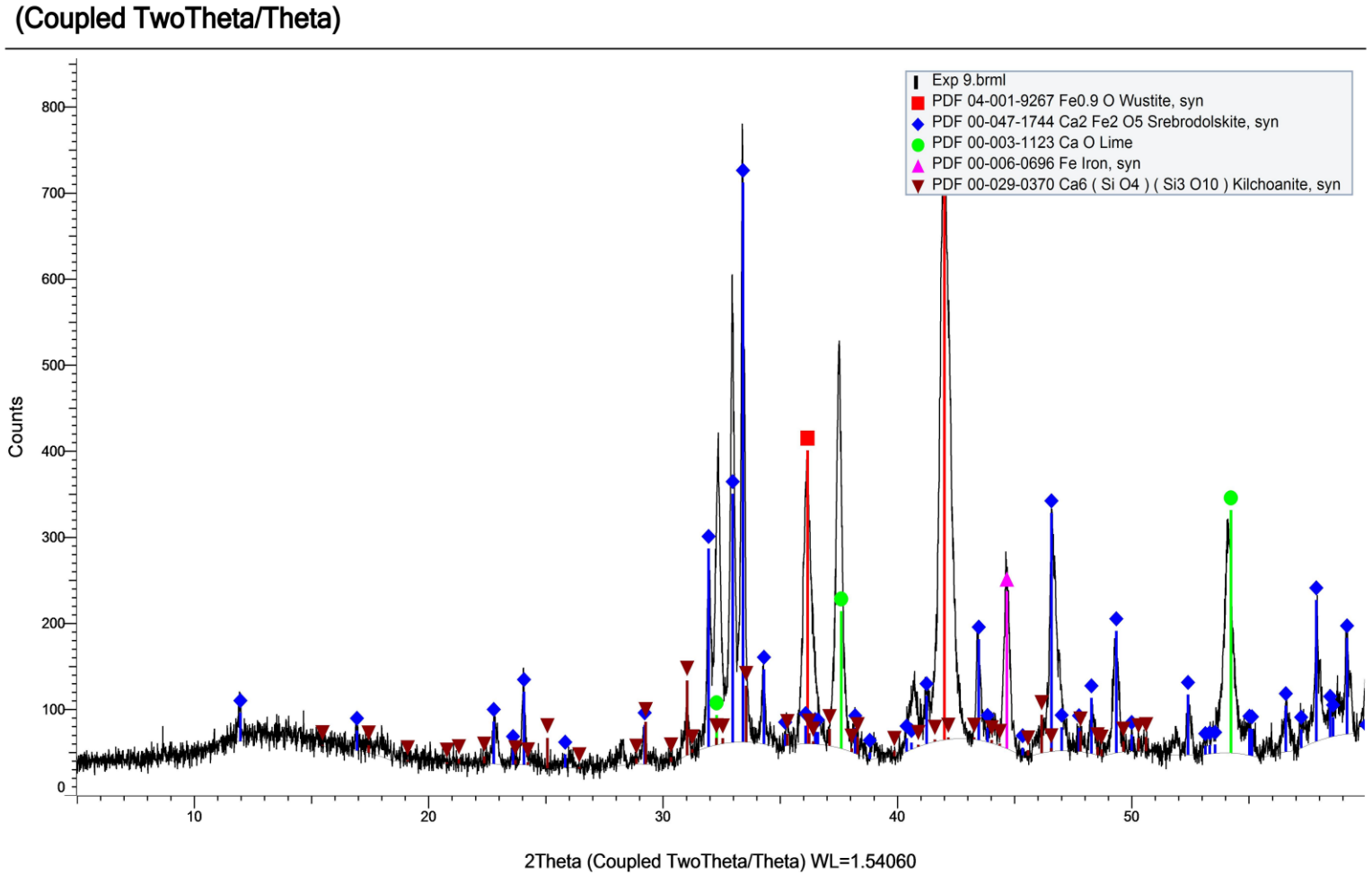

Figure D.9: XRD pattern for experiment 9

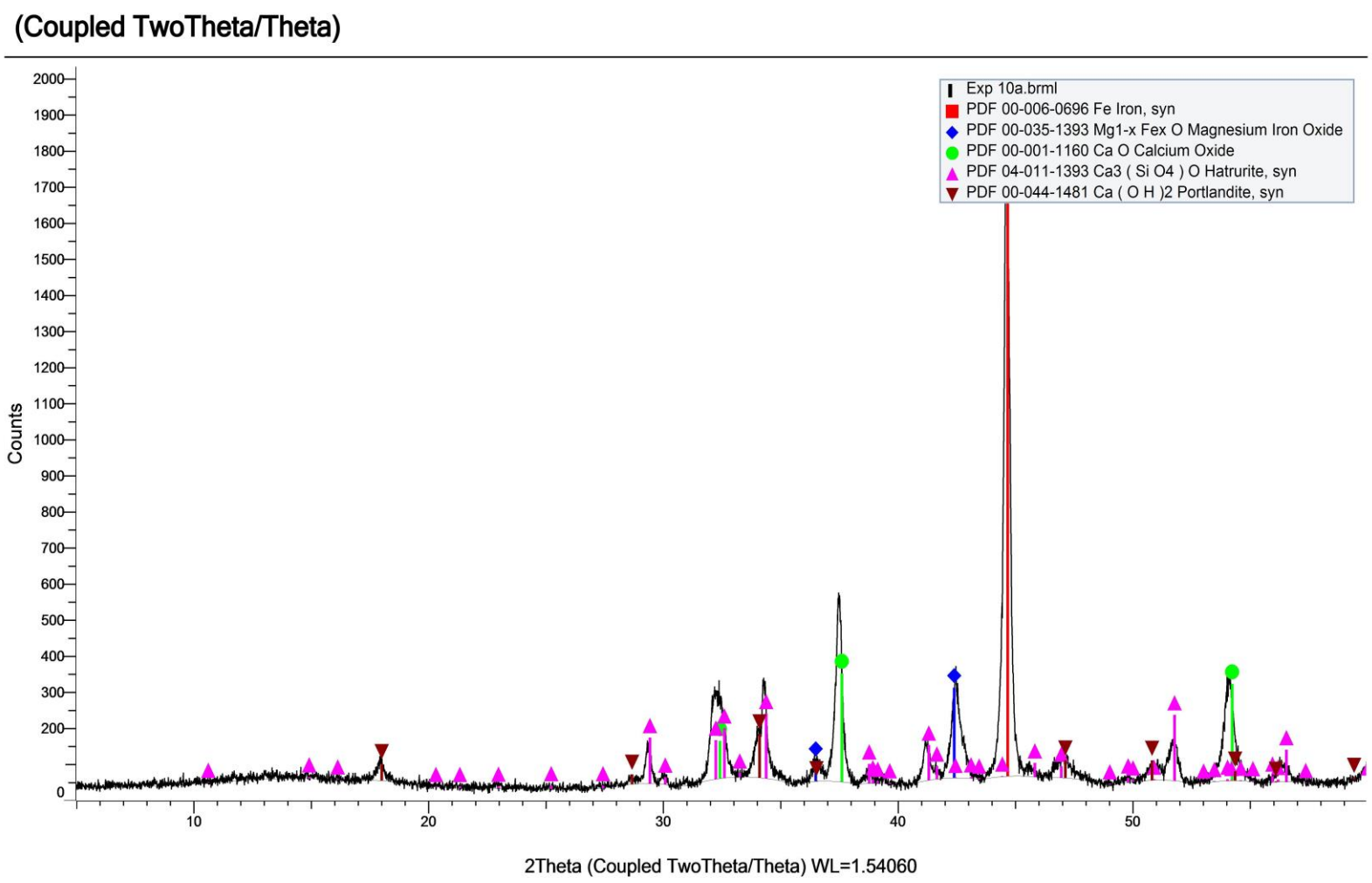

Figure D.10: XRD pattern for experiment 10a

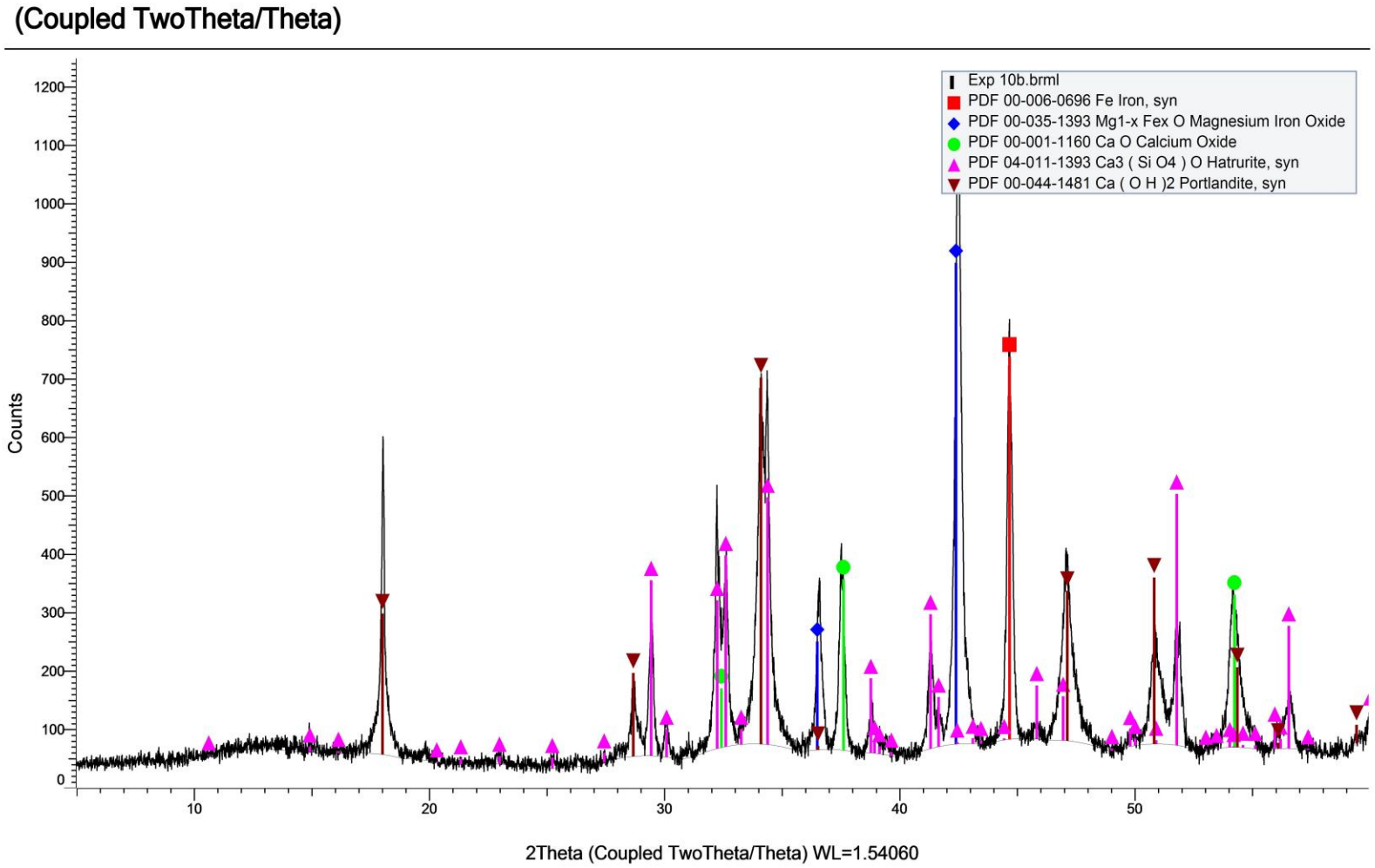

Figure D.11: XRD pattern for experiment 10b

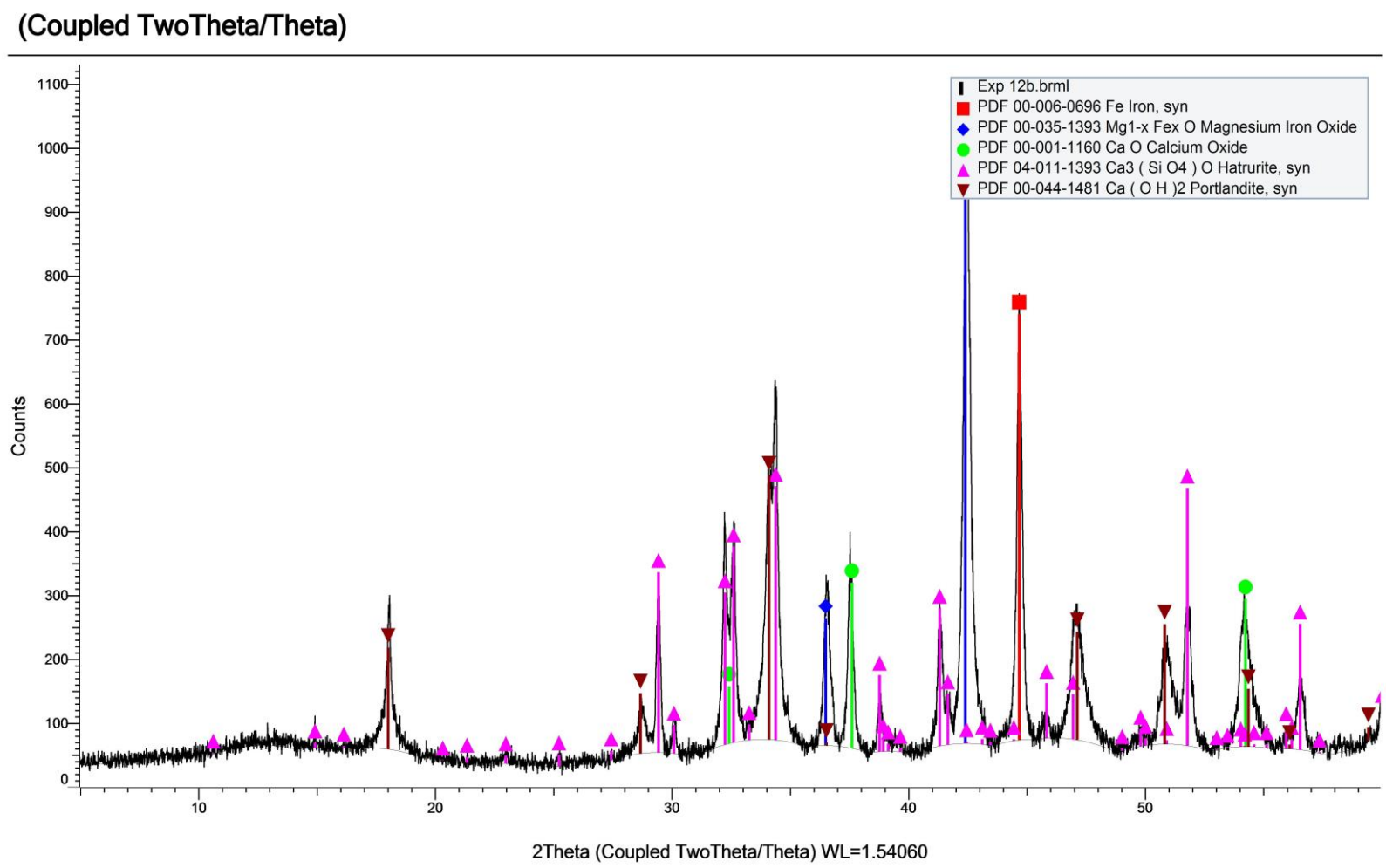

Figure D.12: XRD pattern for experiment 12b

E. EPMA

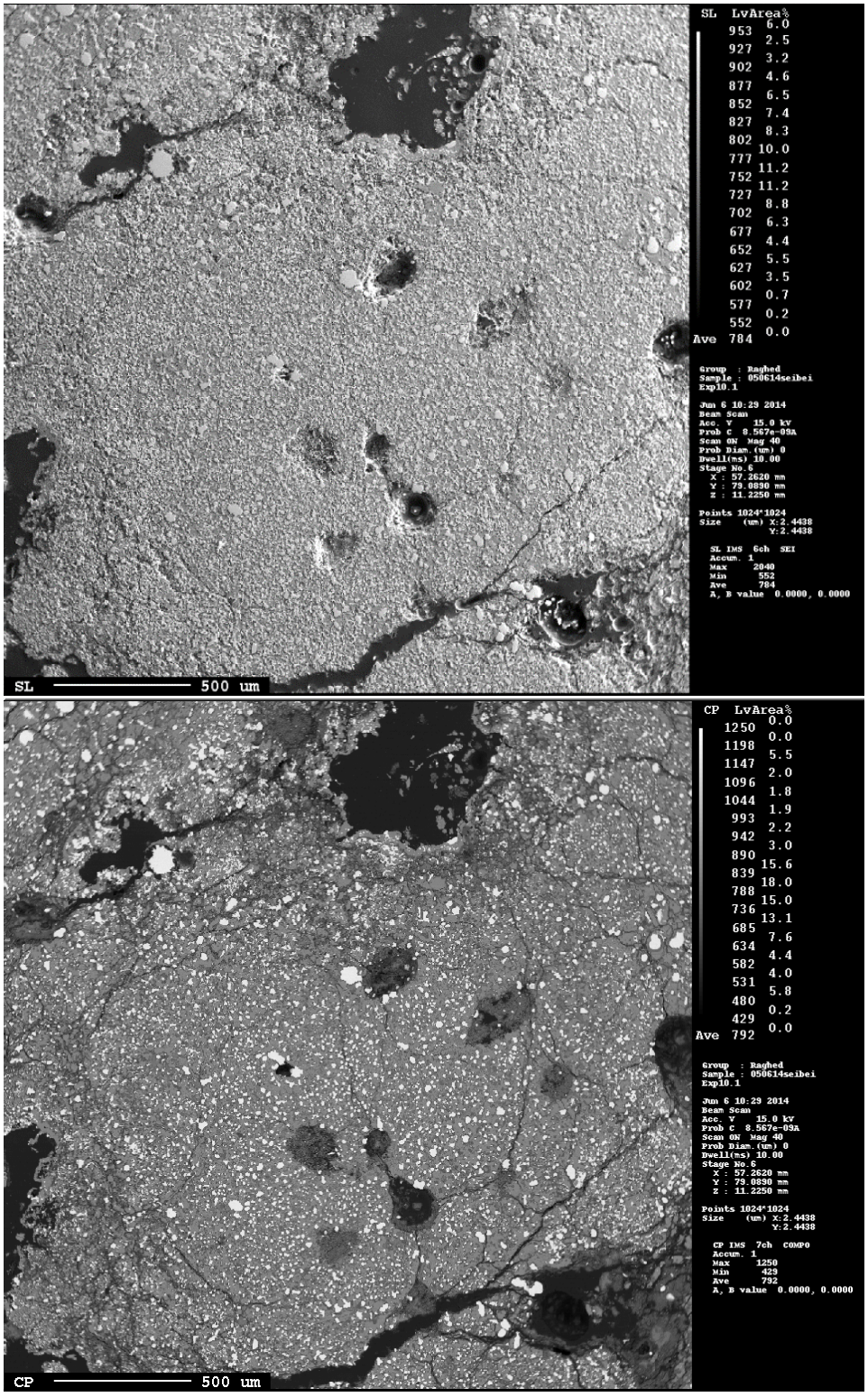

Figure E.1: First EPMA image of experiment 10.1

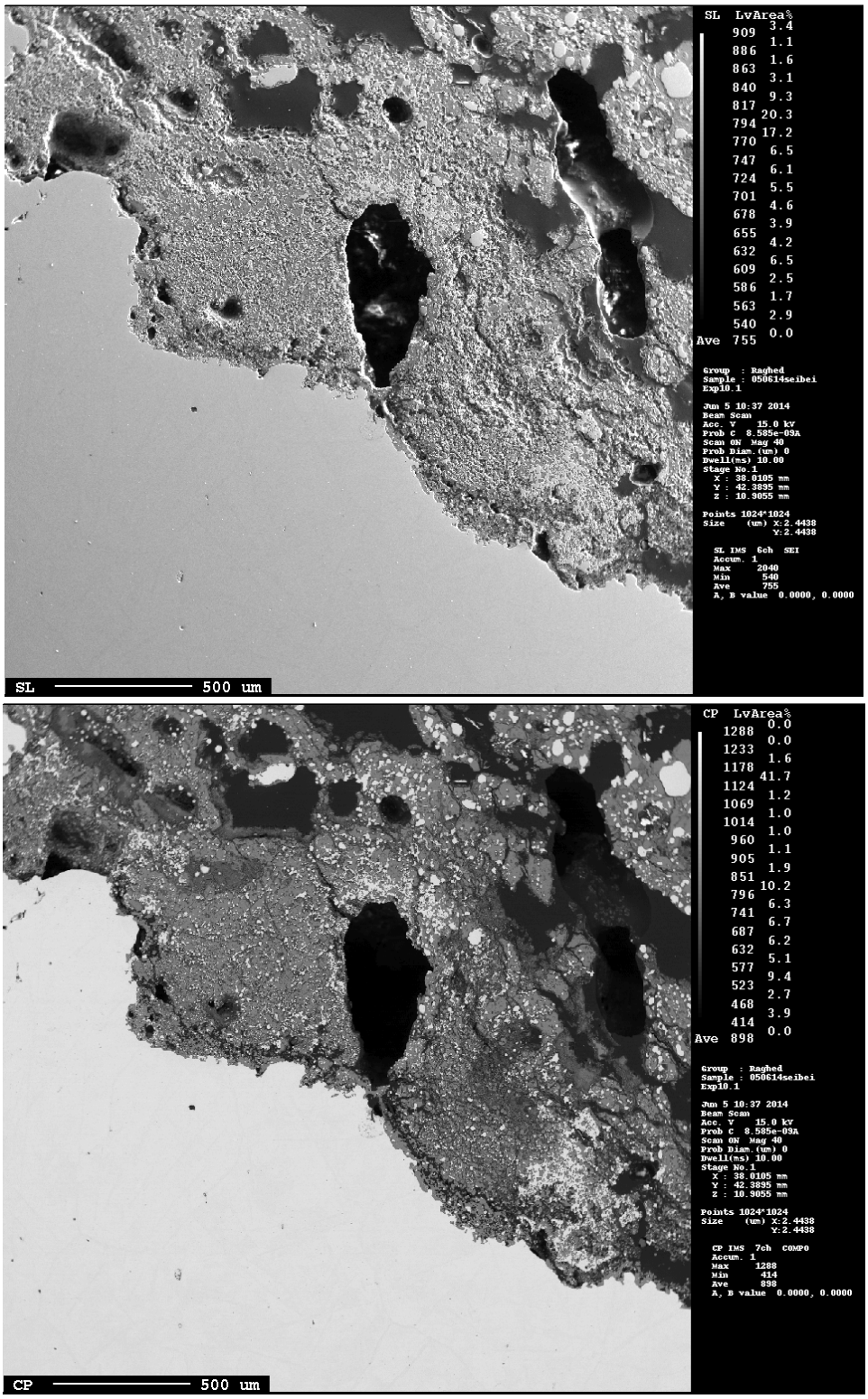

Figure E.2: Second EPMA image of experiment 10.1

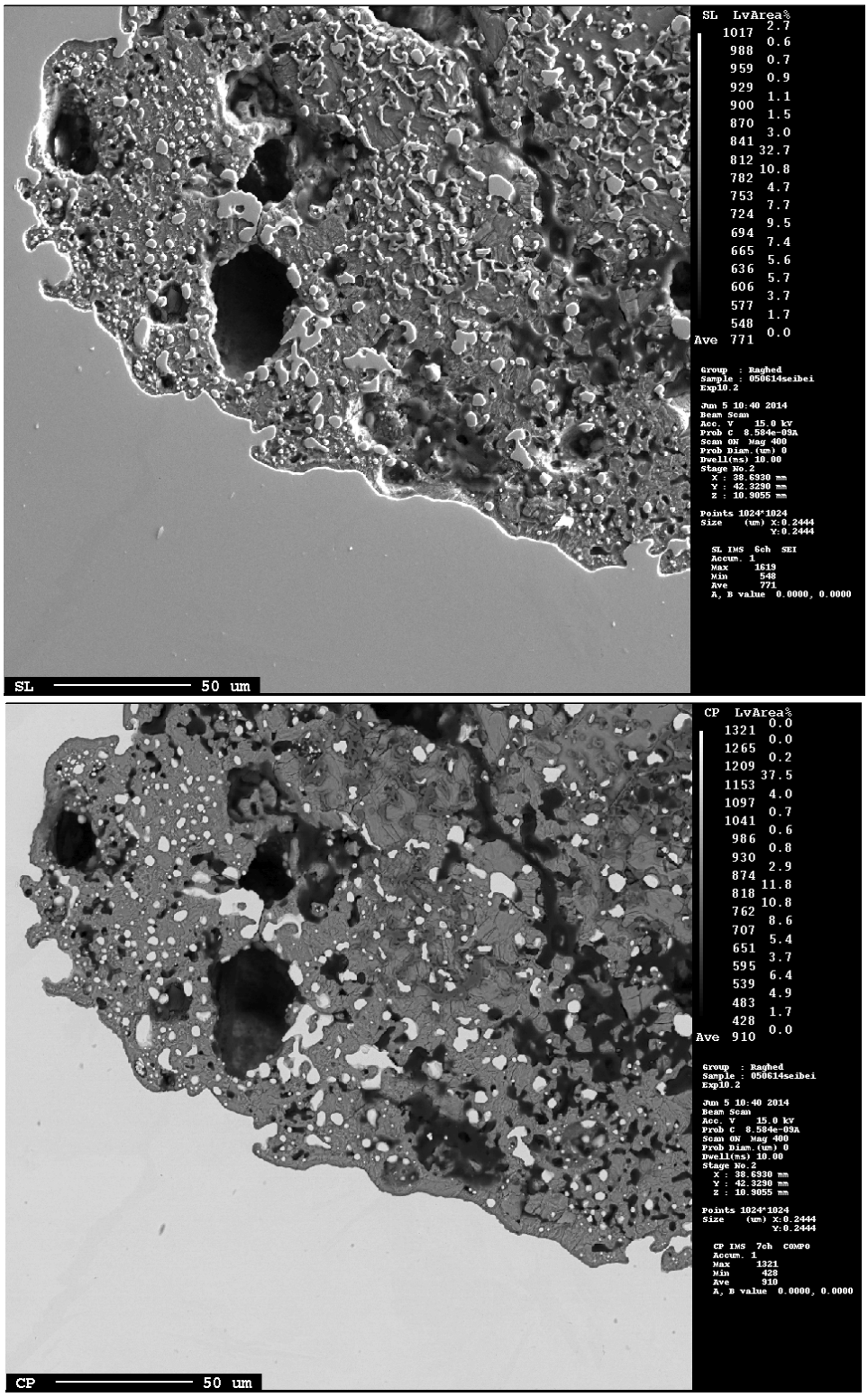

Figure E.3: Third EPMA image of experiment 10.1

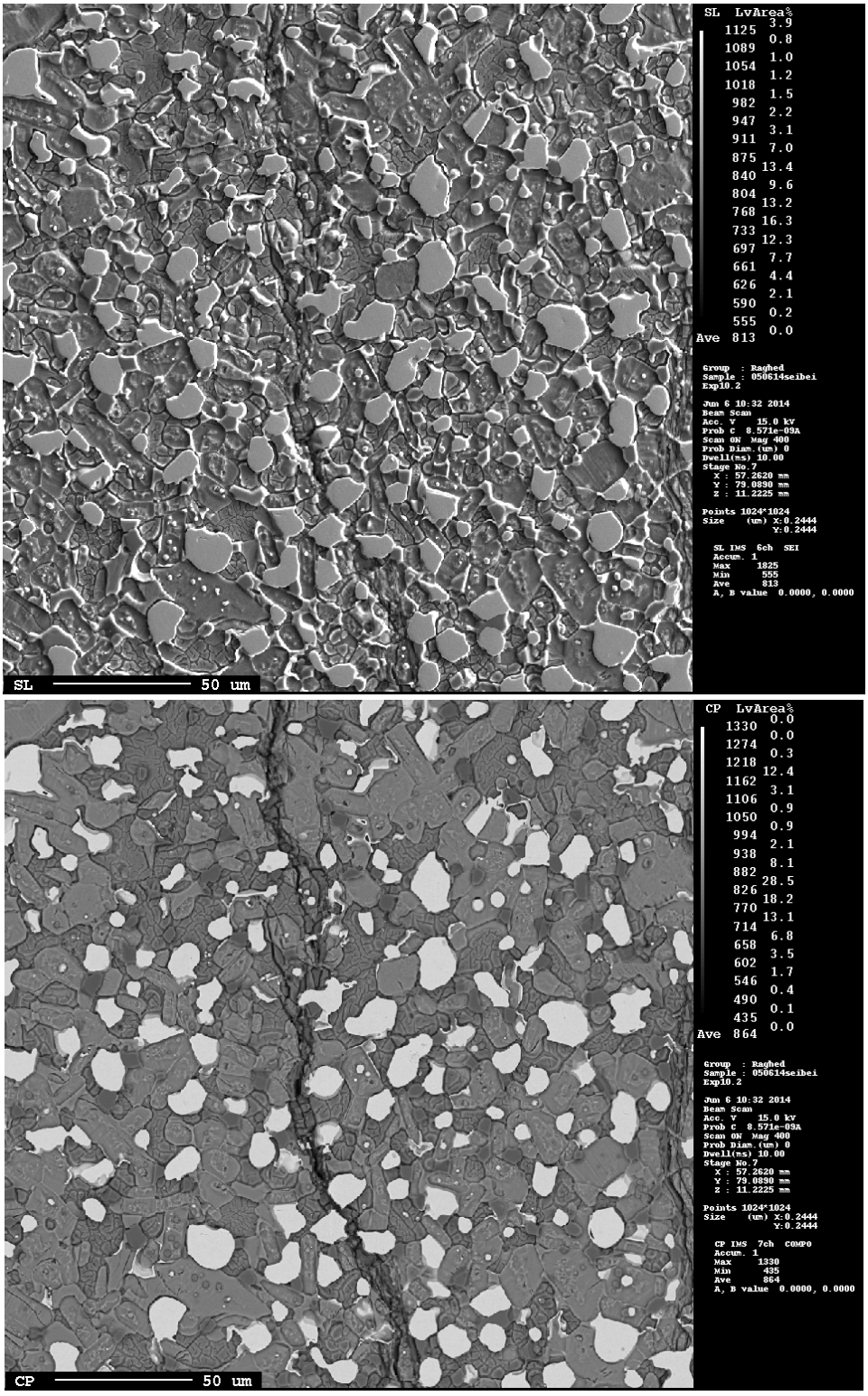

Figure E.4: First EPMA image of experiment 10.2

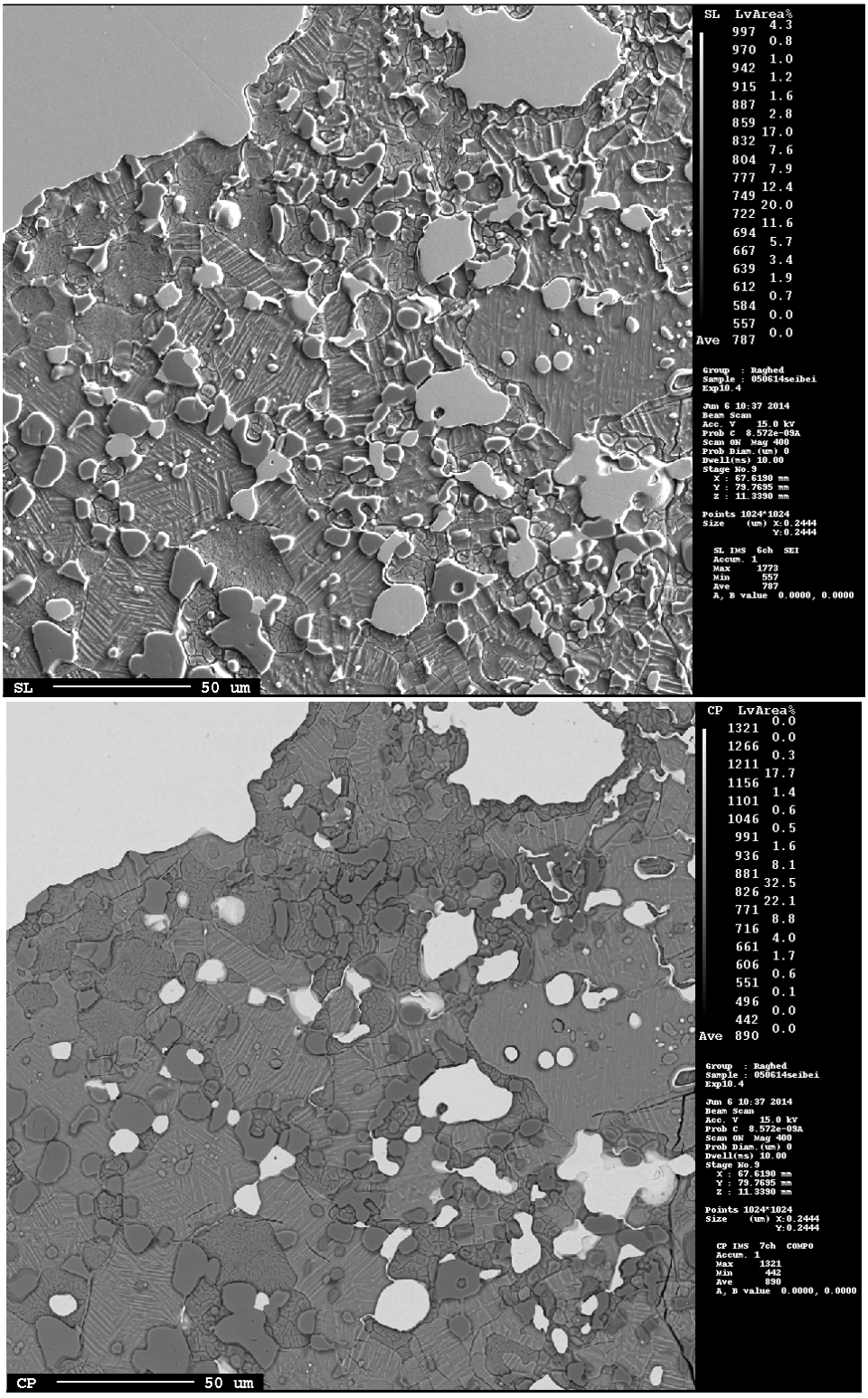

Figure E.5: Second EPMA image of experiment 10.2

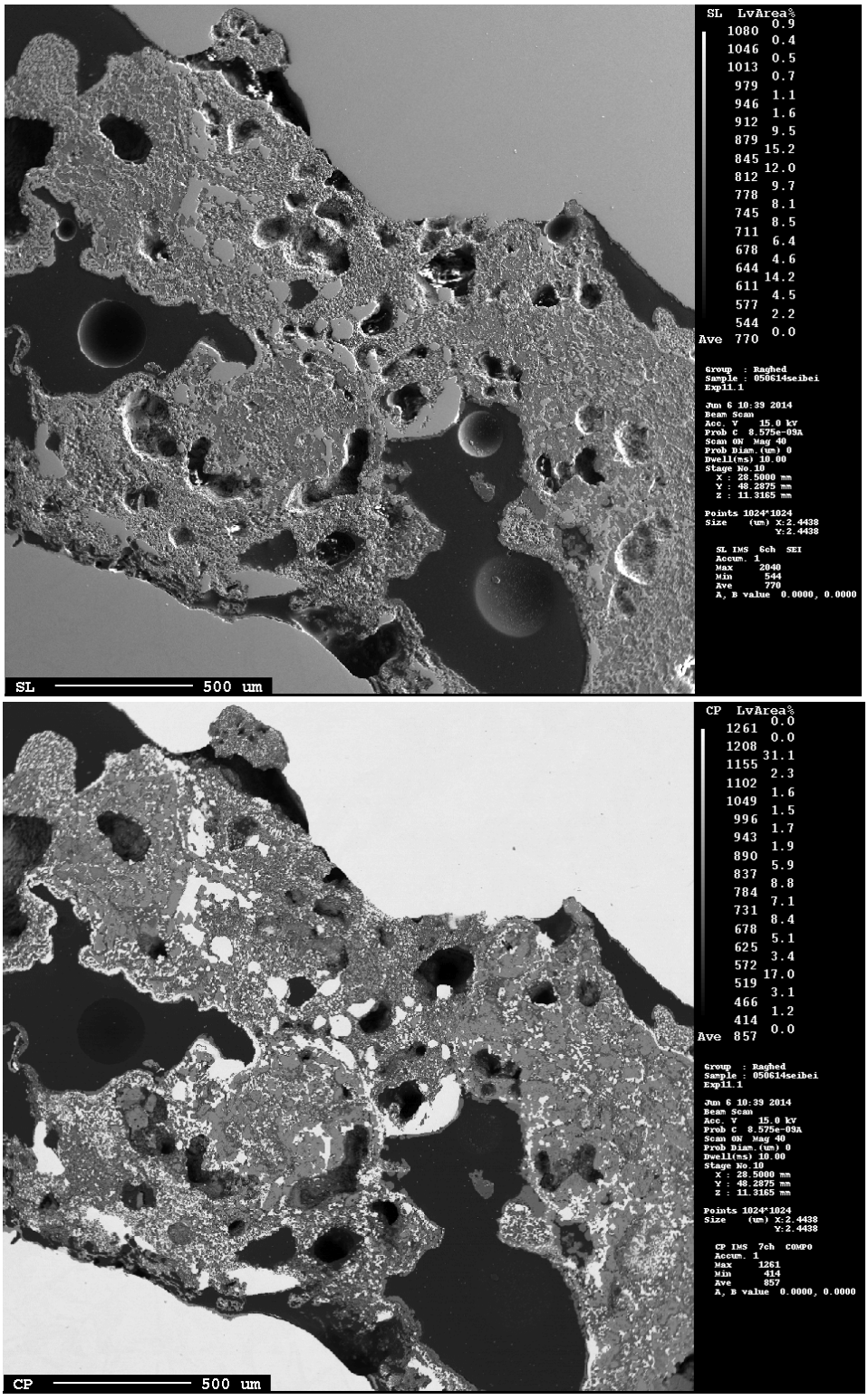

Figure E.6: First EPMA image of experiment 11

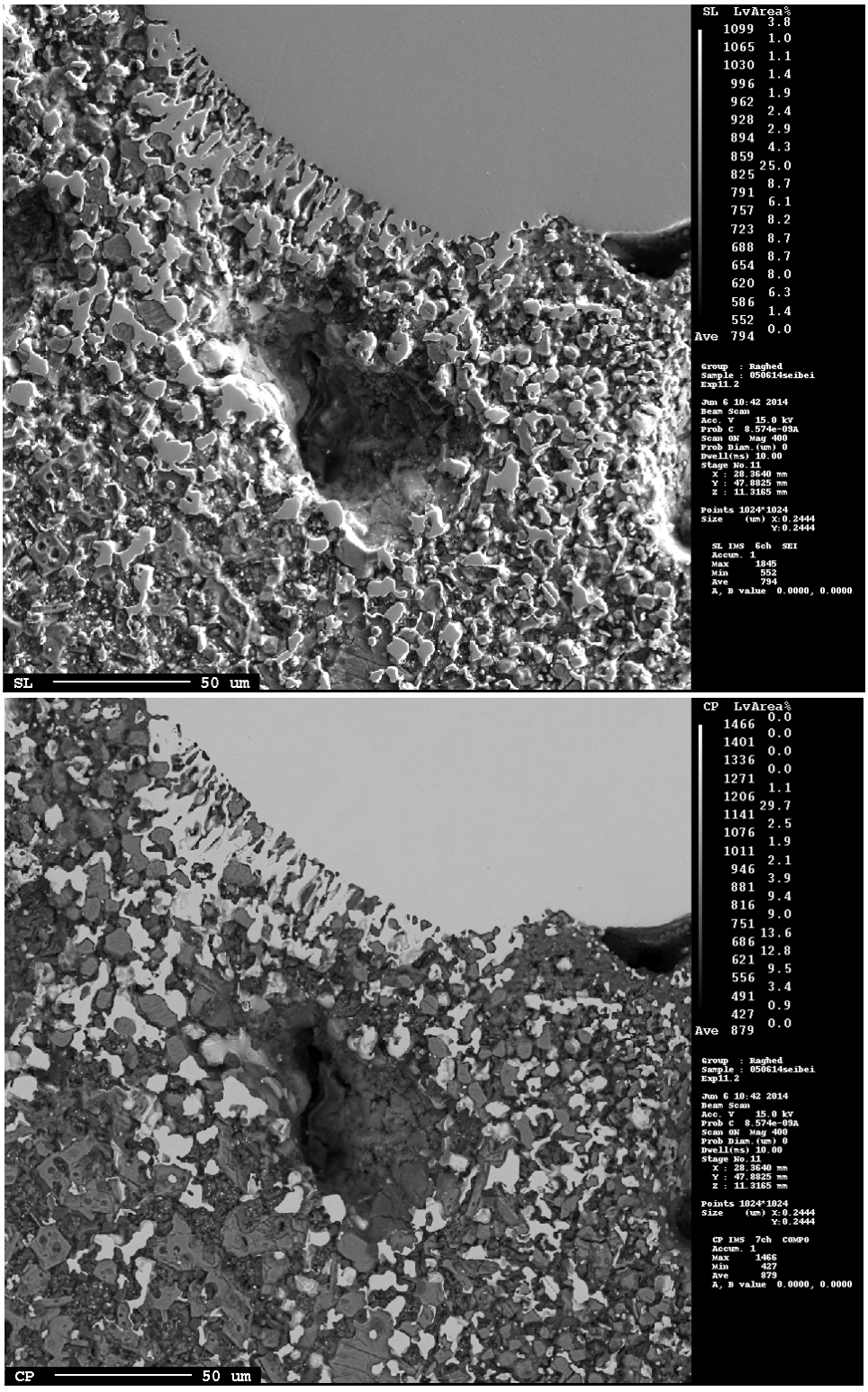

Figure E.7: Second EPMA image of experiment 11

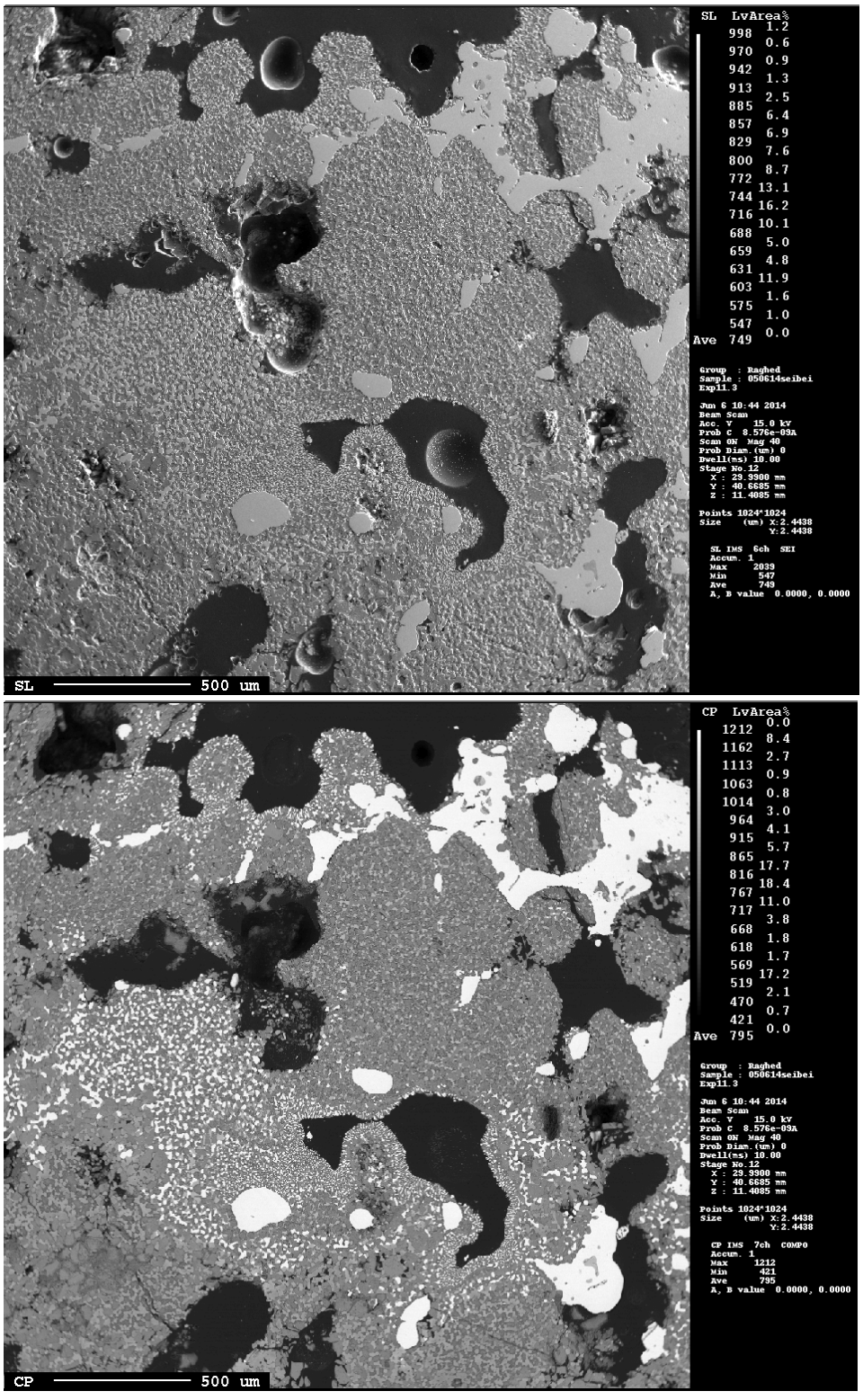

Figure E.8: Third EPMA image of experiment 11

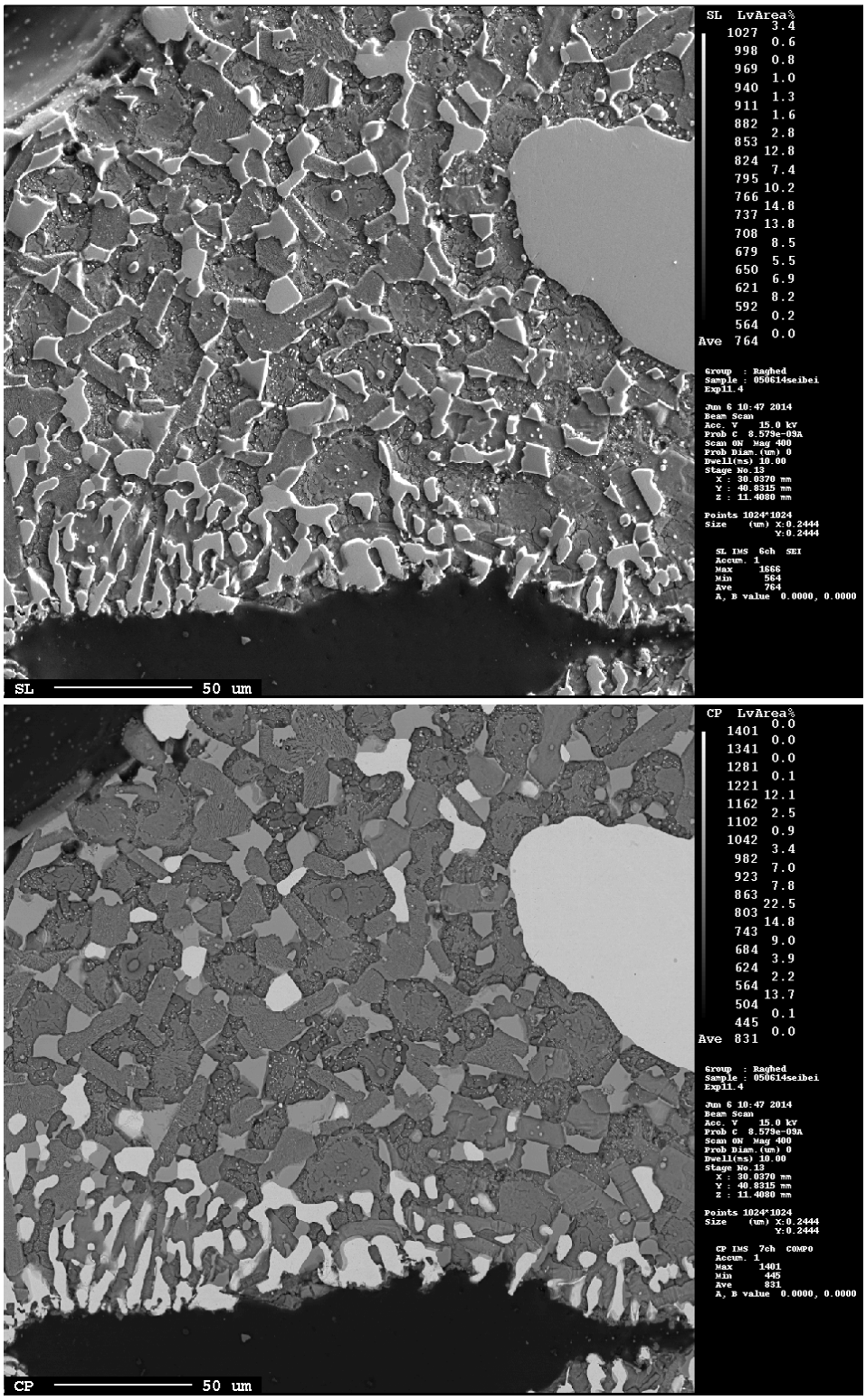

Figure E.9: Fourth EPMA image of experiment 11

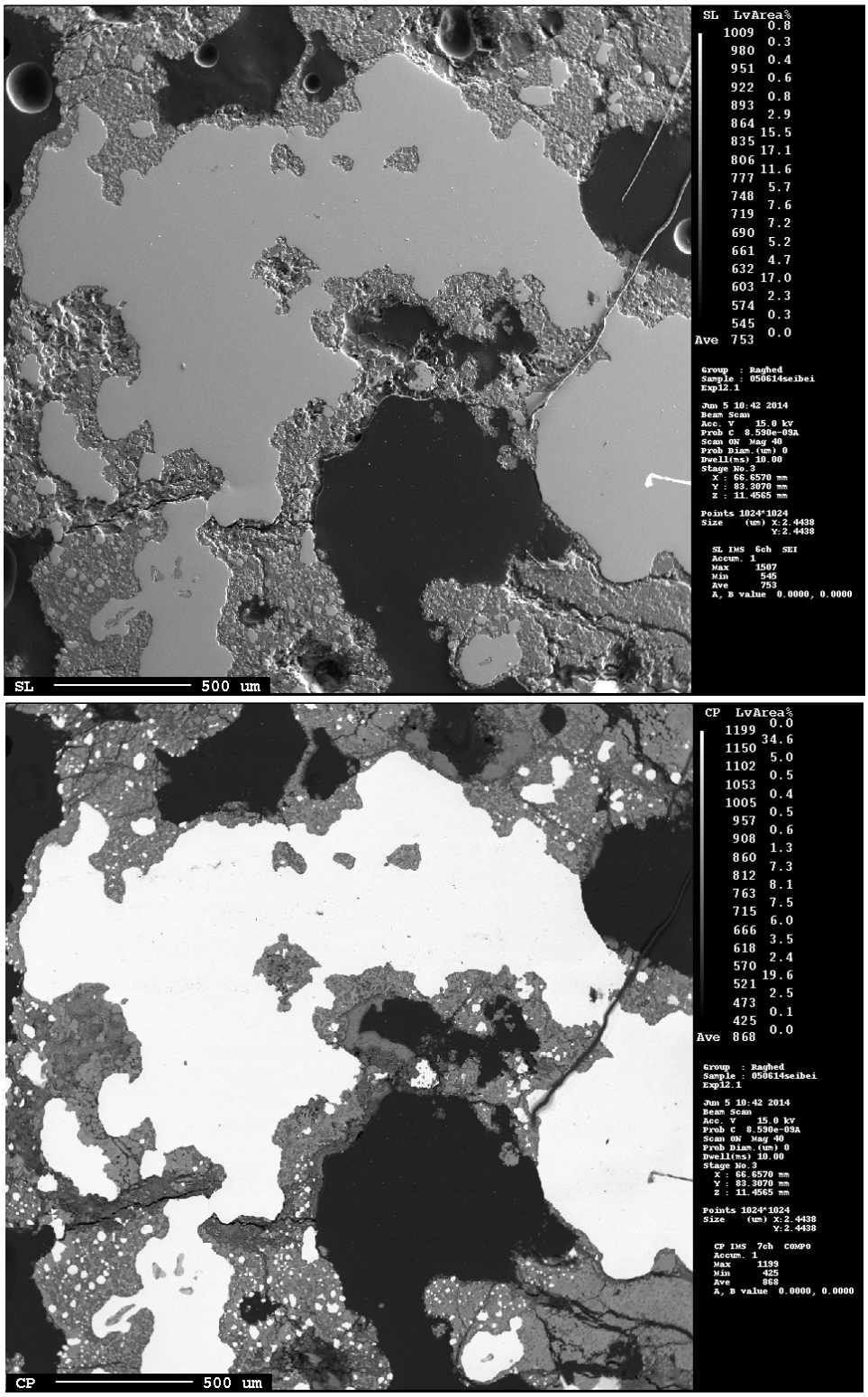

Figure E.10: First EPMA image of experiment 12

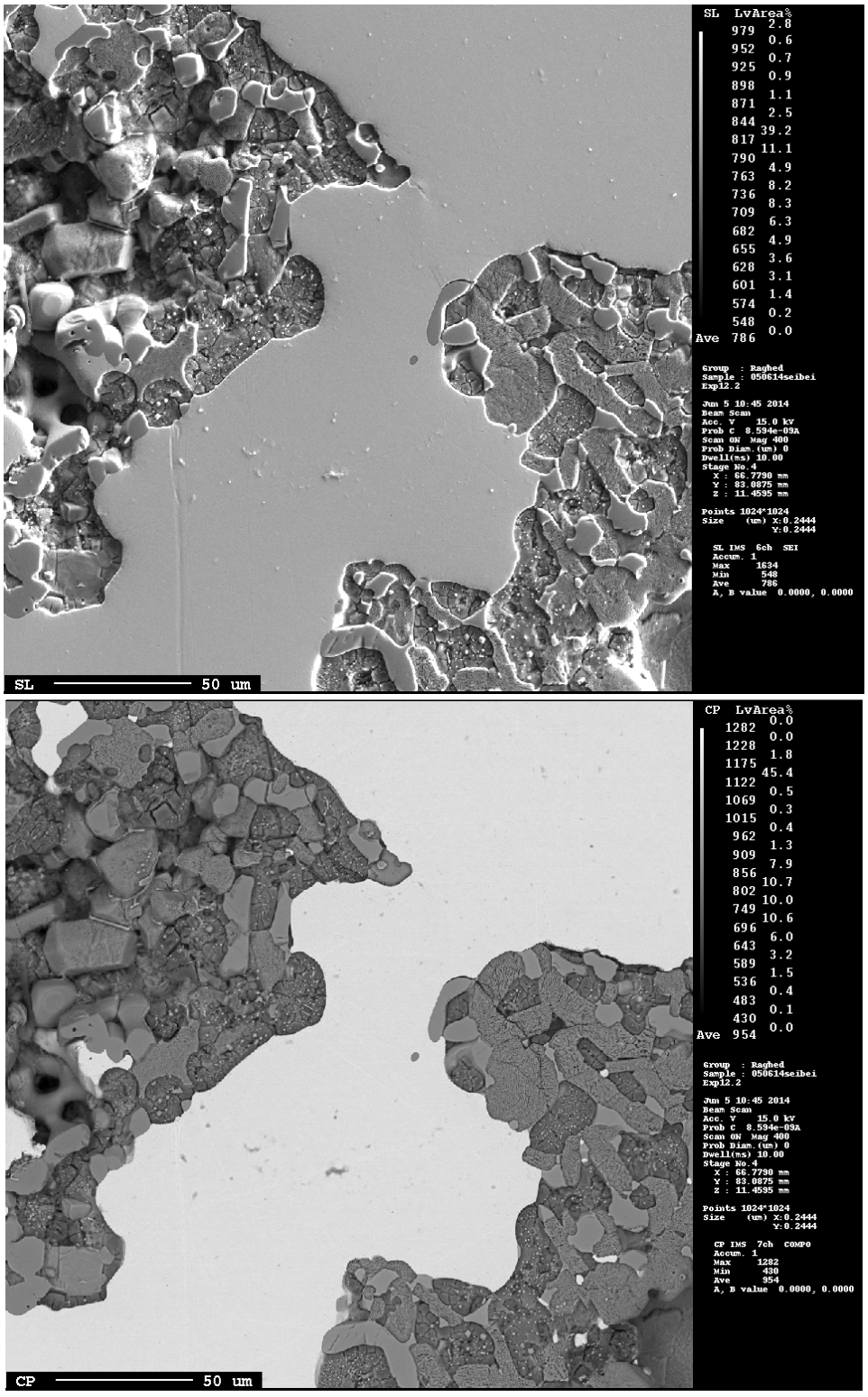

Figure E.11: Second EPMA image of experiment 12

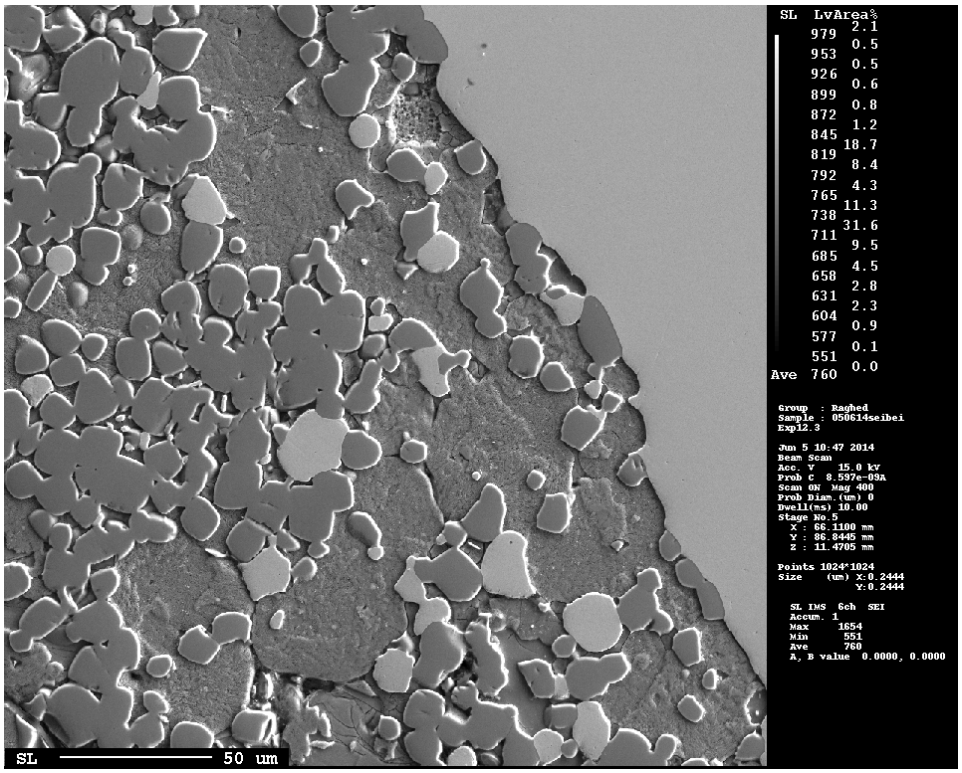

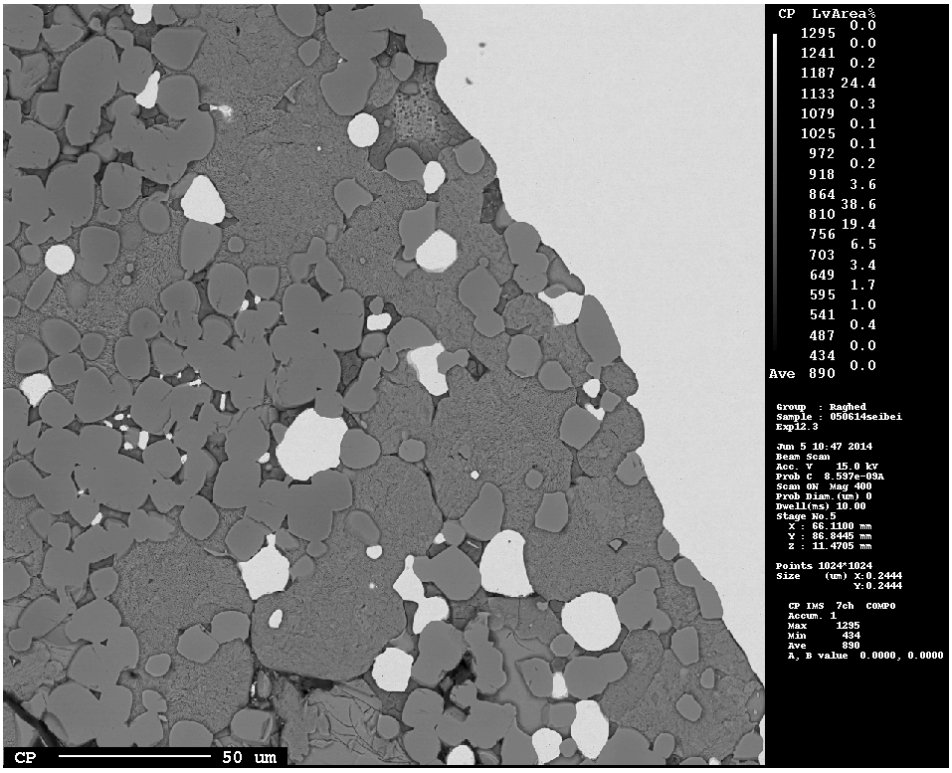

Figure E.12: Third EPMA image of experiment 12

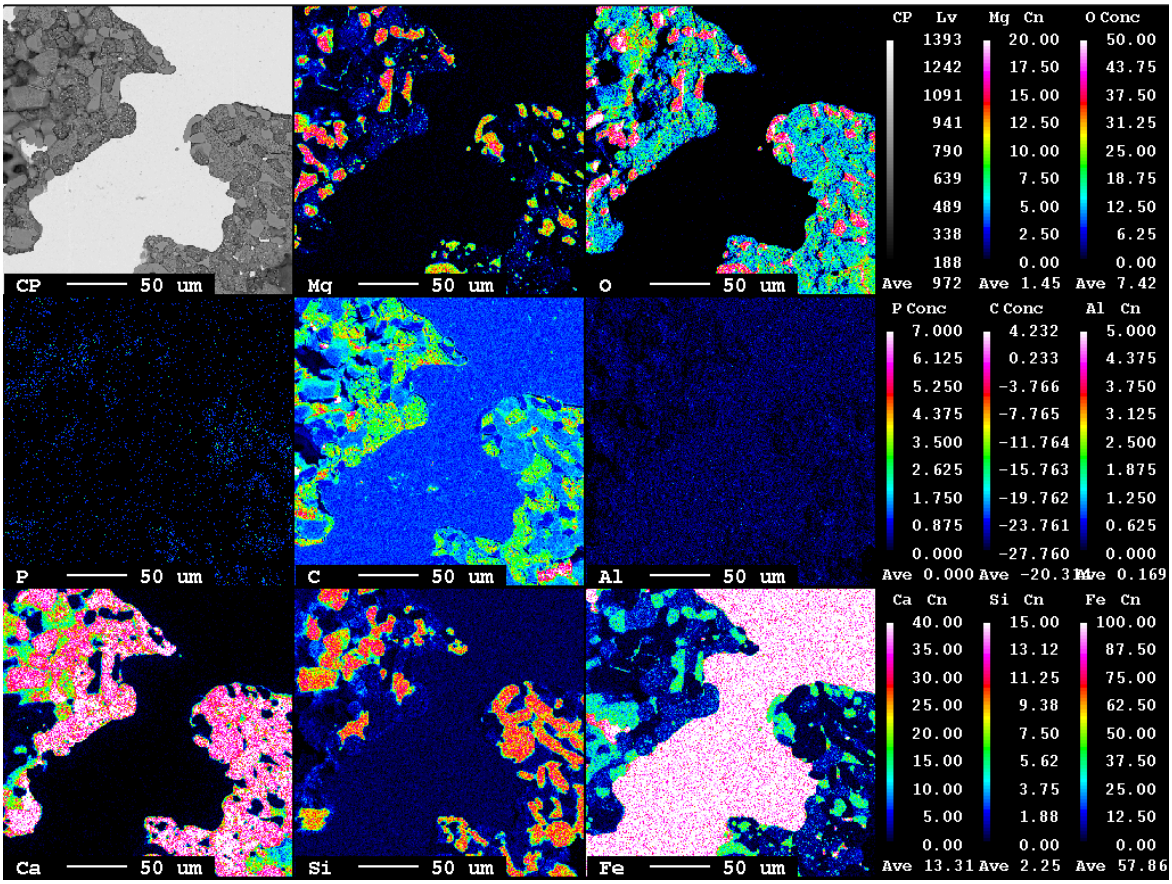

Figure E.13: Mapping of an area from experiment 12

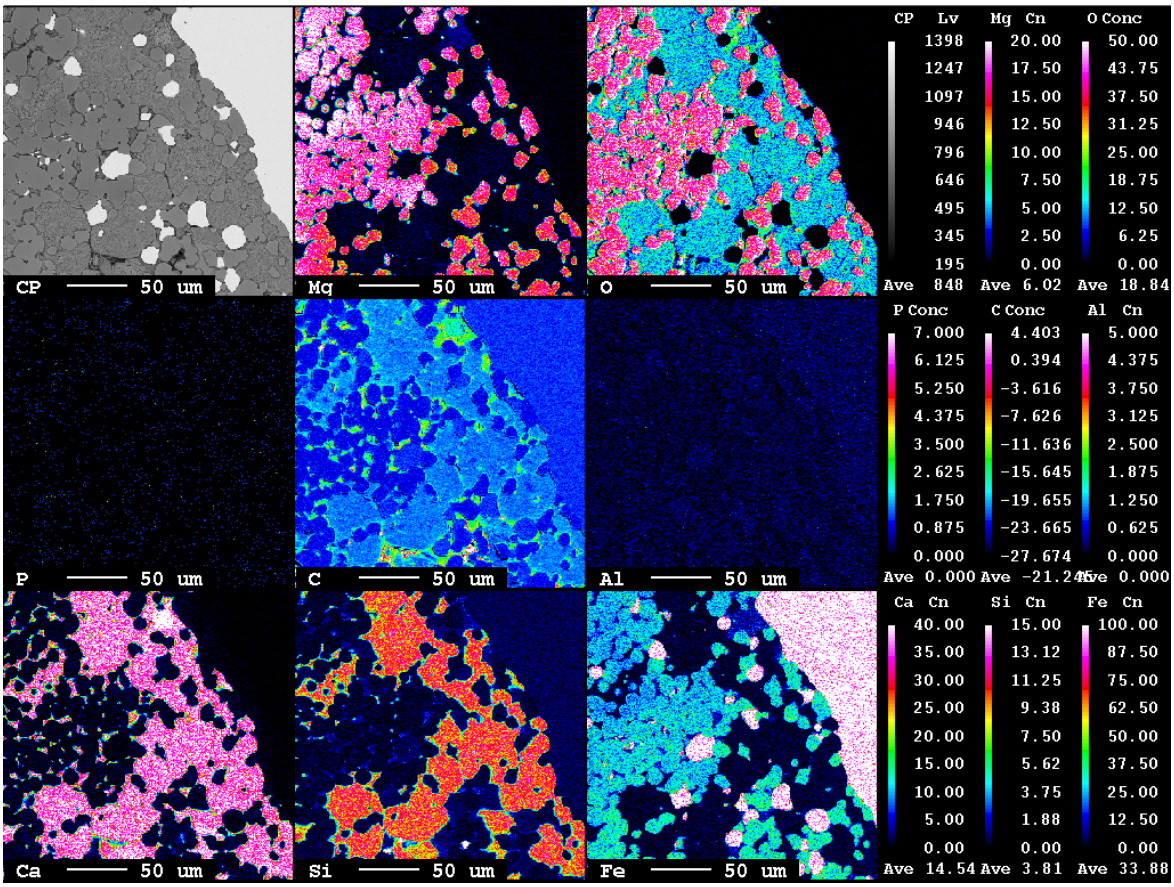

Figure E.14: Mapping of a second area from experiment 12